The Lithospheric Structure of Antarctica from Geophysical–Petrological Modelling

Dissertation zur Erlangung des akademischen Grades
eines Doktors der Naturwissenschaften (Dr. rer. nat.)
der Mathematisch-Naturwissenschaftlichen Fakultät
der Christian-Albrechts-Universität zu Kiel

vorgelegt von

Folker Pappa

Institut für Geowissenschaften

Kiel, November 2019

Erster Gutachter:

Prof. Dr. Jörg Ebbing

Christian-Albrechts-Universität zu Kiel
Institut für Geowissenschaften
Otto-Hahn-Platz 1
24118 Kiel

Zweiter Gutachter:

Dr. Ir. Wouter van der Wal

Delft University of Technology
Aerospace Engineering
Kluyverweg 1
2629 HS Delft, Niederlande

Tag der mündlichen Prüfung: 08. Januar 2020

Zum Druck genehmigt: _____

Der Dekan

Erklärung

Diese Arbeit ist – abgesehen von den angegebenen Hilfsmitteln und der Beratung durch meinen Betreuer – nach Form und Inhalt meine eigene. Die Arbeit hat weder ganz noch zum Teil schon einer anderen Stelle im Rahmen eines Prüfungsverfahren vorgelegen. Die Arbeit wurde – mit Ausnahme der einbezogenen und gekennzeichneten Publikationen – weder veröffentlicht noch zur Veröffentlichung eingereicht. Die Arbeit ist unter Einhaltung der Regeln guter wissenschaftlicher Praxis der Deutschen Forschungsgemeinschaft entstanden. Ein akademischer Grad wurde nicht entzogen.

Kiel, November 2019 Folker Pappa

Zusammenfassung

In dieser Dissertation werden Satellitenschweredaten zusammen mit seismischen Befunden dazu verwendet, Inversionsrechnungen zur antarktischen Mohotiefe durchzuführen. Die Ergebnisse deuten auf einen signifikant geringeren Dichteunterschied zwischen Kruste und Mantel unterhalb der Ostantarktis gegenüber der Westantarktis hin. Darauf aufbauend werden zwei konträre Szenarien zur Mohotiefe mithilfe integrierter, geophysikalisch-petrologischer 2D-Modellierverfahren entlang eines relativ gut untersuchten Profils analysiert. Trotz der gekoppelten Einbeziehung mehrerer geophysikalischer Größen konnte auf diesem Wege jedoch kein eindeutiges Ergebnis erzielt werden. Stattdessen sind umfangreiche, dreidimensionale Modellierungen erforderlich.

Unter Verwendung von Schweregradientendaten aus Satellitenmessungen wird in der vorliegenden Arbeit ein 3D-Modell der antarktischen Lithosphäre und des sublithosphärischen Mantels erstellt, das in sich thermodynamisch konsistent ist. Eine neue Tiefenkarte der Moho-Diskontinuität wird vorgelegt, die mit unabhängig gewonnenen seismischen Ergebnissen im Einklang steht und zahlreiche Details in bislang kaum erforschten Gebieten der Ostantarktis aufweist. Die modellierte Tiefe der Lithosphärenbasis bestätigt frühere Studien hinsichtlich des starken Kontrasts zwischen Westantarktika (<100 km) und Ostantarktika (bis zu 260 km).

Aus dem modellierten Temperaturfeld werden Mantelviskositäten abgeleitet, die ihrerseits Eingang in ein GIA-Modell finden. Der Vergleich mit GPS-Messungen gegenwärtiger Landhebungsraten lässt auf relativ niedrige Viskositätswerte schließen, die der Rheologie trockenen Mantelmaterials entsprechen. Abschließend wird der Krustenbereich des Dichtemodells mit aerogravimetrischen Messdaten abgeglichen. Aus dem kurzwelligen Signalanteil werden Dichtevariationen innerhalb der Oberkruste invertiert, um das Lithosphärenmodell auf regionaler Skala nachbessern zu können. Anhand dieser Beispiele sollen die Möglichkeiten des vorgelegten Modells als Basis für weitere Studien zum antarktischen Kontinent aufgezeigt werden.

Abstract

In this thesis, satellite gravity data are combined with seismic findings to invert for the Moho depth of Antarctica. The results suggest a significantly lower density contrast between crust and mantle underneath East Antarctica compared to West Antarctica. Accounting for that, combined geophysical-petrological modelling of the lithosphere in 2-D is conducted along a well studied profile to test different Moho depth scenarios. However, even though multiple geophysical observables are considered in an integrated manner, neither of the competing scenarios can be validated or refuted with this approach. This demonstrates the need for comprehensive modelling in 3-D.

By utilizing satellite gravity gradient data in a thermodynamically self-consistent framework, this dissertation establishes a 3-D model of the Antarctic lithosphere and sublithospheric upper mantle. A new Moho depth map of the continent is derived that is in good agreement with independent seismic estimates. It also exhibits detailed variations for so far scarcely explored areas. Total lithospheric thickness values of the presented model confirm the marked contrast between West Antarctica (<100 km) and East Antarctica (up to 260 km).

The inferred deep thermal field is used to estimate 3-D viscosities of the mantle for GIA modelling. Coupled with present-day uplift rates from GPS, the relatively low viscosity values suggest a bulk dry upper mantle rheology. Finally, the crustal part of the 3-D density model is tested against recent airborne gravimetric data. The short-wavelength residual signal is inverted for near-surface density variations within the crust with the aim to refine the continental lithospheric model on a regional scale. These two applications demonstrate the potential of the presented model for further regional and continental-scale studies of Antarctica.

Contents

Chapter 1

Introduction

1.1. Motivation and State of Knowledge

Antarctica is often referred to as the "frozen continent". This is not only true for the vast ice sheets, which cover more than 99% of its land surface and are up to 4.5 km thick (Burton-Johnson et al., 2016; Fretwell et al., 2013). The term also applies to the geodynamic situation: Antarctica's location on Earth has been extraordinarily stable since ~75 Ma (e.g. Torsvik et al., 2007).

In the context of global climate change and melting ice sheets, south polar sciences have attracted increasing attention by the public, for the Antarctic is a key region regarding potential sea level rise. Though rarely mentioned in this connection, knowledge about the sub-ice structure of the continent is of fundamental importance for reliably estimating the potential loss of ice mass (Frederikse et al., 2019; King et al., 2012). The general principles of the solid Earth response to ice mass changes, i.e. glacial isostatic adjustment (GIA), are well understood and numerously studied in Antarctica (e.g. van der Wal et al., 2015; Whitehouse et al., 2012). In order to quantify past and future extents of deglaciation, however, robust Earth models are required (e.g. Nield et al., 2018). Despite recent efforts (e.g. Haeger et al., 2019; An et al., 2015a), the current knowledge is particularly poor regarding geophysical properties like density and temperature of the crust and upper mantle in Antarctica. Both of these parameters have a determining influence on the upper mantle viscosity, which itself is of key interest for GIA modelling. While earlier studies have commonly assumed a laterally homogeneous viscosity structure of the Earth, lately the necessity to account for 3-D variations has become more and more recognized (e.g. Nield et al., 2018; van der Wal et al., 2015; A et al., 2013; Kaufmann et al., 2005). This is especially vital in the case

of Antarctica with its spatially variable lithospheric thickness (e.g. An et al., 2015a). Even though seismological models are typically used to infer 3-D mantle temperatures and thereby viscosities (e.g. Nield et al., 2018; O'Donnell et al., 2017), the uncertainties arising from the conversion of seismic velocities are high, and the results are not always consistent with findings derived from other geophysical methods. Comprehensive approaches to jointly model multiple properties of the lithosphere and sublithospheric upper mantle have the potential to reduce the ambiguities associated with the individual geophysical observables (Fullea et al., 2012). Applying such a technique to Antarctica can help to better constrain the temperature and density distribution in the subsurface and thus lead to more robust quantifications of GIA processes.

Furthermore, many questions concerning the geological architecture remain open for large parts of Antarctica. For instance, it is still unclear where major tectonic boundaries extend in the interior of the East Antarctic Craton (e.g. Stål et al., 2019; Harley et al., 2013; Boger, 2011; Fitzsimons, 2000), such as the Pan-African suture (~550–500 Ma), which is related to the assembly of the supercontinent Gondwana (Torsvik and Cocks, 2016; Cawood and Buchan, 2007). Expanding and consolidating the knowledge about the inner structure of Antarctica is therefore crucial for reconstructing Earth's geodynamic history (e.g. Harley et al., 2013). Since the whole continent is covered by a thick ice sheet, bedrock is not directly accessible in most places. Thus, geophysical methods are indispensable in exploring the sub-ice structure. A number of seismological studies have been published in recent years that investigate specific regions such as West Antarctica and the Transantarctic Mountains (e.g. O'Donnell et al., 2019, 2017; White-Gaynor et al., 2019; Shen et al., 2018, 2017; Graw and Hansen, 2017; Hansen et al., 2016; Lloyd et al., 2015) or Antarctica as a whole (e.g. Heeszel et al., 2016; Ramirez et al., 2016; An et al., 2015b; Hansen et al., 2014). They provided valuable new insights into the tectonic configuration of the continent. However, the harsh environment makes seismic experiments challenging. Large gaps exist in the station coverage, and ice reverberations may complicate the interpretation of measured data (Hansen et al., 2009).

Geophysical potential field methods, on the other hand, are inherently non-unique and need additional constraints, though they can provide important information complementary to seismic findings. Considerable progress has been made during recent years in both airborne and satellite-based gravity field observations over Antarctica (e.g. Zingerle et al., 2019; Forsberg et al., 2018; Scheinert et al., 2016; Aitken et al.,

2014; Riedel et al., 2012; Ferraccioli et al., 2011). In particular, satellite data are well suited to overcome the remoteness of the Antarctic continent, as they have an almost global uniform coverage (Ebbing et al., 2018). However, despite several efforts to combine existing and conflicting findings from seismology and gravimetry (e.g. Chisenga et al., 2019; Haeger et al., 2019; Baranov et al., 2018; O'Donnell and Nyblade, 2014), a coherent image of the lithospheric characteristics of Antarctica is still missing.

1.2. Objectives and Structure of this Thesis

This thesis integrates multiple observables from different geophysical methods into a consistent lithospheric model of the Antarctic continent.

- In chapter 2, a study is presented, which is published under the title *Moho Depths of Antarctica: Comparison of Seismic, Gravity, and Isostatic Results* (Pappa et al., 2019a) in *Geochemistry, Geophysics, Geosystems*. Satellite gravity data and seismic estimates are used to invert for the Moho depth of Antarctica. The evaluation and comparison of the results with other existing models leads to the conclusion that the common simplification of assuming a homogeneous density contrast between crust and mantle is not applicable to Antarctica. Even more comprehensive lithospheric modelling in 2-D is inconclusive in case of the exemplary study area of the Wilkes Land region, which demonstrates the need for 3-D modelling with additional constraining data to shed more light on the lithospheric structure of the Antarctic continent. My contributions to this paper are the modelling and computation, the initial manuscript, and all figures.

- The 3-D lithospheric model of Antarctica is established and presented in the second paper *Modeling Satellite Gravity Gradient Data to Derive Density, Temperature, and Viscosity Structure of the Antarctic Lithosphere* (Pappa et al., 2019b), published in *Journal of Geophysical Research: Solid Earth*. The paper is provided in chapter 3. I developed the lithospheric model, compiled the initial manuscript and created all figures.

- Chapter 4 provides an overview of the gravimetric data for studying the upper mantle of Antarctica and the state of knowledge that is gained therefrom.

In particular, discrepancies between existing depth models of the crust-mantle boundary are discussed. Moreover, this part of the thesis describes the potential of the shape index, which is a derivate of the gravity gradient tensor, for interpretations of lithospheric structures. This chapter is a draft for a part of a book chapter on geophysical data for *The Antarctic Mantle: a petrological, geophysical, geodynamic, and geodetic view* (Eds. Adam P. Martin and Wouter van der Wal).

- In chapter 6, the previously introduced 3-D lithospheric density model is checked against a high-resolution gravity model based on satellite and airborne measurements. The residual gravity signal at a low altitude is, for the most part, of short wavelengths and taken to invert for near-surface density variations in the upper crust. The results are compared with other geophysical data such as magnetic anomalies. Finally, the inferred small-scale density variations can be used to refine the lithospheric model in its crustal part. This chapter is planned for publication as part of a study exploring and comparing the role of airborne and terrestrial data vs. satellite data for crustal and upper mantle modelling.

- This thesis concludes with a brief summary and an outlook on future work.

Chapter 2

Moho Depths of Antarctica: Comparison of Seismic, Gravity, and Isostatic Results

F. Pappa[1], J. Ebbing[1], F. Ferraccioli[2]

[1] Department of Geosciences, Kiel University, Kiel, Germany
[2] British Antarctic Survey, Cambridge, UK

Published in: *Geochemistry, Geophysics, Geosystems*, 20, 1629–1645.
https://doi.org/10.1029/2018GC008111

2.1. Introduction

The lithosphere of the Antarctic continent is still poorly known, despite several major airborne geophysical campaigns including the acquisition of extensive gravity and magnetic measurements and recent continental-scale data compilations (e.g. Golynsky et al., 2018, 2006; Aitken et al., 2016, 2014; Scheinert et al., 2016; Ferraccioli et al., 2011, 2009a; Chiappini et al., 2002) and a variety of recent seismological studies (e.g. Shen et al., 2018, 2017; Ramirez et al., 2017, 2016; An et al., 2015b; Chaput et al., 2014; Hansen et al., 2014).

In the last two decades, several Antarctic seismological campaigns have been carried out, in particular within the Fourth International Polar Year (2007–2008). These led to a more robust and comprehensive insight of the crustal thickness and upper mantle structure of Antarctica, and their results have been incorporated in continental-scale

Moho depth models. Still, seismological investigations suffer from limited station coverage over large areas. This can lead to large discrepancies in estimates of Moho depth or upper mantle velocities. For example, differences in Moho depth estimation can add up to 10 km, even for the same station (see the supporting information of An et al., 2015a). These differences affect other fields of Antarctic research. Glacial isostatic adjustment studies, for instance, require reliable and robust lithospheric models. Ice sheet dynamics is strongly related to basal melting and geothermal heat flow, which in turn is influenced by crustal thickness variations. It is therefore necessary to attempt to reconcile the different existing data sets by the use of additional geophysical information.

Satellite data are particularly well suited to overcome the remoteness of the Antarctic continent, as they have an almost global uniform coverage (Ebbing et al., 2018). In contrast to surface and airborne surveys, satellite measurements also contain consistent long-wavelength (>150 km) information, which is mainly influenced by deep subsurface structures (Sebera et al., 2018). They are furthermore less affected by near-surface density changes, which are associated with intracrustal geological features. However, potential field methods like gravity suffer inherently from non-uniqueness and thus need additional constraints. In relation to crustal thickness, this can be a certain density contrast at the Moho, in combination with a reference depth, and/or certain depth constraints, for example, from seismology.

Using gravity data, Block et al. (2009) inverted Antarctica's crustal thickness from gravity data by application of the Parker-Oldenburg technique and found Moho depths of ~45 km beneath the southern Transantarctic Mountains (TAM) and the Gamburtsev Subglacial Mountains (GSM). However, seismological studies estimate crustal thickness values of 35–40 km beneath the TAM (Ramirez et al., 2017) and up to 58 km beneath the GSM (Ramirez et al., 2016; Heeszel et al., 2013; Hansen et al., 2010). Considering different values for the density contrast at the Moho, O'Donnell and Nyblade (2014) inverted the crustal thickness of East Antarctica (EANT) and West Antarctica (WANT) with Parker-Oldenburg algorithms separately and used seismic inferred depth values to constrain their results. Their depth values are closer to those from seismological studies but still differ significantly in some regions, for example, the southern TAM. Furthermore, O'Donnell and Nyblade (2014) examined the correlation between the topography and the inverted crustal thickness and recognized missing buoyancy support from the crust for the GSM and Dronning Maud Land in terms of isostatic balance. They suggest alternative mechanisms, such as anomalous

middle-to-lower mantle structures, as plausible explanations that could affect the isostatic balance in these regions.

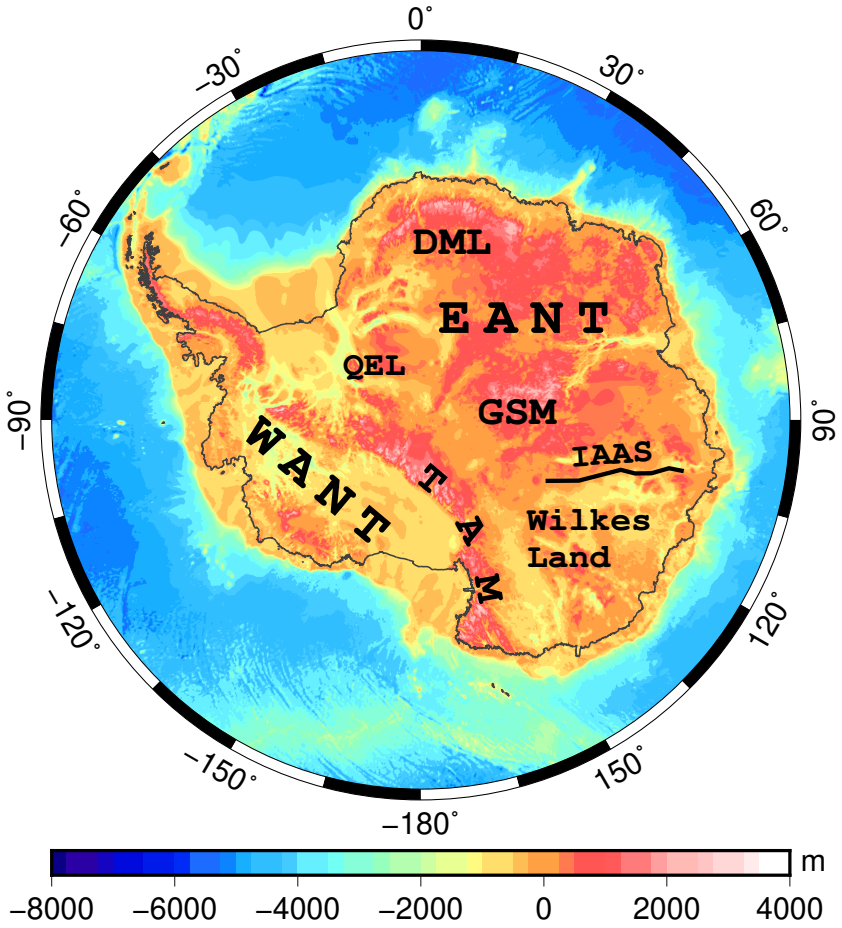

Figure 2.1.: Bedrock topography of Antarctica from Bedmap2 model (Fretwell et al., 2013). WANT=West Antarctica; EANT=East Antarctica; DML=Dronning Maud Land; GSM=Gamburtsev Subglacial Mountains; IAAS=Indo-Australo-Antarctic Suture; QEL=Queen Elizabeth Land; TAM=Transantarctic Mountains.

In our study, we invert the depth of the Antarctic Moho with satellite gravity data from the GOCO05s model by using the tesseroid method from (Uieda and Barbosa, 2017), constrained by seismic depth estimates. Second, we compare our new inversion results with existing seismological Moho depth models and an Airy-isostatic Moho model. High discrepancies are found in some regions, and we discuss these in terms of the potential for different modes of isostatic compensation and upper mantle composition variations beneath different parts of EANT. Specifically, we focus on evaluating two markedly different seismologically derived Moho depth estimations in the hinterland of the TAM in the Wilkes Subglacial Basin region, along the Trans-

Antarctic Mountain Seismic Experiment (TAMSEIS)–GAmburtsev Mountain SEISmic experiment (GAMSEIS) profile (Hansen et al., 2009; Lawrence et al., 2006a,b) by using 2-D models of the lithosphere and the sublithospheric upper mantle. These models incorporate isostasy, the thermal field, seismic velocities, mantle petrology, geoid, and heat flow estimations. Using this approach, we demonstrate that both thinner and thicker crusts beneath the Wilkes Subglacial Basin can lead to an acceptable fit of the observed satellite gravity data. However, we also show that the thinner-crust scenario is preferred if the region is underlain by a moderately depleted lithospheric mantle of inferred Proterozoic age, while the thicker crust is more likely if refertilization processes likely linked to Ross-age (ca. 500 Ma) subduction (e.g. Ferraccioli et al., 2002) along the margin of the composite East Antarctic Craton are invoked. Overall, we conclude that satellite gravity data can complement seismological observations thereby providing an important tool for the development of new 2-D and 3-D models of the Antarctic crust and deeper lithosphere.

2.2. Data

2.2.1. Bedrock Topography and Gravity Data

Bedmap2 is a compilation of the ice thickness and the bedrock topography (Figure 2.1) of Antarctica up to latitude 60° S and is mainly based on airborne radar surveys (Fretwell et al., 2013). Even though some areas are not well covered and exhibit large uncertainties of up to >1000 m, it is the best ice thickness model currently available for Antarctica. The data set is provided as an interpolated grid with 1-km spacing.

We use the combined gravity model GOCO05s (Mayer-Gürr, 2015) to obtain the geoid undulation and the vertical gravity over Antarctica (Figure 2.2). In order to suppress contributions in the signal from below the lithosphere, the geoid is calculated in spherical harmonics from degree and order 12 up to 280 (maximum of the GOCO05s model). The truncation of $N < 12$ is commonly done to eliminate long-wavelength components from the signal, which are associated with sublithospheric sources (Fullea et al., 2009, and references therein). The geoid is in particular used in the 2-D modeling (section 2.4).

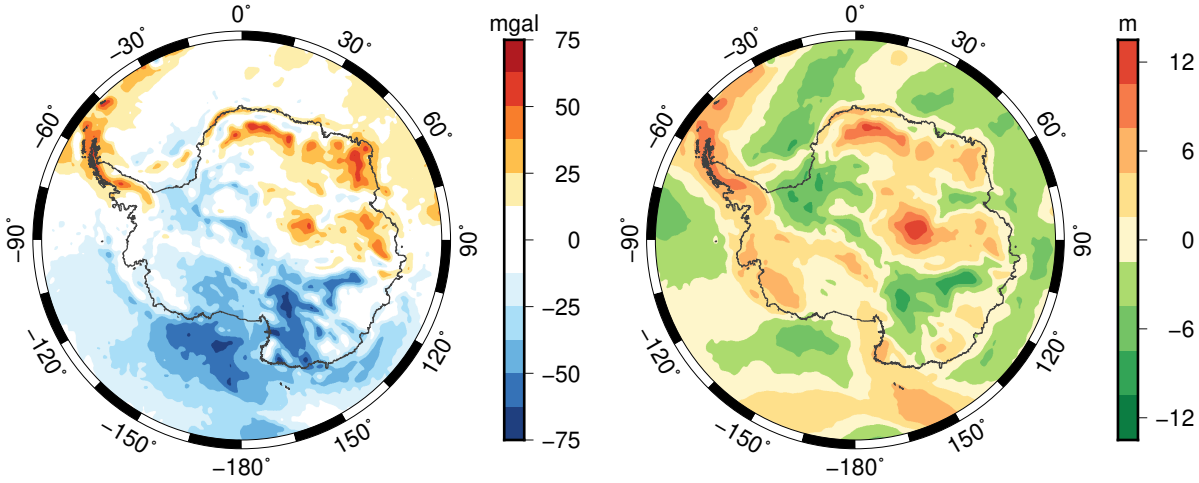

Figure 2.2.: Gravity disturbance at 50-km altitude (left) and geoid (right) from GOCO05s model. The geoid is computed from spherical harmonics expansion from degree and order N = 12 to 280.

Second, we take the gravity disturbance signal (Figure 2.2) at a height of 50 km from the GOCO05s model. The gravity disturbance is a form of free air anomaly reduced to the surface of the normal Earth ellipsoid (Li and Götze, 2001). The representation of the field at 50 km is chosen, as it offers a higher level of detail in the signal than at satellite altitude (~250–500 km) and ensures that the noise amplification is still acceptable for the purpose of crustal thickness and lithospheric modeling (e.g. Sebera et al., 2014).

The total gravity signal originates from several sources, and the free-air anomaly is largely affected by topography and its isostatic compensation. However, we are interested in the Moho geometry and therefore compute the Bouguer gravity anomaly, where the signal arising from the bedrock topography and ice thickness variations is corrected for. In the Bouguer anomaly, the density contrast at the crust-mantle boundary in most cases has a dominating influence on the gravity signal. Even though the remaining signal possibly still contains effects from density variations within the crust or the mantle, or an imperfect topographic reduction model, the Bouguer anomaly can be regarded as suitable for an inversion of the Moho geometry. To compute the Bouguer anomaly above Antarctica, we use density values for water ($\rho_{\text{water}} = 1028$ kg/m^3), ice ($\rho_{\text{ice}} = 917$ kg/m^3), and bedrock elevation ($\rho_{\text{topo}} = 2670$ kg/m^3) together with the ice thickness and topography information from Bedmap2. In our gravity data processing, we also account for far-field and edge effects from masses outside the model area. Szwillus et al. (2016) demonstrated that both topographic masses and iso-

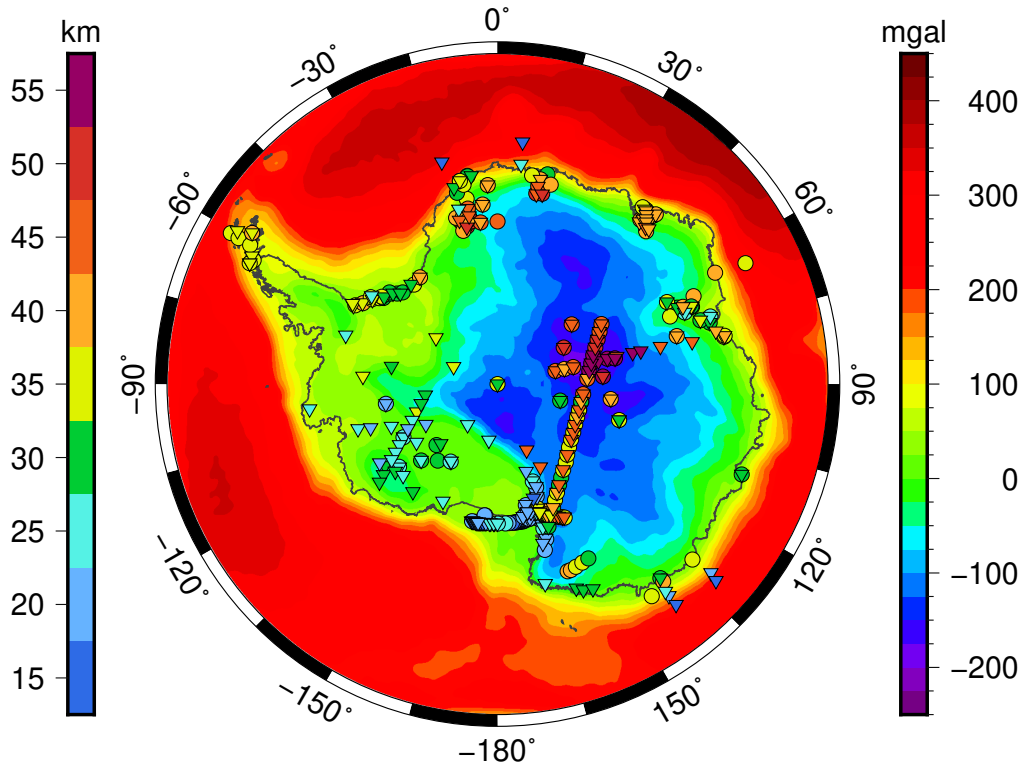

Figure 2.3.: Bouguer gravity anomaly above Antarctica used as input for the Moho depth inversion. Gravity data from GOCO05s at 50 km height corrected for effects from ice, water, and bedrock topography. In addition, the effect from a global Airy-isostatic Moho outside the model area is subtracted. The point sets of seismologically constrained Moho depth values are represented by colored triangles (AN1 model) and circles (ANT model).

static effects need to be considered in a global background model for continental-scale areas of interest. We use the ETOPO1 (Amante and Eakins, 2009) data set to compute a global topographic correction model and a simple Airy-isostatic Moho model (z_{ref} = 30 km, $\Delta\rho$ = 450 kg/m^3). For both models, Antarctica is cut out because we have the better topographic model from Bedmap2, and the Moho is to be inverted for the continent. The result is a Bouguer gravity anomaly above Antarctica (Figure 2.3), which most closely corresponds to the signal from the crust-mantle boundary.

2.2.2. Seismological Models

We make use of previous seismological studies in two ways. First, we use points of seismic Moho depth estimates to constrain our gravity inversion and thereby attempt to overcome the inherent ambiguity of potential field methods. Second, we evaluate

existing continent-wide Moho depth models based on seismology in terms of their gravity signal and compare them with our inversion results. Thus, a set of points with Moho depth estimations as well as a gridded Moho depth model is needed for our purpose. In this study we revert to the models (a) "AN1-Moho" from An et al. (2015b), which is a 3-D *S* wave velocity model resulting from Rayleigh wave dispersion analyses, and (b) "ANT-Moho" from Baranov and Morelli (2013), which is a compilation of regional seismological surveys, interpolated with the standard kriging method (Figure 2.4). More recent studies exist (e.g. Shen et al., 2018, 2017; Ramirez et al., 2017, 2016) but do not cover whole Antarctica or do not provide both single points and areal Moho depth estimation.

Although the AN1-Moho and the ANT-Moho reflect the strong contrast in crustal thickness between WANT (~25 km) and EANT (~40 km), they disagree in large parts and differ up to 20 km in depth (Figure 2.4). In particular, the crustal thickness of Wilkes Land (compare Figure 2.1) is estimated to be ~40 km in the AN1 model, while the ANT model shows values of ~30 km. Not only do the two seismological models exhibit wide disparities in many regions of Antarctica but they also contradict the observed gravity signal when a certain density contrast at the Moho is assumed. Figure 2.4 shows the mismatch of both models against the Bouguer gravity anomaly after forward computation of their gravity signal. This disagreement is independent from the applied Moho reference depth and density contrast. Merely, the amplitude of the misfit varies. Considering the calculated Bouguer anomaly to be correct, this implies that either the density contrast at the Moho varies strongly across Antarctica or the seismological models do not represent the actual Moho depth, or a combination of these factors.

Both models are constrained by a set of seismic station points from other studies (see An et al., 2015b; Baranov and Morelli, 2013, and references therein), where the Moho depth is regarded as well constrained (Figure 2.3). Yet, even though many stations are included in both the ANT and the AN1 model, they indicate different Moho depth values, depending on the applied seismological method. This certainly had an influence on the discrepancy between the final models. We take these point sets as a benchmark for the Moho depth models in the gravity inversion. The points from the AN1 and the ANT model will first be used separately, and additionally in a combined set to evaluate the gravity-inverted Moho depth models.

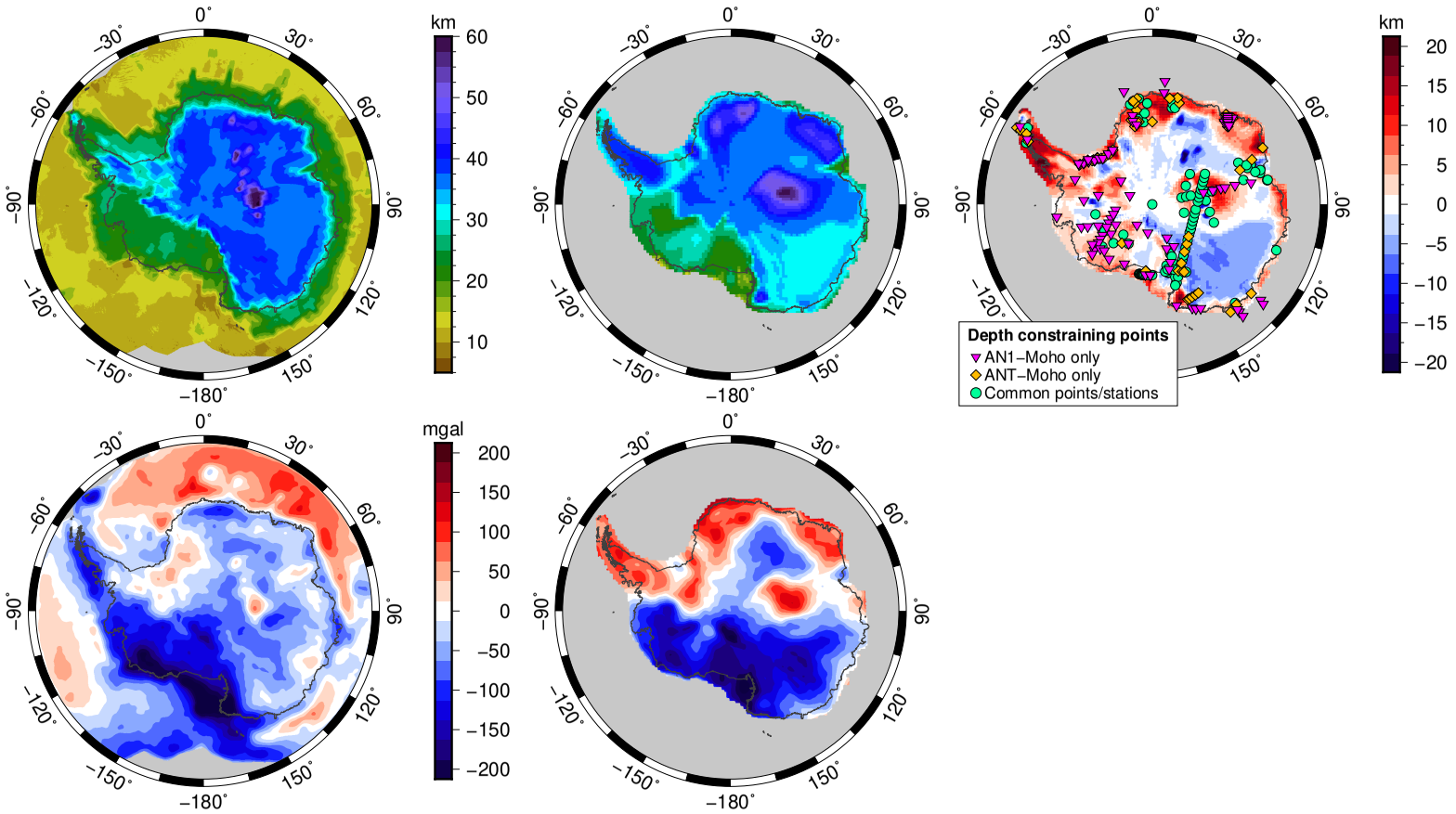

Figure 2.4.: Top: Depth maps of seismic Moho depth models. Left: "AN1-Moho" is derived from an *S* wave velocity model based on Rayleigh wave dispersion analyses (An et al., 2015b); center: "ANT-Moho" is a compilation of regional surveys (Baranov and Morelli, 2013). The strongest differences (right figure) between both models occur in the Wilkes Land, Dronning Maud Land, the periphery of the Gamburtsev Subglacial Mountains, and the Antarctic Peninsula. Bottom: Misfit of forward-calculated gravity effects from seismological Moho depth models (left: AN1; right: ANT) compared to satellite-inferred gravity data at 50 km height. Both models show large disagreement with the gravity data and between each other.

2.3. Moho Depth Inversion from Gravity

2.3.1. Methodology

We follow the methodology of Uieda and Barbosa (2017), who applied a nonlinear inversion algorithm on gravity and seismic data for South America with the Python code package Fatiando. A tesseroid model is created to reproduce the preprocessed gravity signal, parametrized by (1) a regularization parameter, which controls the smoothness of the model; (2) the reference depth (normal Earth Moho depth: z_{ref}); and (3) the density contrast $\Delta\rho$ at the Moho. The regularization parameter is estimated by the inversion of multiple test sets, derived from the original data set. The parameter value that results in the least mean square error (MSE) in predicting the original data set is taken to be optimal. However, we did not find a local minimum within our interval of values for the regularization parameter ($10^{-10} \dots 10^{-4}$). We therefore chose the value of 10^{-6} from which on no further improvement in the MSE can be observed (Figure 2.5).

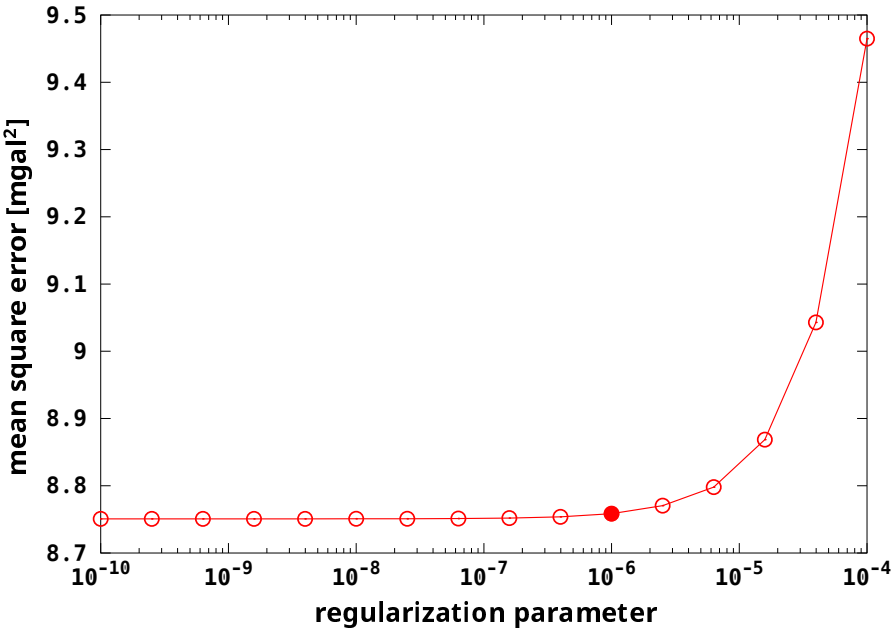

Figure 2.5.: Cross-validation curve of the regularization parameter. No local minimum exists. The value of 10^{-6} is chosen since lower values do not lead to a significantly lower mean square error.

The two other parameters z_{ref} and $\Delta\rho$ span a parameter space for given intervals. Since the mean depth of the Moho and its density contrast are poorly known for Antarctica, we set a wide range for both parameters: the reference depth in 2.5 km steps from 25 to 40 km, and the density contrast in 25 kg/m^3 steps from 250 to 550 kg/m^3. For each pair of reference depth and density contrast in this discretized parameter space, the inversion is performed with the previously estimated regularization parameter. Afterwards, the results are evaluated against a set of points with verified Moho depth values from seismic experiments. Finally, the model that gives the smallest MSE in this evaluation is taken as the best fitting one. Further details of the methodology are described in Uieda and Barbosa (2017).

Since the Fatiando Python code demands an equiangularly discretized gravity data set to create a similarly discretized tesseroid model, all data sets used for the inversion are relocated from the South Pole to the equator. The geographical coordinates from the Antarctic environment are projected into Cartesian coordinates with a Lambert Equal Area projection and subsequently reprojected into geographical coordinates at the equatorial region from 30° W to 30° E and 30° S to 30° N. This is done with a spherical Earth in order to avoid distortions due to the use of the WGS84 ellipsoid.

We perform three separate inversions for individual sets of seismological Moho depth points: at first for the point set that was used by An et al. (2015b) to constrain their Moho depth model ("AN1"), second for the point set used for the kriging-interpolated compilation from Baranov and Morelli (2013) ("ANT"), and third a combined set of both ("comb"). Additionally, we aim to address the different tectonic settings of WANT and EANT in separate inversions, using only seismic points inside the respective area.

2.3.2. Inversion Results

Depending on the point set of seismological Moho depth values, different pairs of reference depth and density contrast yield the best fit (Figure 2.6). While the least error for the "AN1" set is found at z_{ref} = 27.5 km and $\Delta\rho$ = 350 kg/m^3, the "ANT" set is best fitted with z_{ref} = 30 km and $\Delta\rho$ = 450 kg/m^3. The optimum of the combined set is at z_{ref} = 30 km and $\Delta\rho$ = 425 kg/m^3. Consequently, the inverted Moho depths differ. The maximum depth of all models is about 45 km, consistent with the gravity inversion results from Block et al. (2009), and they overall agree in EANT. In WANT,

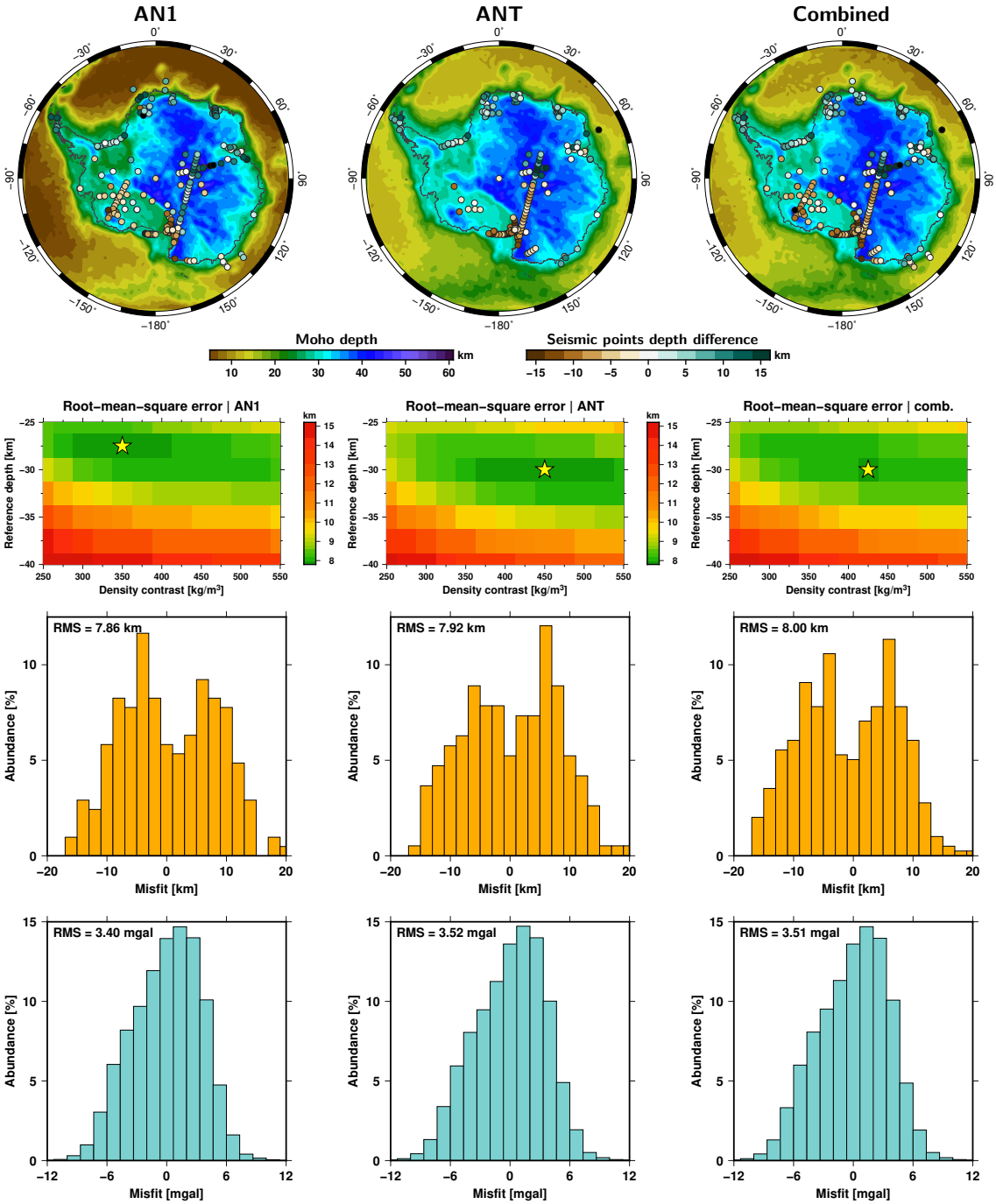

Figure 2.6.: Top: Resulting Moho depth maps from the inversion for different seismic depth point sets (from left to right: AN1, ANT, and combined). The colored circles indicate the differences in depth between the seismic constraint and the inverted depth. Second row: root mean square (RMS) error within the applied parameter space. The best fitting pair of reference depth and density contrast is marked by the star symbol. Underneath: histograms of Moho depth difference and corresponding RMS. Bottom: histograms of gravity residuals.

however, the model inverted with the point set "AN1" shows a 3- to 5-km shallower Moho than the other two, which comes along with the lower density contrast.

As O'Donnell and Nyblade (2014) emphasize, a single inversion for the whole continent with one constant density contrast and Moho reference depth results in a compromise between the distinct blocks of cratonic EANT and rift-dominated WANT. We too see this effect very apparent in the map images and the mismatch histograms in Figure 2.6. The latter show two distinct Gaussian curves, reflecting the western and the eastern part of Antarctica. Thus, we also conducted the inversion procedure with seismic points from the combined set constrained to the respective area of WANT and EANT (Figure 2.7). For WANT we find a well-resolved optimal reference depth of ~25 km. The density contrast, however, is rather diffuse without a clear optimum. We interpret this as an indication of a strong heterogeneity in the region. Compared with this, we also find a distinct reference depth for EANT at z_{ref} = 35 km but also a better resolved optimal density contrast of $\Delta\rho$ = 625 kg/m^3. In this particular case, the reference depth seems reasonable and corresponds to the cratonic nature of EANT. However, the density contrast is most likely overestimated, since the gravity signal needs to be reproduced over the whole study area, including WANT and oceanic areas. Regardless of this, the derived Moho topography beneath EANT reflects the best fit according to the seismic depth points inside the area. In both parts of Antarctica, the misfit concerning the seismic depth points is decreased significantly compared to the inversion for the whole continent. Still, the density contrast could not be determined reliably in the separate inversions.

2.3.3. Comparison With Seismological Moho Depth Models

Although the applied inversion methodology is taking account of the seismic-inferred depth points, the resulting Moho depth model still has to reproduce the gravity data and is not expected to fit the seismic data perfectly. This is reflected in Figure 2.6 (bottom) by the small mismatch in the gravity signal (RMS $\approx$ 3.5 mgal) and the relatively high residual in the Moho depth (RMS $\approx$ 8 km). While in Figure 2.6 the gravity-inverted Moho depth is compared with the seismic points (indicated by the colored circles), Figure 2.8 shows the complete depth differences between the gravity-inverted and the areal seismological models.

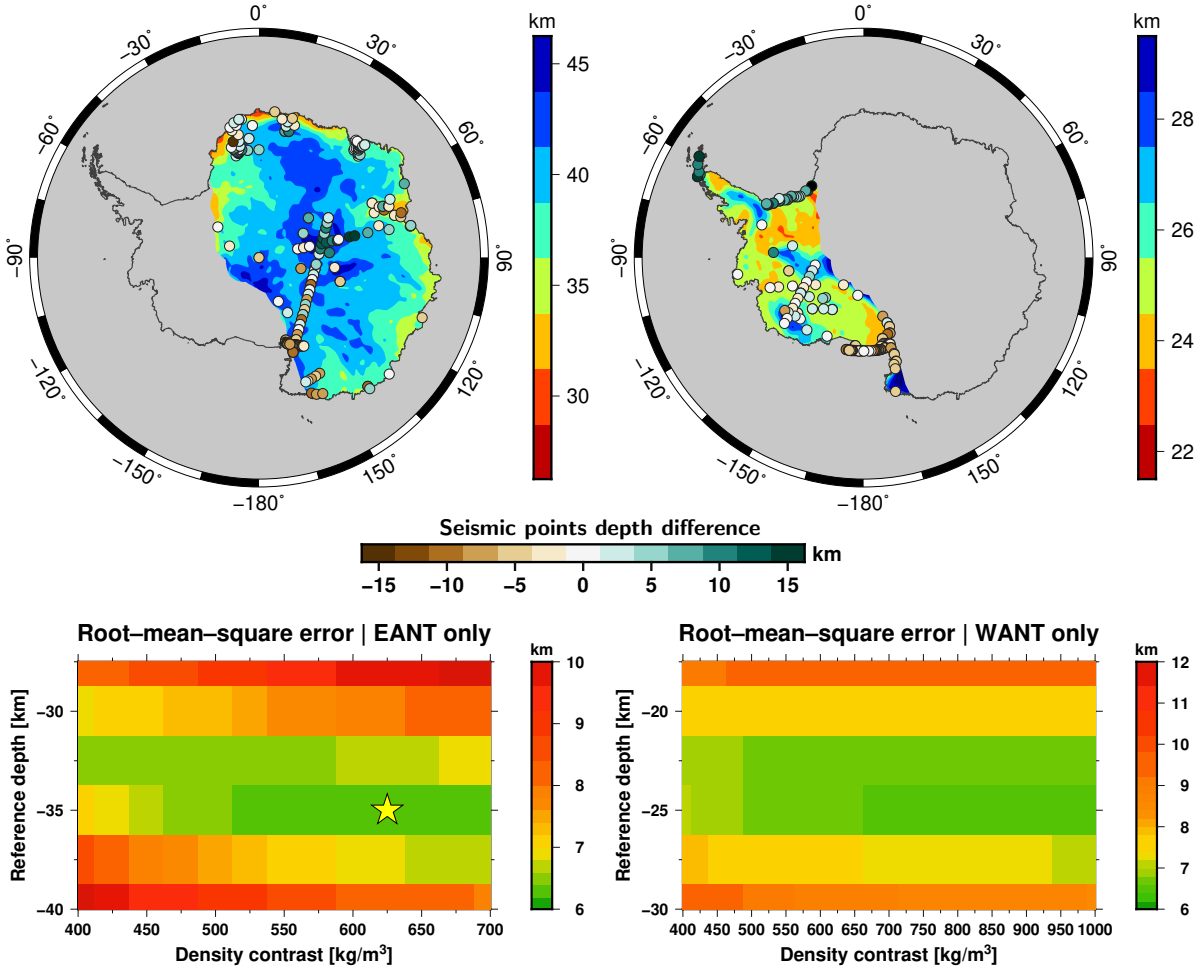

Figure 2.7.: Top: resulting Moho depth maps from the inversion with separate seismic points for EANT (left) and WANT (right). The colored circles indicate the differences in depth between the seismic estimate and the inverted depth. Bottom: root mean square error of gravity-inverted Moho depth to seismic points. While still a rather clear optimum could be found for EANT at z_{ref} = 35 km and $\Delta\rho$ = 625 kg/m^3, the inversion for WANT shows only a distinct reference depth of ~25 km. The density contrast, on the other hand, is rather diffuse, which is pointing toward a strong heterogeneity in the area. WANT=West Antarctica; EANT=East Antarctica.

Large parts of EANT are within the typical range of seismological uncertainty in Moho depth estimation (approximately ±4 km). On the other hand, strong differences occur beneath the GSM and in Queen Elizabeth Land (compare Figure 2.1) for both models. The TAM, in particular their southernmost part, and whole WANT have a much higher crustal thickness in the gravity-inverted models than seismic estimations indicate. The same pattern is reflected by the gravity misfit of the original seismological models (Figure 2.4).

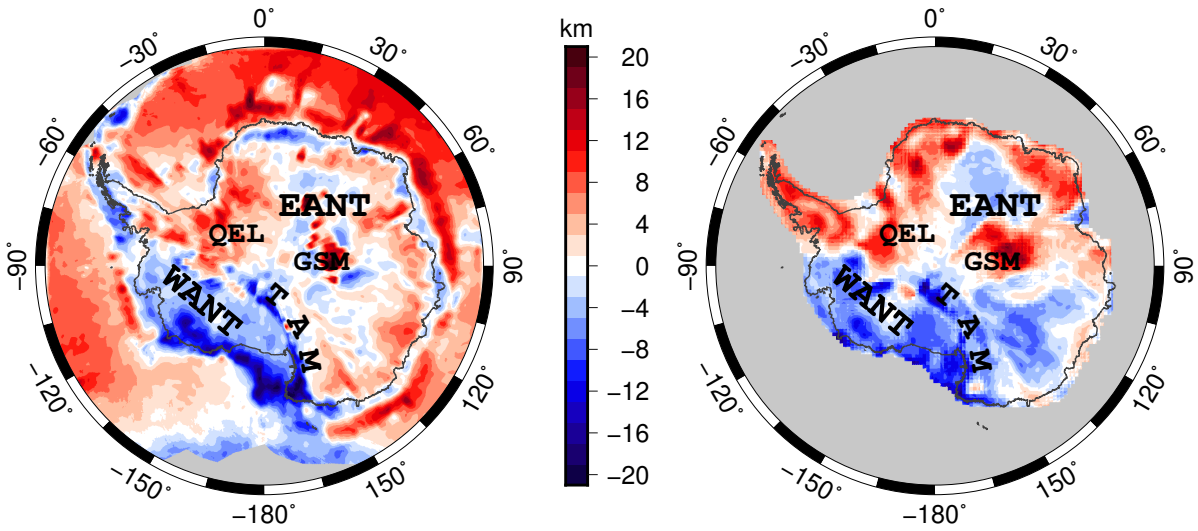

Figure 2.8.: Depth difference between gravity-inverted and seismological Moho depth models (left: AN1; right: ANT). Most parts are within the typical uncertainty range of seismological methods. Both seismological models indicate greater Moho depth beneath QEL and the GSM than the gravity inversion. WANT=West Antarctica; EANT=East Antarctica; GSM=Gamburtsev Subglacial Mountains; QEL=Queen Elizabeth Land; TAM=Transantarctic Mountains.

2.3.4. Comparison With Isostatic Moho Model

The discrepancies between the seismological Moho depth estimations and the gravity signal raise questions about the mass distributions within the Antarctic lithosphere and its isostatic state. For the purpose of this comparison, we calculate simple Airy-isostatic Moho depth models for the continent, using the same values for reference depth and density contrast as derived from the inversion (Figure 2.9). The residual map reveals strong deviations from Airy-isostasy when applying a single density contrast at the Moho boundary. These patterns are congruent with those of the gravity disturbance (Figure 2.2) and the gravity residual resulting from the Airy-isostatic crustal model (Figure 2.9). Most prominent are the TAM and Wilkes Land, where the gravity-inverted Moho depth is up to 10 km deeper than Airy-isostasy is suggesting. The GSM and Dronning Maud Land are almost not visible in the residual map.

However, in both residual maps we can identify a different signature not only for WANT and EANT but also within EANT itself: between the TAM and the proposed Indo-Australo-Antarctic Suture (Aitken et al., 2014), where Indo-Antarctica and Australo-Antarctica may have collided either during the late Mesoproterozoic or as late

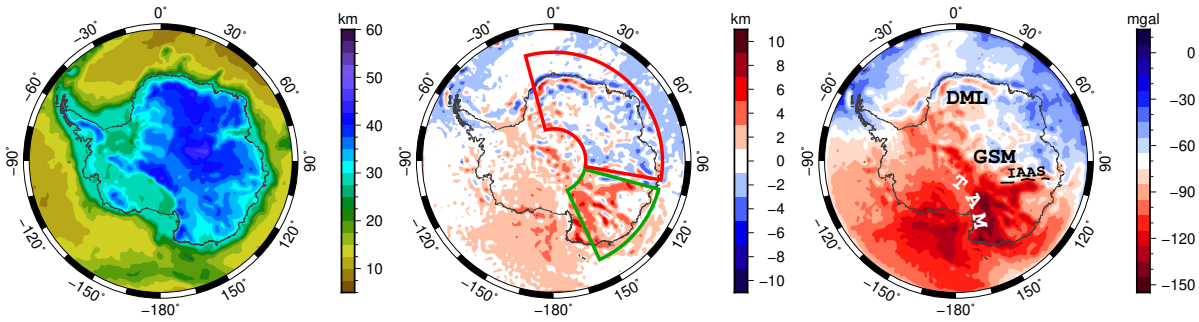

Figure 2.9.: Left: Airy-isostatic Moho depth calculated with density contrast and reference depth from the inversion with combined seismic data point set; center: depth difference between gravity-inverted and Airy-isostatic Moho; right: gravity residual resulting from the Airy-isostatic Moho. IAAS=Indo-Australo-Antarctic Suture; DML=Dronning Maud Land; TAM=Transantarctic Mountains.

as the early Cambrian (Boger, 2011; Collins and Pisarevsky, 2005), the residual is substantially lower than for the rest. This may either point at different modes of isostatic compensation (e.g. lithospheric mantle densities) or imply that topography is partly supported by dynamic (i.e. deeper mantle) effects.

2.4. 2-D Lithospheric Cross-Sections

Our analysis shows that the mass distribution in the crust and upper mantle is expected to have a significant role in the isostatic state and gravity field of Antarctica. In the following, we discuss the potential upper mantle contribution by 2-D modeling across the Wilkes Subglacial Basin region of EANT in particular.

As mentioned previously, large disagreements exist between different Moho depth models and studies in EANT. Moho depth estimates from seismological studies differ for the same station by up to 10 km, even along a relatively well-studied profile (Figure 2.10). The profile stretches from the TAM to the GSM (Paxman et al., 2016; Creyts et al., 2014) crossing the southern Wilkes Subglacial Basin (Paxman et al., 2019, 2018; Jordan et al., 2013; Ferraccioli et al., 2009a; Studinger et al., 2004; Ferraccioli and Bozzo, 2003; Ferraccioli et al., 2001). Seismic data have been acquired by deployments from the TAMSEIS (Hansen et al., 2009; Lawrence et al., 2006a,b) and the GAMSEIS (Kanao et al., 2014) experiments. Yet the respective studies are not consistent and yield different Moho depth estimations, ranging from a relatively shallow (~33 km, Rayleigh wave analyses; Lawrence et al., 2006b) to a significantly deeper (~43 km,

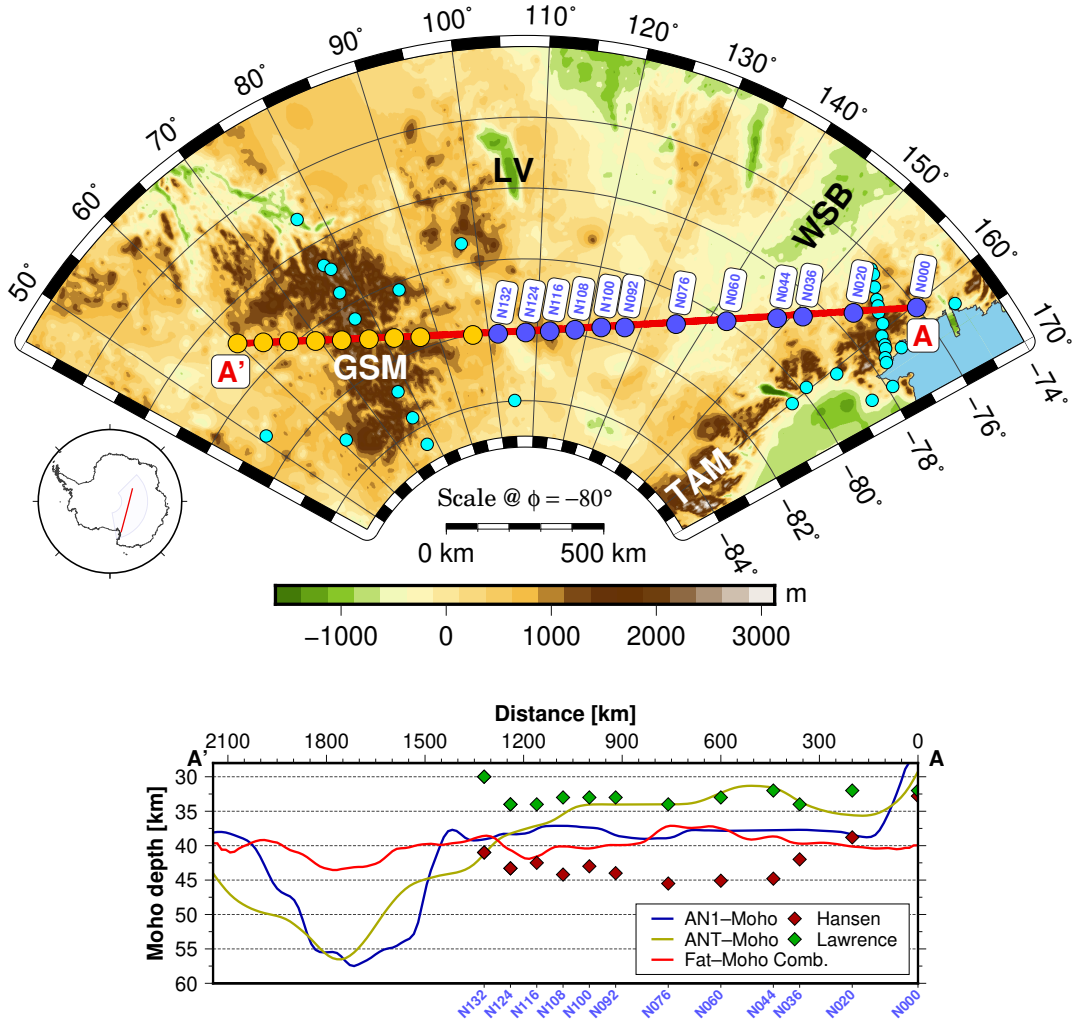

Figure 2.10.: Top: Bedrock topography (Fretwell et al., 2013) with combined profile (A–A') of seismic stations from the Trans-Antarctic Mountain Seismic Experiment (blue circles) and Gamburtsev Mountain Seismic experiment (orange circles) surveys. Cyan-colored circles indicate further seismic stations used to constrain the AN1-Moho model. GSM=Gamburtsev Subglacial Mountains; LV=Lake Vostok; TAM=Transantarctic Mountains; WSB=Wilkes Subglacial Basin. Bottom: Moho depth estimations from different studies: Rayleigh wave analyses from Lawrence et al. (2006b) show a shallow Moho at ~30 km (green diamonds), while *S* wave receiver functions from Hansen et al. (2009) indicate an ~10-km deeper Moho (red diamonds). Solid lines indicate depth of seismic (AN1-Moho and ANT-Moho) and gravity-inverted Moho with combined point set.

S wave receiver functions; Hansen et al., 2009) Moho beneath the southern Wilkes Subglacial Basin. Similar discrepancies exist between the AN1-Moho model (deep), which incorporates estimates from Hansen et al. (2009), and the ANT-Moho model (shallow), involving results from Lawrence et al. (2006b). Such a considerable differ-

ence of ~10 km in crustal thickness has, of course, strong implications for the characteristics of the crust itself and the underlying mantle in terms of density, temperature, and composition and therefore the tectonic and geodynamic history of the region. In case of pure Airy-isostasy, for example, 10 km in crustal thickness would correspond to 1500 m in topography, when assuming a rock density of 2670 kg/m^3 and a Moho density contrast of 400 kg/m^3. Figure 2.10 (bottom) shows the different Moho depth estimates along the profile. For purpose of comparison, the gravity-inverted Moho based on the combined seismic point set is shown as well. Its huge deviations from the seismic estimates again illustrate the consequences of neglecting varying crustal and mantle densities, particularly in the GSM region, where a very low density contrast of ~55 kg/m^3 at the crustal root has been modeled in order to fit both gravity and seismologically derived estimates of crustal thickness (Ferraccioli et al., 2011).

In order to examine in further detail the crustal and lithosphere properties that would be required in the thick versus thin crust scenario for the southern Wilkes Subglacial Basin, we use LitMod2D v1.6 (Afonso et al., 2008), a software that has successfully been applied in a number of studies (e.g. Jones et al., 2014). It solves the corresponding equations for conductive heat flow, thermodynamic, geopotential, and isostasy in the finite differences method simultaneously. Output data are density, temperature and pressure fields, surface heat flow, seismic body wave velocities, geoid, gravity anomalies, and isostatic elevation (topography). The underlying properties are functions of temperature, pressure, and composition. In case of mantle material, they are thermodynamically modeled with the software Perple_X (Connolly, 2005) based on a predefined peridotitic composition. Further details of the methodology are described in Afonso et al. (2008). According to the different Moho depth estimates, we set up two alternative models along the model profile (Figure 2.10): one with a shallow and one with a deep Moho boundary.

Petrological properties are required as input parameters for crust and mantle. We use values for bulk density, thermal expansion coefficient, and compressibility (Table 2.1) of the crustal layers that result in *in situ* densities being thought to represent a global average (e.g. Rudnick et al., 1998; Christensen and Mooney, 1995, and references therein). For thermal parameters (heat production and thermal conductivity), we take the same values as An et al. (2015a, and references therein) to get comparable results. The petrology of the upper mantle of central EANT is unknown, but it has been speculated that an igneous and metamorphic belt of Mesoproterozoic (1–1.4 Ma)

Body No.	Type	Heat prod.	Therm. cond.	Density	Compressibility
Model with deep Moho after Hansen et al. (2009)					
1a	Upper crust	1.0	2.1	2.65	6e-11
1b	Upper crust	1.0	2.1	2.80	5e-11
2a	Lower crust	0.4	2.1	2.70	6e-11
2b	Lower crust	0.5	2.2	2.80	6e-11
		($\mu W/m^3$)	(W/mK)	(g/cm^3)	GPa^{-1}
Model with shallow Moho after Lawrence et al. (2006b)					
1a	Upper crust	1.0	2.1	2.65	6e-11
1b	Upper crust	1.0	2.1	2.78	5e-11
2a	Lower crust	0.4	2.1	2.70	6e-11
2b	Lower crust	0.3	2.2	2.78	7e-11
		($\mu W/m^3$)	(W/mK)	(g/cm^3)	GPa^{-1}

Table 2.1.: Petrophysical parameters of crustal layers in the 2-D models. The body numbers correspond to Figure 2.11.

age is present at crustal levels on the periphery of the GSM (Goodge et al., 2017; Elliot et al., 2015; Ferraccioli et al., 2011). Thus, we assume a mean Proterozoic lithospheric mantle composition beneath the interior of EANT in our models. However, seismic *S* wave and Rayleigh wave velocity studies beneath the 250-km-thick (An et al., 2015a) craton indicate that the lithosphere of the GSM region may have been formed during earlier Archaean and Paleoproterozoic times (Heeszel et al., 2013). Following these seismic interpretations, we introduce a lithospheric mantle of Archaean composition in our models beneath the GSM. In our modeling, we use the oxide compositions for representative Phanerozoic, Proterozoic, and Archaean peridotites from Afonso et al. (2008).

2.4.1. Results and Discussion

We fitted the models to topography and geoid by minor adjustments of crustal densities (see Table 2.1 for the parameters used and compare upper and lower table), Moho depth, and lithospheric thickness. The modeled lithospheric density structure (Figure 2.11, bottom) directly affects the resulting geoid and isostatic elevation, which in turn are used as constraining observables. While the model with the shallow

Moho beneath the southern Wilkes Subglacial Basin could be fitted with a uniform lithospheric mantle of Proterozoic composition, the deep Moho boundary required a denser lithospheric mantle to be in isostatic balance. Overall, both the deeper and the shallower Moho scenarios can fit the topography and geoid but require different mantle compositions.

Further comparison with upper mantle *S* wave velocities (An et al., 2015b) and surface heat flow (An et al., 2015a) can be done for model validation and discussion. Remarkably different geothermal heat flow estimations exist for Antarctica (e.g. Martos et al., 2017; Fox Maule et al., 2005; Shapiro and Ritzwoller, 2004). Here we compare our predictions to the heat flux estimates from An et al. (2015a) since they originate from a similar model setup (conductive heat transfer within the lithosphere) and are thus best suited for our 2-D modeling purposes. The calculated surface heat flow of both 2-D models (Figure 2.11) is in the range of heat flow data provided by An et al. (2015a). Notably, the largest effect is in the coastal region of the TAM (close to profile point A) where heat flow differs from 55 to more than 65 mW/m^2 between the two models. Such a difference would be expected to have a significant effect in modeling of the ice sheet history (e.g. Rogozhina et al., 2012) and estimates of present-day basal melting rates, which in turn can influence subglacial hydrology and ice sheet dynamics. Regarding seismic velocities, both models are in first-order agreement with the *S* wave model from An et al. (2015b) down to a depth of ~150 km (Figure 2.12). At profile kilometer 1200–1300, a transition from low to high velocities takes place at depths of 50–150 km, which is a response to the thick underlying lithosphere. However, the LitMod2D framework assumes an adiabatic temperature gradient in the sublithospheric mantle and does not include thermal anomalies there. Thus, the seismic velocities are only comparable when assuming thermal steady state. Considering that, the slightly better resemblance of the deep Moho model with the AN1 velocity model should not be considered as a robust indication of a more realistic model. The comparison of *S* wave velocities alone cannot validate or reject one of the two models, either.

A depleted mantle composition of Proterozoic age that would best fit with the thick crust scenario would be consistent with the hypothesis that the Mawson Craton of Archaean-Paleoproterozoic age that comprised the Antarctic Terre Adélie Craton and the Australian Gawler Craton prior to Gondwana breakup extends to our model profile and may extend even much further south to the Shackleton Range in Queen Elizabeth Land (Paxman et al., 2017; Boger, 2011). The notion that the Mawson Craton

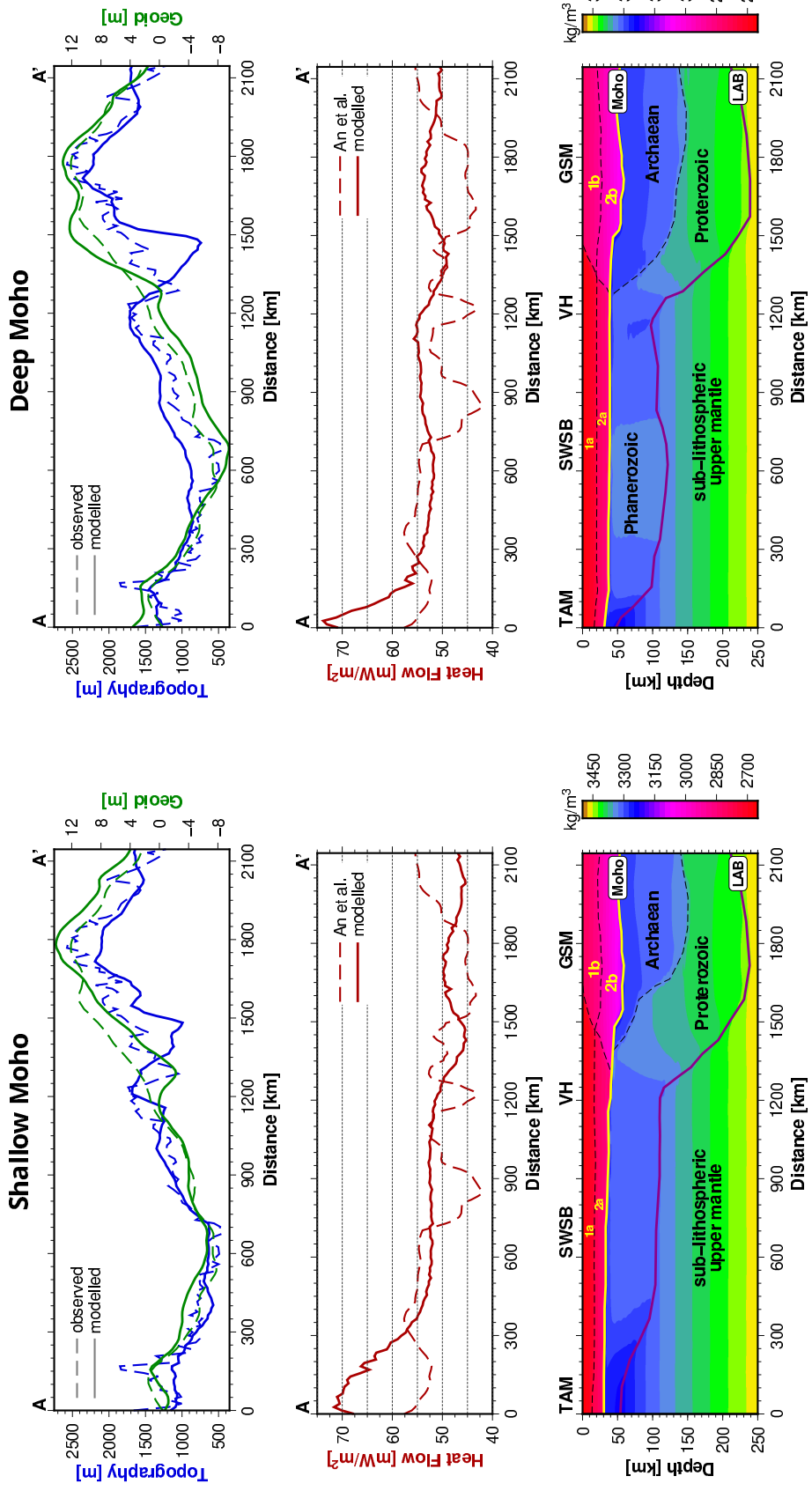

Figure 2.11.: LitMod2D modeling results along the profile shown in Figure 2.10. Left: thin crust after Lawrence et al. (2006b); right: thick crust after Hansen et al. (2009). Both models are fitted for topography and geoid (top) and are largely consistent with heat flow estimations. A thick crust requires higher lithospheric mantle density to be in isostatic equilibrium. TAM=Transantarctic Mountains; SWSB=Southern Wilkes Subglacial Basin; VH=Vostok Highlands; GSM=Gamburtsev Subglacial Mountains.

extends to our study area is also supported by independent observations from surface geology in the central TAM and from studies of glacial erratics. Detrital zircons from Lake Vostok, for example, are partly dated to 1.6–1.8 Ga (Leitchenkov et al., 2016) and have potentially been transported from ice sheet-covered cratonic terrains located in the Wilkes Land region. Goodge et al. (2017) collected and analysed glacial clasts in the central TAM region, relatively close to our modeling profile. Their results indicate that ~1.6-Ga magmatic belts of the Gawler Craton may extend into central EANT. The transport distance of the individual clasts, however, is uncertain. Distinctly younger ages (ca. 1.3 to 1.0 Ga) are also observed, and their origin could be located in a putative ~1000-km-distant source region in the GSM province, where Ferraccioli et al. (2011) hypothesized that a major coeval orogenic belt exists, based on their aeromagnetic and airborne gravity interpretation. Aeromagnetic studies also suggest that the cratonal margin of EANT, at least at crustal level, gets much closer to the coast along our modeling profile compared to the northern parts, where the Ross Orogen appears to be considerably wider (Golynsky et al., 2018; Ferraccioli et al., 2009a,b, 2002).

As this sector of the Mawson Craton and the Ross Orogen in EANT were formerly contiguous with the Gawler Craton and the Delamerian Orogen in Australia, respectively (e.g. Finn et al., 1999), it is useful to make some first-order comparisons between these two continents in terms of crustal thickness estimates. Seismic crustal thickness estimates of 30–35 km have been derived for parts of the Delamerian Orogen in South Australia (Salmon et al., 2013; Kennett et al., 2012, 2011), suggesting that this subduction-related orogenic belt did not lead to major crustal thickening. A similar setting may be envisaged in particular for the back-arc regions of the Ross Orogen that may in parts underlie the Wilkes Subglacial Basin (e.g. Jordan et al., 2013; Ferraccioli et al., 2009a). However, there are complicating effects in EANT, due to the much more recent Cenozoic uplift of the TAM (at the former site of the Ross Orogen) and the associated lithospheric flexure of the craton and its margin beneath the Wilkes Subglacial Basin (e.g. Paxman et al., 2019, 2018, and references therein). Irrespectively, however, we also note that some potentially conjugate Precambrian terranes in Australia that lie along the eastern edge of the Gawler Craton appear to have anomalously thick crust, most notably the seismically defined Numil terrane that has crust up to 45 km thick close to a proposed major suture zone of inferred Paleoproterozoic or even older Archaean age (Curtis and Thiel, 2019; Betts et al., 2016). Another potentially conjugate craton region for the Wilkes Subglacial Basin basement is the Australian Curnamona Craton that is also underlain by 40- to 45-km-thick crust (Salmon et al., 2013; Kennett

et al., 2012, 2011). Taken together, this comparison with crustal thickness patterns observed over the much better understood Australian continent coupled with previous aeromagnetic interpretations and geological studies in this sector of EANT tends to lend more weight to the Proterozoic lithosphere model beneath the TAMSEIS seismic line.

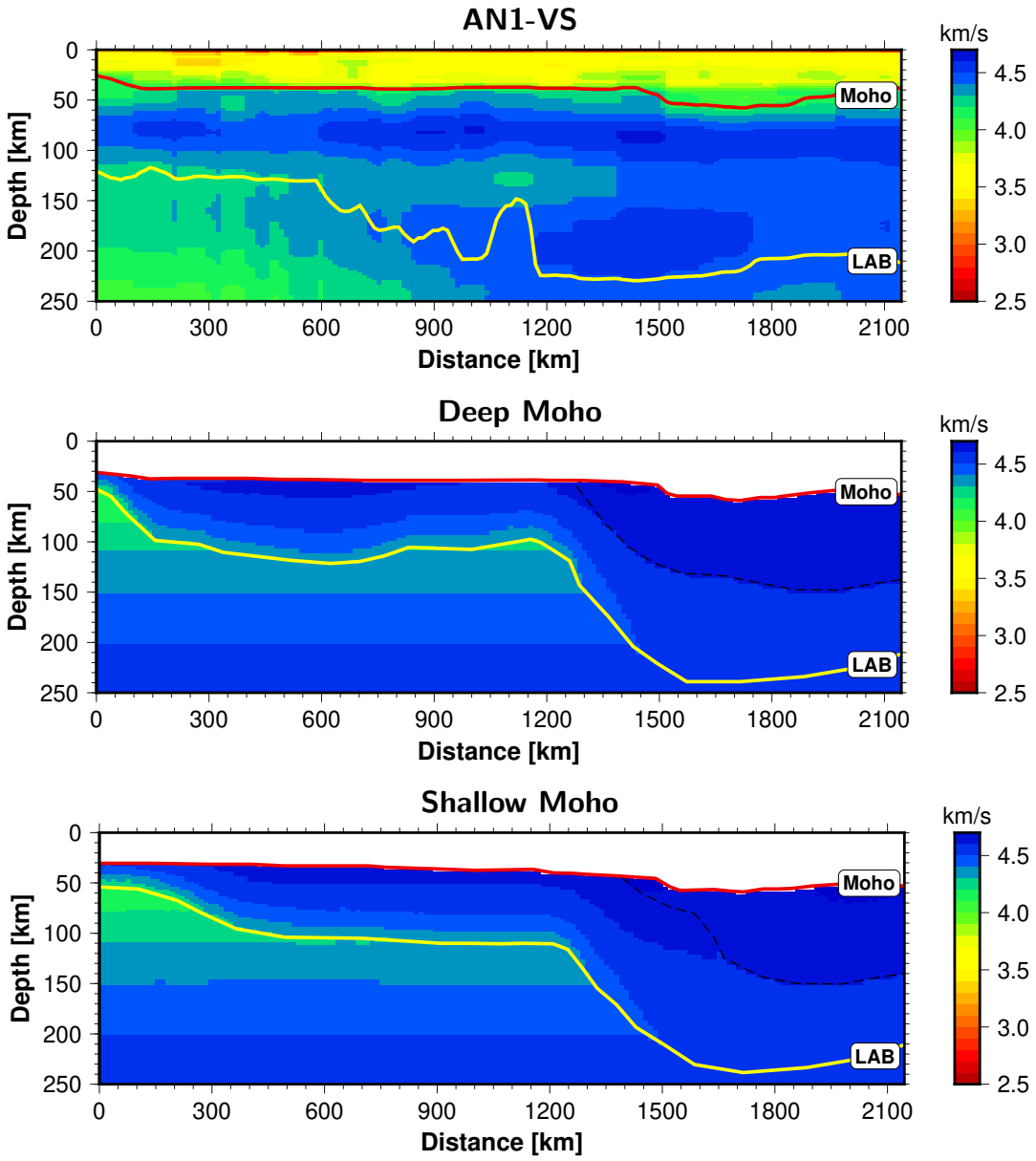

Figure 2.12.: *S* wave velocities for the alternative models. Top: velocity model from An et al. (2015b); middle and bottom: velocities from LitMod2D models. Although the amplitude differs (partly due to the choice of attenuation parameters), the velocity pattern is widely similar down to a depth of 150 km. In the LitMod2D models only mantle velocities are calculated.

The younger and more fertile Phanerozoic lithospheric mantle composition, which is required in the model with a deep Moho beneath the southern Wilkes Subglacial Basin, is instead apparently inconsistent with the presumed Proterozoic age of the crust (Goodge et al., 2010). However, this model cannot be ruled out either, considering the broader tectonic history of the region: the inherited TAM margin formed in the course of the late Neoproterozoic breakup of Rodinia (Elliot et al., 2015; Goodge and Finn, 2010) and extensive subduction-related metamorphism and magmatism took place during the subsequent Ross Orogeny in Cambrian-Ordovician times (Elliot et al., 2015; Goodge et al., 2012; Ferraccioli et al., 2009a,b, 2002). Considering the above, far-field effects of Ross-age subduction in an inferred back-arc setting for the WSB region (Ferraccioli et al., 2009a) could potentially have affected the degree of depletion of the mantle lithosphere beneath the hinterland of the TAM. Overall, it is possible that subduction-related processes may have led to a refertilization of the lithospheric mantle over a broader area than surface exposures or interpretations of crustal geology alone appear to support. We contend that ruling out either the thinner or the thicker crust models for the Wilkes Subglacial Basin is therefore somewhat premature based on our alternative 2-D end-member models alone. Overall, it is clear that more extensive seismological station coverage is required to reduce the ambiguities in crustal and lithospheric modeling in this remote frontier of EANT.

2.5. Conclusions

Our inversion results of the Moho depth of Antarctica from satellite gravity data, constrained by independent seismological estimates, are broadly consistent with previous gravity studies (O'Donnell and Nyblade, 2014; Block et al., 2009). Our main results and conclusions are summarized hereafter:

1. A strong contrast in crustal thickness is confirmed between WANT (~25 km) and the composite East Antarctic Craton (~40–45 km) and the larger misfits between gravity inversions and seismologically derived estimates of Moho depth likely stem from different density contrasts at the Moho in these geologically distinct parts of the continent. A separate inversion for West and EANT therefore provides a better fit to the seismic constraints and thus yielded improved Moho depth estimates. However, we found that the different density contrasts at the Moho could not be resolved reliably from gravity inversions alone, especially

beneath WANT, suggesting that there could be significant additional variability in upper mantle densities beneath the different Phanerozoic domains that make up WANT.

2. By comparing our results with an Airy-isostatic Moho depth model we showed that different modes of compensation likely exist in EANT and WANT. Notably, we found that the region of Wilkes Land also differs considerably from the rest of EANT. It is therefore reasonable to conclude that some sectors of Antarctica may not be in isostatic equilibrium and that significant additional buoyancy contributions from the lithospheric mantle are present even in EANT, in general agreement with the findings of O'Donnell and Nyblade (2014).

3. In our quest to better comprehend crustal and deeper lithospheric architecture in interior EANT, we performed targeted 2-D lithospheric modeling over the southern Wilkes Subglacial Basin region along the TAMSEIS–GAMSEIS passive seismic profile. We showed that a shallow Moho beneath the basin can be fitted by introducing a moderately depleted lithospheric mantle composition, which would match well with the notion of a Proterozoic age lithosphere underlying the region. An alternative end-member model with a deeper Moho fits the satellite gravity and the topography equally well but requires a higher mantle density, as might be expected for a younger and more fertile Phanerozoic lithospheric mantle. Although the latter model appears to be at odds with our current knowledge of this part of the Mawson Craton, based on surface geology, erratics, and interpretations of aeromagnetic anomaly data, we propose that it cannot be ruled out either. For example, far-field effects of Ross-age subduction in a distal back-arc setting (Ferraccioli et al., 2009a, 2002) could in principle have modified the original Proterozoic lithosphere beneath parts of the Wilkes Subglacial Basin, affecting the degree of depletion of the mantle lithosphere. Given the importance of validating or refuting these competing models for the crustal structure of the Wilkes Subglacial Basin, both for comprehending the processes that affected the margin of the composite East Antarctic Craton and for geothermal heat flow estimation, we recommend new seismological deployments in this frontier region, coupled with the development of enhanced 3-D lithosphere modeling approaches.

Chapter 3

Modeling Satellite Gravity Gradient Data to Derive Density, Temperature, and Viscosity Structure of the Antarctic Lithosphere

F. Pappa[1], J. Ebbing[1], F. Ferraccioli[2], W. van der Wal[3]

[1] Department of Geosciences, Kiel University, Kiel, Germany
[2] British Antarctic Survey, Cambridge, UK
[3] Delft University of Technology, Delft, The Netherlands

Published in: *Journal of Geophysical Research: Solid Earth*, 124.
https://doi.org/10.1029/2019JB017997

3.1. Introduction

The structure of the Antarctic lithosphere is still less known than that of other continents. Agreement exists on a difference in lithospheric structure between West Antarctica (WANT) and East Antarctica (EANT) divided by the Transantarctic Mountains (TAM) and the Antarctic Peninsula (e.g. Torsvik and Cocks, 2013, Figure 3.1). WANT comprises several distinct Paleozoic to Mesozoic fore-arc and magmatic-arc terranes (Dalziel and Elliot, 1982) and the Ellsworth-Whitmore terrane with Grenville-age crust (Craddock et al., 2017). Multiple phases of rifting took place from Cretaceous to Cenozoic times in the West Antarctic Rift System (WARS; e.g. Jokat and Herter, 2016;

Fitzgerald, 2002) and earlier rifting commencing in the Jurassic in the Weddell Sea region (e.g. Jordan et al., 2017b). The tectonic history of EANT is characterized by several phases of accretionary or collisional events in the Precambrian (Boger, 2011). Thus, EANT is now widely recognized to comprise several lithospheric provinces of different origin and age, ranging from Archaean and Paleoproterozoic to Cambrian (Elliot et al., 2015; Harley et al., 2013; Torsvik and Cocks, 2013; Ferraccioli et al., 2011; Boger, 2011, and references therein).

Seismological methods are well suited for assessing the internal structure of the lithosphere. However, the remoteness and the harsh environment of the Antarctic continent make seismic experiments logistically and technically challenging. Recently, a number of seismological models for the Antarctic continent (e.g. Heeszel et al., 2016; Ramirez et al., 2016; An et al., 2015b; Hansen et al., 2014) or with focus on WANT and TAM have been published (e.g. White-Gaynor et al., 2019; Shen et al., 2018; O'Donnell et al., 2017; Ramirez et al., 2017; Graw and Hansen, 2017; Hansen et al., 2016; Lloyd et al., 2015), which show the clear differences in crustal thickness between EANT and WANT and to a notable extent the heterogeneous nature of the upper mantle. However, density models derived from seismic observations generally lead to predicted gravity anomalies that differ greatly from observed values (Pappa et al., 2019a) and therefore exhibit significant inconsistencies. Beyond that, gravity data or combinations of gravity and seismic data have been used to estimate the crustal thickness for the entire Antarctic continent (Baranov et al., 2018; O'Donnell and Nyblade, 2014; Block et al., 2009). Even though the main features are similar in these models, considerable disagreement exists in some regions, for example, in Wilkes Land or eastern Dronning Maud Land (DML) where seismic and gravity estimates of crustal thickness differ by over 10 km.

Alternatively, satellite gravity gradient data can be used in combination with seismological models to derive lithospheric models. The potential of satellite-based gravity gradients to establish regional models, which can be used as a background for local interpretations, has been demonstrated (Holzrichter and Ebbing, 2016; Bouman et al., 2015) and is especially useful for large, inaccessible areas such as the Antarctic continent (Ebbing et al., 2018). Since the gravity gradients possess different sensitivities for different depth ranges (Bouman et al., 2016), they are particularly suited to investigate the mass distribution within the lithosphere. Still, gravity gradient data alone are not sufficient to uniquely constrain density.

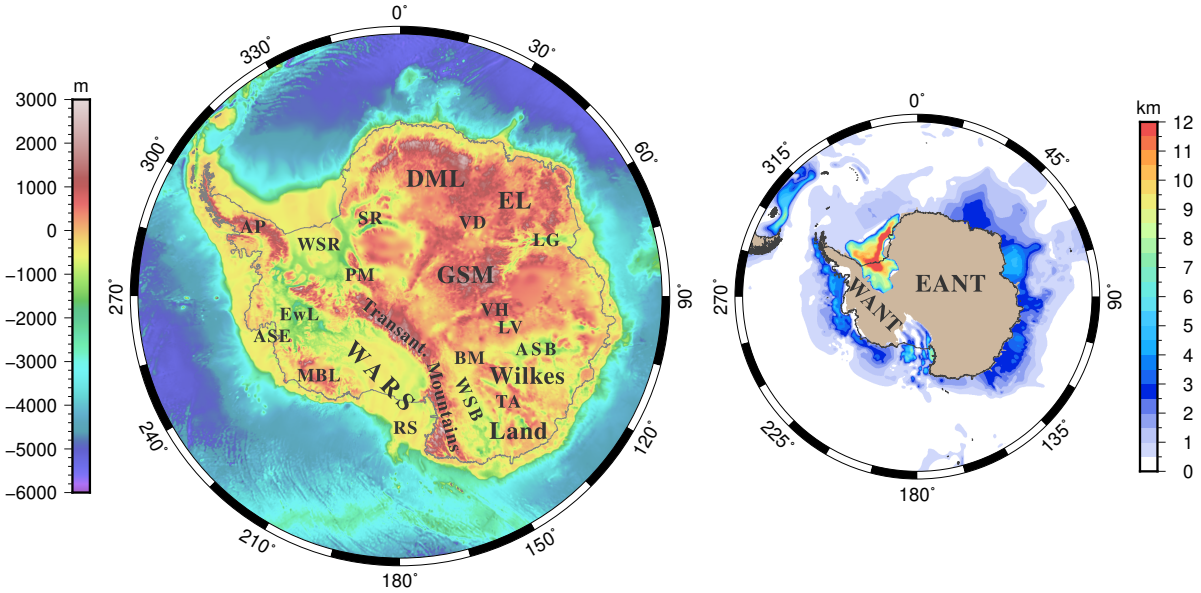

Figure 3.1.: (left) Bedrock topography of Antarctica. AP=Antarctic Peninsula, ASB=Aurora Subglacial Basin, ASE=Amundsen Sea Embayment, BM=Beardmore Microcontinent, DML=Dronning Maud Land, EL=Enderby Land, EwL=Ellsworth Land, GSM=Gamburtsev Subglacial Mountains, LG=Lambert Graben, LV=Lake Vostok, PM=Pensacola Mountains, RS=Ross Sea, SR=Shackleton Range, TA=Terre Adélie, VD=Valkyrie Dome, VH=Vostok Highlands, WARS=West Antarctic Rift System, WSB=Wilkes Subglacial Basin, WSR=Weddell Sea Rift. (right) Sediment thickness data compilation used in this study. Sources are described in the main text. EANT=East Antarctica, WANT=West Antarctica.

Few studies so far have tried to jointly investigate the crust and upper mantle (e.g. Haeger et al., 2019; An et al., 2015b,a) of EANT, which is needed to better understand the fundamental structure of the lithosphere as a whole. Seismic velocities and rock densities depend on temperature and composition, which can be modeled by minimizing the Gibbs energy or described in simplified terms by other petrophysical parameters such as thermal expansion and compressibility. An et al. (2015a) estimated the temperature of the Antarctic lithosphere and upper mantle through conversion of seismic velocities (An et al., 2015b) by using a homogeneous non-cratonic mantle composition. However, uncertainties caused by the potential presence of melt or fluid or linked to the choice of the anelasticity model adopted are higher than those arising from compositional variations within the lithosphere and remain difficult to fully resolve. The resulting temperature model was however an important step toward a better understanding of the state of Antarctica's lithosphere. Haeger et al. (2019) compiled existing seismological crustal thickness estimates and used satellite

gravity data to isolate the gravity signal from the lithospheric mantle. By also utilizing seismological velocity models, they iteratively derived a density, temperature, and compositional model of the Antarctic lithosphere. Their methodology, however, relies on the validity of the crustal model adopted, which is subject to high uncertainties.

An alternative approach is to incorporate the whole lithosphere and sublithospheric upper mantle in one model. In addition, integrated modeling of both geophysical and petrological properties of rocks in a self-consistent framework can help to reduce the uncertainties associated with modeling the observables separately (Fullea et al., 2012). This approach has proved valuable for investigation of the lithospheric structure in several studies (e.g. Fullea et al., 2015; Jones et al., 2014). The inferred temperature structure of a lithospheric model obtained by this process can also be used to also estimate sublithospheric upper mantle viscosity. Seismological models are typically used to derive a 3-D Earth viscosity structure. Nield et al. (2018) explored the effect of applying 3-D viscosity distribution instead of classical 1-D models on Antarctica and have shown that such models are crucial to obtain more accurate spatial patterns of glacial isostatic adjustment (GIA). However, deriving 3-D viscosity from seismological models introduces uncertainties from the seismological data and from the conversion methodology.

In this study we use satellite gravity gradient data, the principle of isostasy, and thermodynamic modeling of mantle petrology to derive a self-consistent 3-D lithospheric density and temperature model of the Antarctic continent. New crustal and lithospheric thickness estimates are obtained and compared with previous studies. The modeled upper mantle temperature field is then used to derive viscosity values and to compute present-day uplift rates due to GIA.

3.2. Data

The gravity gradients are the second derivative of the gravitational potential. They are generally more sensitive to shallower structures than the vertical gravity field, which makes them a useful tool to study the density structure of the lithosphere (Bouman et al., 2016). During the years 2009–2013 European Space Agency's satellite mission Gravity Field and Steady-State Ocean Circulation Explorer measured the gradients of the Earth's gravity field at an average altitude of 255 km at the beginning

of the mission and 225 km at the end of the mission. For our study we use the gravity gradient grids at 225-km height (Figure 3.2) from Bouman et al. (2016). Commonly, gravity gradient data are expressed as tensor components in a North-West-Up frame, which is suitable for regions of intermediate latitudes, but leads to unintuitive maps in polar regions. By performing a tensor basis change, we adopt a local reference system for Antarctica. In this new IAU reference frame, the directions of derivation point to India (I; 90° E) and to the Atlantic Ocean (A; 0° E), that is, right and top in an Antarctic polar stereographic map, while the vertical axis (U; upward) remains unchanged. The components of the gravity vector T are rotated as a function of the longitude λ according to the following:

$$\begin{pmatrix} T_i \\ T_a \\ T_u \end{pmatrix} = \begin{pmatrix} \sin\lambda & \text{-}\cos\lambda & 0 \\ \cos\lambda & \sin\lambda & 0 \\ 0 & 0 & 1 \end{pmatrix} \begin{pmatrix} T_n \\ T_w \\ T_u \end{pmatrix} \tag{3.1}$$

A complete derivation of Equation 3.1 is presented in section A.4.

To isolate the gravity gradient signal from the lithosphere, we first need to correct for the effect of topography, water, ice, and sediments. To achieve this, we use density values for water ($\rho_{\text{water}} = 1028\,\text{kg/m}^3$), ice ($\rho_{\text{ice}} = 917\,\text{kg/m}^3$), and bedrock elevation ($\rho_{\text{topo}} = 2670\,\text{kg/m}^3$). The values adopted for ice thickness and topography were derived from the Bedmap2 Antarctic compilation (Fretwell et al., 2013). The Bedmap2 model describes the ice thickness and the bedrock topography (Figure 3.1) of Antarctica up to latitude 60° S and is mainly based on airborne radar surveys. Even though some areas are not well covered and exhibit large uncertainties up to >1000 m, it is the most accurate ice thickness model currently available for Antarctica. (The effect of the uncertainty in the Bedmap2 model on the gravity gradients at satellite altitude is shown in Figure A.4.) The gravity gradient effect of the individual units for the reduction is computed by discretization in tesseroids of ~11-km edge length south of 60° S and 0.5° edge length north of 60° S. A tesseroid is a segment of a sphere, delimited by upper and lower meridians and parallels plus by its top and bottom radii (as distance from the Earth's center). In addition to assessing the gravity effect, the topographic data are used as a constraint for isostasy in our modeling. Regarding this issue, the model does not explicitly include an ice layer, which is why we use the rock-equivalent topography, in which the ice layer is converted into a mass-equivalent layer of rock density (e.g. Hirt et al., 2012), to evaluate the isostatic state.

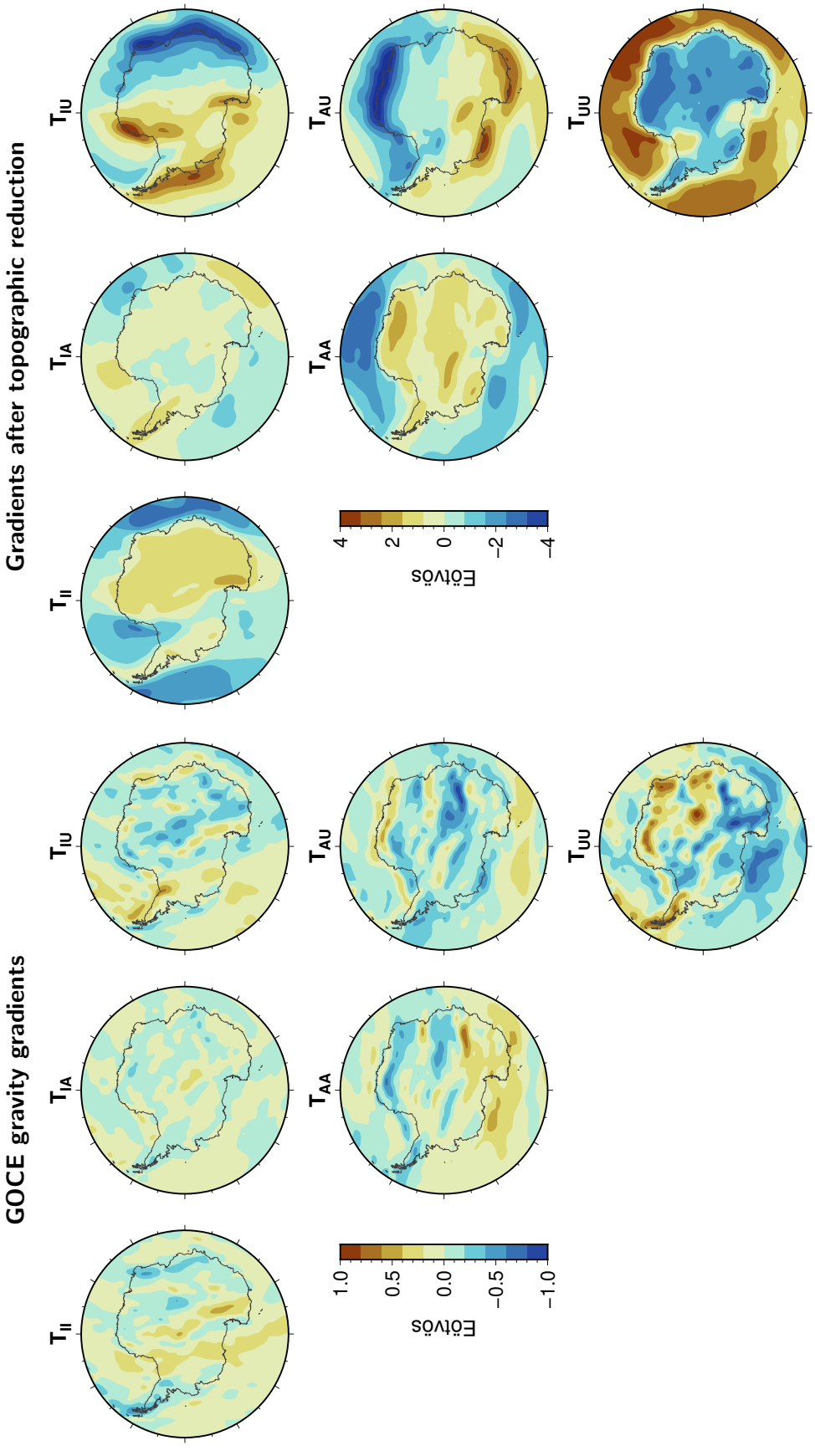

Figure 3.2.: (left) GOCE derived gravity gradients at 225-km altitude (Bouman et al., 2016). (right) The same data after reduction for effects of water, ice, rock topography, and sediments. Note the change of signal amplitude. GOCE=Gravity Field and Steady-State Ocean Circulation Explorer.

Several low-lying sectors of the Antarctic bedrock host major sedimentary basins, which can cause significant gravity anomalies, depending on their thickness and the density and porosity of the infill. To assess the effect of sedimentary thickness on the gravity gradient signal over Antarctica, we compiled available models and data (Figure 3.1). Few studies exist for onshore areas of the continent (e.g. Frederick et al., 2016; Aitken et al., 2014), where relatively high sediment densities are to be expected due to additional compaction from the thick ice sheet. Because the density is close to that of the surrounding crystalline rock, we do not include sedimentary basins in onshore areas to avoid inducing regional inconsistencies, which would emerge from omission of relatively unexplored basins. In offshore areas, we use National Geophysical Data Center's global 5-arc min grid (Whittaker et al., 2013), which provides ocean sediment thickness estimates up to 70° S. We complement these with the more detailed model from Wobbe et al. (2014), which also covers the Ross Sea, the Amundsen Sea, and the Bellinghausen Sea. A sedimentary thickness map for the Weddell Sea is available based on the magnetic data presented by Golynsky et al. (2001) and suggests up to 15-km-thick sediments there. Although it is difficult to derive the crystalline basement depth reliably from magnetic anomalies, we include this data set due to the lack of alternative areal sediment thickness information for the Weddell Sea. A potential overestimation may lead to erroneously low densities in the upper crust that would have to be compensated by modeled higher densities at greater depths. Further analyses of newly compiled Antarctic magnetic anomaly data (Golynsky et al., 2018) may help enhance our current knowledge of sedimentary basin thickness within the Weddell Sea and other interior parts of the continent.

For the sediment density, we use a simple exponential compaction model (e.g. Chappell and Kusznir, 2008). Thus, the sediment density ρ is related to the depth z in km from the sediment top as follows:

$$\rho = \rho_g + \left(\rho_w - \rho_g\right) \Phi e^{-\lambda z}, \tag{3.2}$$

where ρ_g is the grain density (set to $\rho_\mathrm{g} = 2670$ kg/m^3), ρ_w is the water density (set to $\rho_\mathrm{w} = 1028$ kg/m^3), Φ is the porosity of the uppermost sediment, and λ is the exponential decay constant. We use data from Sclater and Christie (1980), who provide $\Phi = 0.55$ and $\lambda = 0.4$ km^{-1} as representative values for mixed or unknown marine sediments. Global far-field gravitational effects are accounted for water and rock topography, using ETOPO1 topography (e.g. Amante and Eakins, 2009), which seamlessly extends the Bedmap2 model, with the same values for ρ_water and ρ_topo as

indicated above. Offshore sediments up to 30° S are also taken from the National Geophysical Data Center grid (Whittaker et al., 2013).

After subtraction of the effect of ice, water, bedrock topography, and sediment density anomaly from the observed gravity gradient data, a signal is obtained that should mainly reflect subsurface density variations in the crystalline crust and in the mantle (Figure 3.2). However, the remaining signal may still contain effects of an imperfect topographic reduction model or effects of deep mantle density heterogeneities. Moreover, the lithosphere may be in a state of isostatic disequilibrium due to ice mass changes in the past (O'Donnell et al., 2017). This GIA-induced displacement of the solid Earth can cause a gravity signal that should be considered if it is significant. The effect on the gravity gradients at satellite altitude (225 km), however, accounts at maximum for ~25 mE (Figure A.6), corresponding to less than 1% of the total signal, and is thus small enough to be neglected.

3.3. Modeling Methods

3.3.1. Lithospheric Modeling

A combined modeling framework of multiple geophysical quantities of the lithosphere and the sublithospheric upper mantle is provided by the forward modeling software LitMod3D (LIThospheric MODelling in a 3-D geometry; Fullea et al., 2009). It solves the equations for heat flow, thermodynamic properties of rocks, gravitation, and isostasy simultaneously in a finite differences method. Output quantities are density, temperature and pressure fields, surface heat flow, seismic body wave velocities, geoid, gravity anomalies, and isostatic elevation (topography). The underlying material properties are functions of temperature, pressure, and composition. LitMod3D uses a combined petrological (compositional), rheological (isostatic) and thermal (1315 °C isotherm) definition of the lithosphere-asthenosphere boundary (LAB).

Generally, the LAB is defined as the boundary between the rheologically strong lithospheric mantle and the rheologically weak asthenospheric upper mantle, where partial melting occurs (Artemieva, 2009, and references therein). Laboratory experiments indicate a sharp change in rheology and elastic properties of olivine-rich rocks at temperatures between 85% and 100% of the solidus temperature (Sato and Sacks, 1989;

Sato et al., 1989) and thus connect the rheological definition with a thermal boundary in the range of 1250–1350 °C. Different geophysical methods can be used to detect the LAB, depending on the according definition, which with their pitfalls are discussed in detail in Artemieva (2009) and Eaton et al. (2009). For example, from seismic methods the LAB can be defined as a change in anisotropy or as the boundary between a (*S* wave) high-velocity lid and low velocities in the asthenosphere. For GIA modeling, the transition from purely elastic to viscoelastic behavior on glacial time scales determines the bottom of the lithosphere (Nield et al., 2018, and references therein), which does not necessarily coincide with any of the previously mentioned LAB definitions (Artemieva, 2009). This transition is governed by viscosity, which is the crucial parameter for GIA studies (Paulson et al., 2005; Wu, 2005) and can be derived through conversion of temperatures by using power law rheology (Nield et al., 2018).

In the following, we provide a short overview of the methodology of LitMod3D (for more details, the reader is referred to Fullea et al., 2009). The specific values of the modeling parameters such as densities will be presented in the subsequent section.

The model space is discretized into a regular Cartesian grid, and cells are assigned to specific layers. Thus, a geometry and geophysical parameters need to be predefined. In the simplest case, a model may consist of a crust, a lithospheric mantle, and a sublithospheric mantle layer. Each cell inherits the layer-specific geophysical parameters: bulk density, compressibility and thermal expansion coefficient, thermal conductivity, and radiogenic heat production. For computing heat transfer, LitMod3D assumes a conduction-dominated lithosphere, where the thermal structure is calculated with the common steady-state (time-invariant) heat equation. While the thermal conductivity of the crust is constant, the thermal conductivity in the mantle follows the temperature- and pressure-dependent model of Hofmeister (1999). The upper and lower thermal boundary conditions of the conduction-dominated region are defined by a constant surface temperature and a constant temperature at the LAB, respectively. Below the LAB, a buffer layer is modeled to represent both conduction and convection in a rheologically active layer between the lithosphere and the sublithospheric mantle down to a depth where the temperature reaches 1400 °C. Further down, convectional heat transfer is simulated by an adiabatic gradient between the temperature at the bottom of the model at 400 km and 1400 °C isotherm. The bottom temperature is set to 1500 °C, which is consistent with high-pressure and high-temperature experiments (Fullea et al., 2009, and references therein).

The *in situ* density in crustal layers follows the formula for thermal expansion and compression:

$$\rho\left(T,P\right)=\rho_0-\rho_0\alpha\left(T-T_0\right)+\rho_0\beta\left(P-P_0\right), \tag{3.3}$$

in which ρ_0 is the bulk density, α the thermal expansion coefficient, and β the compressibility. In subcrustal layers, densities are calculated with the thermodynamic modeling software Perple_X (Connolly, 2005) for given geochemical mantle compositions in the CaO, FeO, MgO, Al_2O_3, and SiO_2 scheme under mantle pressure and temperature conditions. Since more than 98% of the mantle is made up of these oxides (e.g. McDonough and Sun, 1995), they are considered to be a good basis for modeling mantle phase equilibria (Afonso et al., 2008). By minimization of the Gibbs free energy, the stable mineral phases and the consequent bulk rock densities can be computed according to several thermodynamic databases, which are based on laboratory experiments. We use the formalism and database for peridotites from Stixrude and Lithgow-Bertelloni (2005).

For Airy-type local isostasy, the pressure corresponding to the overlying density column is calculated for every node at the bottom of the model space (compensation level). The resulting elevation due to buoyancy forces is obtained from comparison with a reference density column at a mid-oceanic ridge and can be used as a quantity to fit the model to the actual topography in the study area. The reference at the mid-oceanic ridge is chosen because average elevations, petrogenetic processes, and lithospheric structures are better known there than in other tectonic settings (Afonso et al., 2008). Dynamic loads associated with sublithospheric mantle flows are neglected. Likewise, the error for Airy-type isostasy emerging from the planar approximation of the Earth is negligibly small due to the relatively thin lithosphere compared to the Earth's radius (Hemingway and Matsuyama, 2017). To take into account the rigidity of the lithosphere, regional (flexural) isostasy is modeled on the basis of the local isostasy, the pressure at the compensation level, and the assumed elastic thickness (T_e) of the lithosphere with the software TISC (Garcia-Castellanos, 2002). For our modeling we choose a value of $T_e = 30$ km.

Although LitMod3D is capable of calculating gravity gradients, this is still done in a Cartesian coordinate system. To account for the large extension of Antarctica, a spherical geometry should be used to avoid biased results. We thus use the software Tesseroids (Uieda et al., 2011), which can compute the gravitational potential, the gravity,

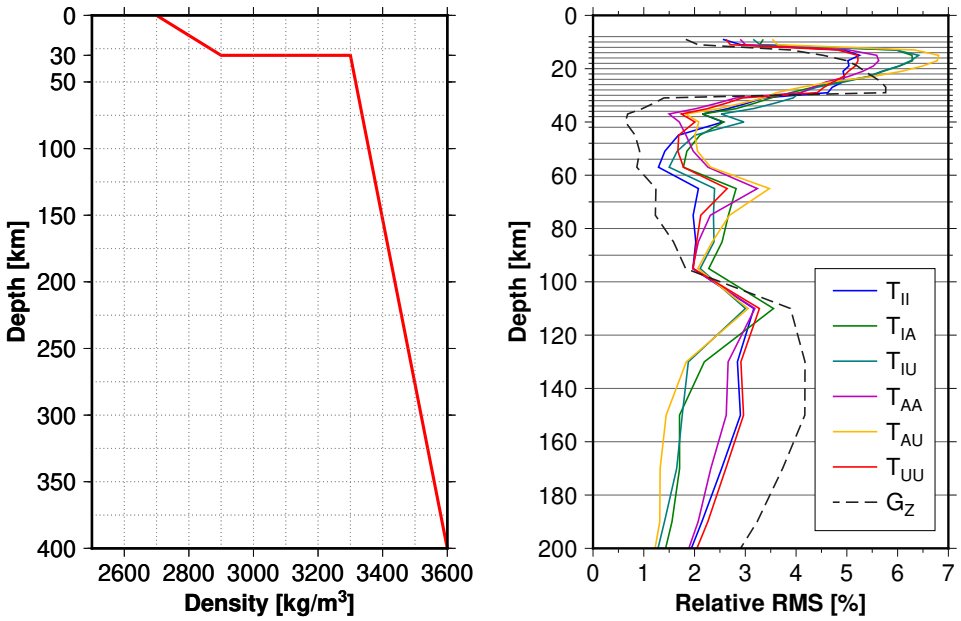

Figure 3.3.: (left) A step-wise linear reference density model is used to compute relative density anomalies and gravity gradient anomalies. (right) Relative depth sensitivity of vertical gravity G_Z and gravity gradients for the final model. Horizontal lines mark the thickness of the contributing depth interval. The gradients generally show high sensitivity at depths above 100 km. T_{IA}, T_{IU}, and T_{AU} obtain their largest contribution from the uppermost 25 km, reflecting the density variation across continent-ocean transitions. Compare Figure A.11 for absolute root-mean-square (RMS) values.

and the gravity gradient effect caused by tesseroids with certain densities. We transform the lithospheric density model from LitMod3D into a spherical tesseroid model. An equiangular discretization in polar regions, however, would lead to very small tesseroids near the pole and bigger tesseroids at higher latitudes. A discretization into metrically equal sized tesseroids is a better choice, considering both numerical precision and computational effort. To avoid edge effects, we extend the model up to latitude 30° S. From the Cartesian LitMod3D model, an inner high-resolution (~25-km edge length) model is created up to a latitude of 60° S. Beyond that, coarser tesseroids (0.5°) are built. If a tesseroid of the extension model lies outside the original LitMod3D model space, the density of the particular depth layer is extrapolated and assigned to the tesseroid. A piece-wise linear reference model (Figure 3.3) with density increasing with pressure in the crust (above 30 km) and the mantle (below 30 km), is subtracted from the modeled *in situ* (absolute) densities.

3.3.2. GIA Modeling

For the GIA response a model is used that is based on the finite element software ABAQUS™, which computes the deformation for certain surface loads. Iterative calculations are required to account for changing non-eustatic sea level and the gravitational potential, which result in a new load to be applied at boundaries (Wu, 2004). Density and rigidity are derived from volume averaging of Preliminary Reference Earth Model (PREM) (Dziewonski and Anderson, 1981). Three-dimensional density structure, mainly the difference between EANT and WANT, could influence results, but our method requires 1-D density. Earlier work that included variation of 1-D density profile suggests limited effects for spatial wavelengths above 700 km (Vermeersen and Sabadini, 1997). Three-dimensional variation in elastic parameters was found to introduce small effects on elastic response (Mitrovica et al., 2011) and is therefore not included. The finite element model uses a stress-strain-rate relation for composite rheology (van der Wal et al., 2013, 2010). The composite rheology is based on experimental flow laws for olivine of Hirth and Kohlstedt (2003), which are assumed to be valid for the upper 400 km where olivine is the dominant mineral. The lithosphere our GIA model is implicitly defined in the model as that part of the top of the Earth model that does not deform viscously in the time scale of glacial loading. Barnhoorn et al. (2011a) Barnhoorn et al. (2011) derived that this cutoff viscosity of 10^{25} Pa·s, above which no viscous deformation takes place, would be detectable in GIA measurements.

Viscosity, η_{eff}, is computed as in van der Wal et al. (2015):

$$\eta_{\text{eff}} = \frac{1}{3B_{\text{diff}} + 3B_{\text{disl}} q^{n-1}} \tag{3.4}$$

with q as the von Mises stress, n as the stress exponent (set to 3.5), and B_{diff} and B_{disl} contain all rheological parameters from the creep law for diffusion and dislocation creep in olivine

$$B = A d^{-p} f H_2O^r e^{\alpha\varphi} e^{-\frac{E+PV}{RT}}, \tag{3.5}$$

in which A and α are constants, d is the grain size, fH_2O is water content, φ is melt fraction, E is activation energy, P is pressure, V is activation volume, R is the gas constant, T is absolute temperature, p is the grain size exponent, and r is the water fugacity exponent, respectively. Except for grain size and water content, all values

are taken from Hirth and Kohlstedt (2003, Table 1). Pressure is calculated as a function of depth and density as obtained from PREM; temperature is taken from the LitMod3D model interpolated on the $2° \times 2°$ grid of the finite element model using triangular based linear interpolation. The viscosity in Equation 3.4 is stress dependent. That means that there is a weak dependence on the ice load, for which we use the W12 model (Whitehouse et al., 2012). O'Donnell et al. (2017) suggested GIA and sublithospheric tectonic stress levels to be of the same order of magnitude, which means that the viscosity will also depend on the tectonic stress. We neglect the influence of background stress here, as accurate predictions requires the stress tensor from both processes to be known.

B_{diff} below 400 km is set to $1.1 \cdot 10^{-21}$ $\text{Pa}^{-1}\cdot\text{s}^{-1}$ (corresponding to a viscosity of $1.1 \cdot 10^{21}$ Pa·s). Outside the LitMod3D space, the top 100 km is taken to be elastic close to the value obtained in global GIA model (Peltier, 2004). Below 100 km, a diffusion creep parameter is used that corresponds to a viscosity of $1 \cdot 10^{21}$ Pa·s. To reduce edge effects, creep parameters across the boundary are smoothed by applying a moving average to the log base 10 values of the creep parameters in a range of 8° before and after the boundary.

Applying an olivine flow law to derive viscosity introduces many uncertainties. Here we consider water content and grain size as unknown parameters as they have a large effect on viscosity for values that are still within their uncertainty bounds. In principle, those quantities can be measured in xenoliths but they do not provide a single, typical grain size. Furthermore, it is not certain how well the grain size and water content of the surfaced rocks represent conditions at depth. Also, the scarcity of xenolith samples in Antarctica makes it difficult to use them as constraints for flow law parameters. Hence, we opt to use values for grain size and water content that result in acceptable viscosities as determined from their good fit to GIA observations in other regions (van der Wal et al., 2013). Uncertainty in other parameters is absorbed by the grain size and water content. We do not include the influence of partial melt as O'Donnell et al. (2017). Viscosity and present-day uplift rates are shown for our temperature model for dry rheology and 4-mm grain size (4d, the preferred model in van der Wal et al., 2015), while uplift rates from wet rheology (1000-ppm water content) and varying grain sizes are also investigated. It is important to note the Antarctic-wide loading model that we use here does not include recent ice load changes, which are expected to dominate present-day uplift rates in some regions in Antarctica (e.g. Barletta et al., 2018; Nield et al., 2014).

3.4. Model Setup

To cover the whole Antarctic continent at a reasonable resolution, our model extends over 6620 km $\times$ 6620 km with a lateral resolution of 50 km. Vertically, the model extends down to 400 km, and a smaller vertical discretization of 2 km is chosen for reasons of numerical precision in computing the heat transfer. An initial structure is needed to start the model, ideally solely based on seismic estimates to be independent from our gravity gradient modeling. We use the continental-scale crustal thickness model AN1-CRUST (An et al., 2015b) since it is not a compilation of different regional studies but derived from Rayleigh wave analyses, constrained by Moho depth estimates from studies using receiver function techniques. The crustal thickness values from AN1-CRUST are the distance from the solid surface to the Moho, so we subtracted the surface elevation data from Bedmap2 in order to obtain the Moho depth with respect to the WGS84 reference ellipsoid and refer to the product as AN1-Moho (Figure 3.4). A continent-wide estimate of the lithospheric thickness is provided by the model AN1-LAB (Figure 3.4) from An et al. (2015a). The authors inverted temperatures from mantle *S* wave velocities (An et al., 2015b) and defined the LAB as the shallowest position with a temperature crossing the 1330 °C adiabat. As described in section 1, the inferred mantle temperatures of this model may be overestimated due to omission of potential presence of melt or water. However, we regard the AN1-LAB to be a good initial geometry for our modeling. The An et al. (2015a) temperature model will be used for comparison with our final lithospheric model.

Given the lack of knowledge about characteristics of the lithosphere for large parts of Antarctica, particularly the interior of EANT, we take general (global) geophysical and petrophysical properties for crustal and lithospheric mantle rock parameters, but we distinguish between different domains vertically and horizontally (Table 3.1). Both the crust and the lithospheric mantle in our models are divided into an oceanic and a continental part. Since the actual ocean-continent transition at Antarctica's margins is still ill constrained in some regions, we use bathymetric data from the Bedmap2 and the ETOPO1 data sets to determine the continental shelf line (taken at 2000-m water depth) and take this as a proxy for the boundary of the continental lithosphere. We divide the continental crust into three layers of equal thickness (upper, middle, and lower crust). In this way we are able to model the thermal field more realistically by introducing differentiated radiogenic heat production rates and thermal conductivity, and we can vary the vertical density distribution within the crust.

Type	Heat production ($\mu W/m^3$)	Thermal conductivity (W/mK)	Density (kg/m^3)	Thermal expansion K^{-1}	Compressibility GPa^{-1}
Sediments	0.5	1.85	2300	1E–5	8E–10
Upper crust	1.0	2.35	2670	1E–6	1E–10
Middle crust	0.4	2.25	2670	1E–6	1E–10
Lower crust	0.4	2.0	2800	1E–6	8E–11
Oceanic crust	0.1	3.0	2950	0	0
Mantle layers	0.01	5.3	—	—	—

Table 3.1.: Petrological parameters of crustal layers in the final model (Model 3). The *in situ* density is computed as a function of thermal expansion and compression according to temperature and pressure conditions. The thermal conductivity within the mantle follows the equations from Hofmeister (1999). The denoted value represents thermal conductivity at standard temperature-pressure conditions (Fullea et al., 2009).

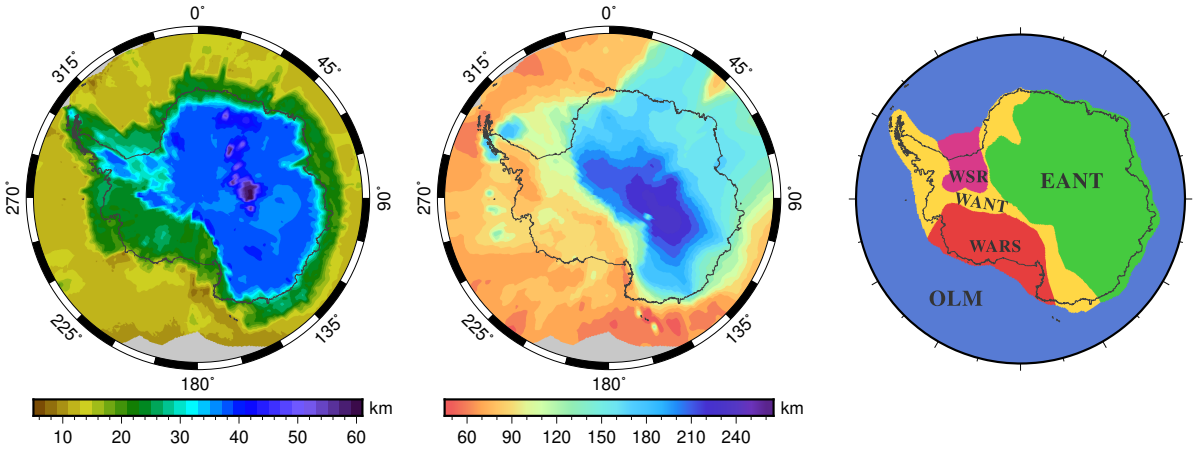

Figure 3.4.: Initial model geometry for Moho and LAB depth is taken from seismological estimates: AN1-Moho (left, An et al., 2015b), AN1-LAB (center, An et al., 2015a). The right map shows the subdivision of lithospheric mantle domains in the model based on previous studies on tectonic provinces of Antarctica. EANT=East Antarctica, OLM=Oceanic lithospheric mantle, WANT=West Antarctica, WARS=West Antarctic Rift System, WSR=Weddell Sea Rift; LAB=lithosphere-asthenosphere boundary.

wt%	PUM[a]	Lherzolite[b]	Harzburgite[c]	Phanerozoic[d]	Proterozoic[d]	Archaean[d]
SiO_2	45.45	45.08	43.48	44.99	45.19	46.08
MgO	38.18	42.70	46.26	40.24	43.16	45.88
Al_2O_3	4.55	2.42	1.96	3.54	1.93	1.00
FeO	8.18	8.44	7.80	8.09	8.00	6.45
CaO	3.64	1.36	0.50	3.13	1.72	0.59
Mg#	89.27	90.02	91.36	89.87	90.58	92.69

Table 3.2.: Oxide composition of lithospheric mantle peridotites used for the modeling. PUM=primitive upper mantle. [a]McDonough and Sun (1995). [b]Maaløe and Aoki (1977). [c]Irifune and Ringwood (1987). [d]Fullea et al. (2009) and references therein.

We use the same values as An et al. (2015a) for the thermal parameters, such that our modeled heat flow can be compared to their estimates.

To define different lithospheric mantle domains, we followed overviews of the Antarctic tectonic provinces (e.g. Goodge and Fanning, 2016; Harley et al., 2013; Boger, 2011), which rely on petrological evidence. The subcontinental lithospheric mantle is divided into three major domains (Figure 3.4): EANT, WANT, and the two major rift systems: the WARS (Bingham et al., 2012) and the Weddell Sea Rift (Jordan

et al., 2017b). We use representative lithospheric mantle compositions of Phanerozoic age for WANT and Proterozoic age for EANT (Table 3.2). Peridotitic xenolith samples from the WARS indicate a very heterogeneous lithospheric mantle structure (e.g. Armienti and Perinelli, 2010; Storti et al., 2008; Wörner, 1999), partly characterized by metasomatic processes and re-enrichment of depleted lithospheric mantle. Since our model is not supposed to account for such localized variations, we assume a primitive upper mantle composition (McDonough and Sun, 1995) for the rift systems. Parts of EANT are assumed older than Proterozoic (Goodge and Fanning, 2016; Elliot et al., 2015; Ménot et al., 2007). For these regions, we implement an Archaean lithospheric mantle composition in some of our models as explained later on. Yet since such a depleted composition leads to very low densities, we implement it only in the upper lithosphere, accounting also for potential refertilization by postdepletion metasomatism of the lower lithosphere (e.g. Beyer et al., 2006). In oceanic areas, the lithospheric mantle is modeled in two layers in order to represent the vertically varying chemical composition and density due to differences in the degree of melt depletion in the mantle material generated at the mid-ocean ridge (e.g. Afonso et al., 2007; Ji and Zhao, 1994). The lower layer of oceanic lithospheric mantle makes up two thirds of the total lithospheric mantle thickness in our model and has a lherzolithic composition, while the upper layer (one third of the total thickness) is modeled as harzburgite.

3.5. Results and Discussion

An iterative process was adopted to fit the model outputs to the observational data sets, that is, the rock-equivalent topography and the gravity gradient anomaly field at satellite height. The simple starting model with the initial geometry based on seismological data turns out to be far from isostatic equilibrium and does not satisfy the gravity gradient observations. Therefore, we proceed from this simple starting model and refine it in three subsequent stages:

1. Model 1 keeps the petrological parameters and the lithospheric domains from the initial model. The depths of the Moho and LAB interfaces are iteratively changed in the model in order to fit the isostatic elevation to the observed rock-equivalent topography. For this purpose, in each iteration step the current elevation misfit between the model and the data is multiplied with a factor that relates the topographic load with the mass deficit or surplus, respectively, at the

interface through simple Airy isostasy. A detailed description of the method is given in section A.2. The resulting model is not a unique solution because, theoretically, isostatic equilibrium can be achieved with a variety of pairs of factors for adjusting the Moho and the LAB depth. However, the internal modeling processes, which determine the density in each cell of the model, significantly narrow the set of solutions (e.g. Afonso et al., 2013). After achieving isostatic equilibrium in Model 1 in this way, high residuals of more than ± 1 E are still present in the gravity gradients in some areas (Figure A.8), which is ~25% of the amplitude of the topography-reduced input data. As an explanation, this misfit could be related to an improper vertical density structure of the model's lithosphere. For isostasy, only the mass integral is relevant. The gravity gradient components, on the other hand, have different depth sensitivities.

2. In Model 2, we account for these gravity gradient residuals by refining crustal and lithospheric domains while still maintaining isostatic equilibrium. Additional blocks of Archaean mantle lithosphere are introduced and the density parameters of the overlying crust are changed in regions with large misfits (Figure A.9). The vertical density distribution is modified in such a way that the upper lithospheric mantle is less dense (depleted Archaean composition), whereas the crustal density is increased. Simultaneously, the Moho boundary and the LAB are shifted again to achieve isostatic equilibrium with the result that the crust is thinned and the lithospheric mantle is thickened, and thus, crustal material is replaced by denser mantle peridotite. Moreover, by shifting the isotherm that defines the LAB to greater depths, the middle to lower lithospheric mantle becomes denser due to temperature decrease. As a result, the gravity gradient response of Model 2 is improved by a few tenths of eötvös in the respective regions. It was, however, not possible to fit both the isostatic equilibrium and the gravity gradient field simultaneously.

3. Model 3 builds upon Model 2, but the previous constraint of isostatic balance of the Antarctic continent is discarded. Instead, the depth of the Moho discontinuity and LAB is adjusted based on the gravity gradient residual with accordingly different factors but in principle the same procedure as described for the isostatic fitting. As a result, the residual of the gravity gradients is generally less than ± 0.2 E (Figure 3.5), thus less than 5% of the topography-reduced signal. In turn,

the root-mean-square (RMS) misfit between modeled and observed topography is 389 m (Figure 3.5). The patterns of the residual topography correlate with the gravity gradient (T_{UU}) residuals in Model 2 since the mass change in the subsurface is reflected by an increased or decreased isostatic elevation, respectively. These adjustments have implications for the isostatic state of different parts of Antarctica. In the following subsections, we will discuss and interpret the particular characteristics of the models in terms of crustal and lithospheric thickness, density, and temperature.

3.5.1. Topography Misfit in Gravity Gradient Fitted Model

By establishing isostatic equilibrium, a first-order fit of the gravity and gravity gradient field can usually be achieved (e.g. Braitenberg et al., 1997). This approach indeed reduces the gradient misfit of Model 1 significantly compared to the initial model, which was not in isostatic balance. It is, however, uncertain to what extent the Antarctic continent actually is in isostatic equilibrium. If sublithospheric forces generate a non-isostatic component in the present topography, fitting the observed gravity gradient field is a better option than fitting the isostatic elevation, because the gradients are most affected by near-surface density variations. Furthermore, given the high accuracy and the homogeneous covering of the gravity gradient data over Antarctica, we consider Model 3 as our preferred model for a representation of the continent's lithospheric density structure. However, because the condition of perfect isostatic equilibrium is released, it shows a mismatch with the actual (rock-equivalent) topography (Figure 3.5). While no clear contrast is apparent between WANT and EANT in the residual map, Wilkes Land shows a distinctly different (negative) signature from the rest of EANT. Yet some parts of Wilkes Land still show positive residuals, specifically where the Archaean to Mesoproterozoic Terre Adélie Craton is located (e.g. Lamarque et al., 2015; Ménot et al., 2007) and where the inferred Paleoproterozoic Beardmore Microcontinent (e.g. Boger, 2011; Borg et al., 1990) is thought to underlie parts of the Wilkes Subglacial Basin (e.g. Ferraccioli et al., 2009a; Ferraccioli and Bozzo, 2003) region (Figure 3.1).

In summary, these topography residuals are not explained by the gravity gradient signal. Their large-scale variations may be induced by sublithospheric forces like mantle upwellings or downwellings, which provide dynamic support of the topography. Short-wavelength residuals could originate from imperfect topographic or ice correc-

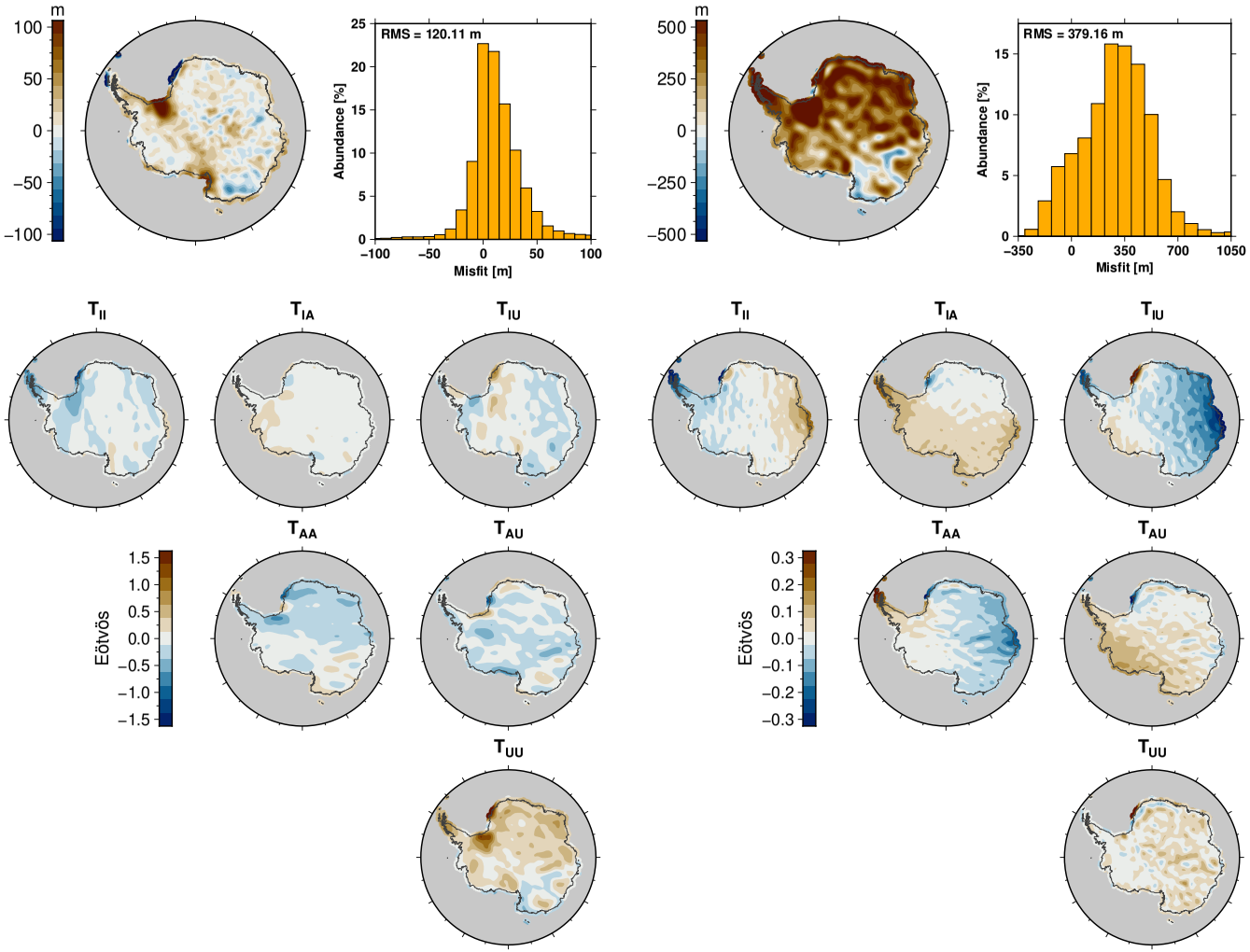

Figure 3.5.: Residual analysis Model 2 (left) and Model 3 (right). (top) Topography misfit map and histogram. (bottom) Misfit of gravity gradient signal. Note the different value ranges. The gravity gradient misfit is reduced significantly from Model 2 ($\pm$1 E) to Model 3 ($\pm$0.2 E), though at the expense of the fit of perfectly isostatically compensated topography. The difference in elevation of ~250 m, mostly emerging in East Antarctica, may point to an imperfect topographic gravity correction model, flexural compensation, or dynamic forces that support the topography.

tion models onshore or sediment models in offshore areas. It is also possible that they represent topographic masses that are not in local isostatic balance but compensated regionally due to lithospheric flexure (e.g. Paxman et al., 2019). However, the RMS misfit of ~380 m is still small compared to the corresponding crustal thickness variation that would be needed to compensate such a topographic load. Assuming a rock density for the topography of 2670 kg/m^3 and a density contrast at the Moho of 400 kg/m^3, a 2.5-km-thicker crust would compensate 380 m of topography. This is below the uncertainty of most seismic-inferred Moho depth estimates even in well-studied areas.

3.5.2. Density Structure

A main advantage of using the full gravity gradient tensor in lithospheric modeling is the potentially different depth sensitivity of the individual components. The theoretical sensitivity kernels for the gravity gradients show a large response for near-surface mass anomalies (Martinec, 2014). However, the actual contribution of each depth interval depends on the location of the sources in the respective study area. An appropriate way to quantify this contribution is to compute the relative RMS of the signal of density variations with respect to the reference model (Bouman et al., 2016). For every single component of the gravity gradient tensor—and the vertical gravity G_Z, respectively—the contribution of a particular depth interval is given in percentage of the total RMS integral over the depth. Figure 3.3 (right) shows the relative RMS signal contribution from different depth ranges computed for our lithospheric Model 3. (For absolute values see Figure A.11.) For the vertical gravity and all gradient components, the strongest signal originates from a depth range of 10 to 25 km, which reflects the density variations at the continent-ocean boundaries. Horizontal and mixed components are more sensitive to signals at this depth than the vertical gradient T_{UU} and the vertical gravity G_Z. From 25- to 40-km depth, the contrast between EANT and WANT affects the gradients more than the vertical gravity, resulting in a smoother decrease of the RMS with depth. In particular, the horizontal component T_{IA}, which is commonly considered to be most sensitive to very shallow structures, is still remarkably strong at this depth. Clearly, this reflects the sharp transition at roughly 45° W/135° E between WANT and EANT. Furthermore, a noticeable divergence of the T_{AU} and T_{AA} components is present at ~60-km depth. This means that a marked density variation exists with an orientation perpendicular to the 0° meridian (point-

ing toward the Atlantic), which is the Pacific-Antarctic Ridge north of the Ross Sea region. The density of the upper mantle is decreased to 3200 kg/m^3 here in order to fit the bathymetry, whereas other regions in the model show 3300 kg/m^3 and more in ~60-km depth. In summary, for almost every single layer above 100-km depth, the relative RMS contribution is higher in the gravity gradients than in the vertical gravity, even below the Moho.

The modeled densities of the upper mantle in our Model 3 are shown in Figure 3.6. At depths of 50 to 80 km the topography of the LAB is dominating the patterns in WANT with rather low densities in the coastal areas. In EANT the deep crustal root of the Gamburtsev Subglacial Mountains (GSM) stands out in the 50-km depth slice, whereas at 80-km lower density is present in areas where our model features Archaean lithospheric mantle composition. Down to 150 km, the mantle density is lower beneath WANT due to the higher temperature compared to cratonic EANT (Figure 3.6e). However, this relation is reversed below 150 km. At this depth, relatively low density values are present beneath EANT (Figure 3.6f), and the deep lithospheric mantle of EANT is notably less dense than the sublithospheric mantle of WANT, particularly at its edges where it is hotter than in the interior. A cross section through the model is shown in Figure 3.6a that spans from the West Antarctic coast of Marie Byrd Land (MBL) across the WARS, the TAM, the GSM, and the Lambert Graben to the Indian Ocean coast, thus covering key elements of Antarctica's lithospheric structure over a distance of 5500 km. It reveals another interesting feature: At the depth of the shallow LAB beneath WANT almost no density contrast is present between lithosphere and asthenosphere since the lithospheric mantle is relatively fertile, hot, and at low pressure. On the other hand, the density contrast at the deep lithospheric base of EANT adds up to several tens of kilograms per cubic meter and thus contributes to the lithosphere's buoyancy and the gravitational field anomalies. However, we note that our model does not include potential density variations in the asthenosphere due to temperature anomalies, as one would expect in case of a (WARS) mantle plume (e.g. Seroussi et al., 2017).

Another approach to investigate the lithospheric structure of Antarctica in terms of density, along with temperature and composition, has been recently presented by Haeger et al. (2019). Instead of predefining the lithospheric mantle composition, that study inverts for composition, density, and temperature while different seismological *S* wave tomography models are used to iteratively reconcile the estimates in a thermodynamically consistent way. The main difference with our strategy is, however, that

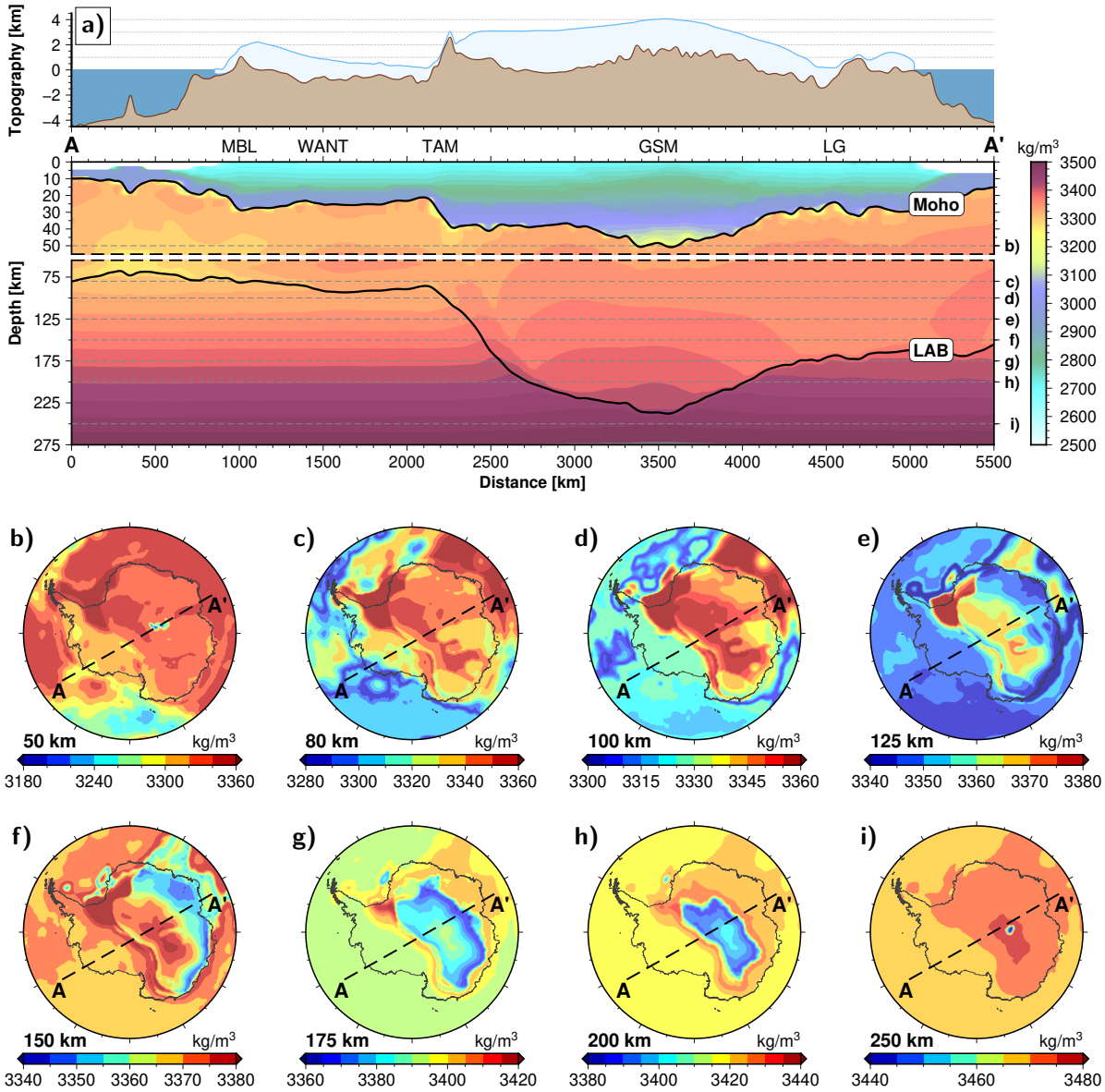

Figure 3.6.: (a) Cross section through ice, topography, crust, and mantle of our Model 3. The profile is shown in the slices below. High crustal densities are present beneath the GSM. The mantle cross section illustrates the different density contrasts at the lithosphere-asthenosphere boundary beneath WANT and EANT, respectively. MBL=Marie Byrd Land, WANT=West Antarctica, TAM=Transantarctic Mountains, GSM=Gamburtsev Subglacial Mountains, LG=Lambert Graben. Dashed horizontal lines indicate depths of mantle density slices: (b) 50, (c) 80, (d) 100, (e) 125, (f) 125, (g) 175, (h) 200, and (i) 250 km.

Haeger et al. (2019) base their analysis on a predefined Moho depth, whereas it is a model result in our study. Vice versa, we predefine lithospheric mantle compositions in our modeling, while Haeger et al. (2019) invert for these. The degree of depletion of the lithospheric mantle material is strongly dependent on the selection of the seismic tomography model in the inversion of Haeger et al. (2019), demonstrating the need for more seismological surveys for Antarctica.

3.5.3. Crustal Thickness

The depths of Moho and LAB result from fitting the elevation (Models 1 and 2) and the gravity gradients (Model 3), respectively, starting from the initial model based on the seismologically derived geometry from An et al. (2015b,a). We do not fit our model to seismic data but compare our results with seismic-inferred Moho depth estimates. A considerable number of local seismic Moho depth estimates exist, even though large gaps in the coverage of the Antarctic continent are still present.

Recent continental-scale Moho depth models (e.g. Haeger et al., 2019; An et al., 2015b; Baranov and Morelli, 2013) made use of the local Moho studies by application of different techniques to infer the crustal thickness in poorly covered areas. Several other Moho depth models exist for Antarctica, which are, however, less suited for the evaluation of our model since they involve the inversion of gravity data (e.g. Baranov et al., 2018; O'Donnell and Nyblade, 2014; Block et al., 2009) or only provide estimates in a limited region (e.g. White-Gaynor et al., 2019; Shen et al., 2018; Chaput et al., 2014). In comparison, some of these models show large discrepancies of more than 10 km in large areas of Antarctica (see Pappa et al., 2019a, for detailed discussion).

We evaluate the Moho depth of our models at the same seismic stations that have been used by An et al. (2015b) and Baranov and Morelli (2013). Figure 3.7 shows the Moho depth of Model 3 together with the mismatch to the seismic estimates indicated by colored circles. (For a mismatch histogram see Figure A.10.) Parameter and compositional changes from Model 1 to Models 2 and 3 improved the fit in Moho depth for WANT and TAM significantly owing to higher densities in the middle and lower crust. The crustal root beneath areas with high topography is therefore less pronounced. The changes of Moho depth related to the release from isostatic equilibrium from Model 2 to Model 3 are minor in WANT, but in EANT the crust of Model

3 is thinned compared to Model 2. Areas of relatively thick crust become more pronounced, for instance, in eastern DML, in Terre Adélie, and west of Lake Vostok.

The RMS misfit at the seismic depth points increased slightly from 6.1 km in Model 2 to 6.9 km in Model 3 (Figure A.10). It is difficult to quantify the uncertainty of our Moho depth model in relation to the seismic estimates since disagreements exist between studies even at the same locations (Pappa et al., 2019a). As a measure of discrepancy, one can calculate the deviation D of the RMS misfit M of our model (6.9 km) from the supposed uncertainty U of seismological methods of ~3 km (e.g. Hansen et al., 2009) by

$$D = \sqrt{M^2 - U^2}, \tag{3.6}$$

which gives 6.2 km. This is, however, a measure of deviation in terms of seismic Moho depth estimates, whereas the misfit of the gravity gradients and the topography must also be taken into account.

The Moho depth of our final Model 3 (Figure 3.7) exhibits detailed patterns in EANT, typical of gravity-based or Airy-isostatic models (e.g. Pappa et al., 2019a; O'Donnell and Nyblade, 2014; Block et al., 2009). Although the AN1-Moho model was used as starting value, distinct differences exist in our Moho depth. DML shows more variations and can be divided into three parts: (1) the northern mountain ranges with crustal roots that exhibits crustal thicknesses of ~40–45 km, (2) further south western DML with a rather thin crust of ~30 km, and (3) eastern DML as a block with markedly thicker crust of ~40 km. These values and the according subdivision are consistent with results from Riedel et al. (2013, 2012), who jointly interpreted aeromagnetic and aerogravity measurements with isostatic modeling of the region. Studies relying on gravity or a combination of both gravity and seismology also show thicker crust in eastern DML (Baranov et al., 2018; O'Donnell and Nyblade, 2014; Block et al., 2009), and this is also revealed by the Rayleigh wave-derived model from An et al. (2015b). However, in previous Moho depth compilations (Baranov and Morelli, 2013), based on regional surveys, the opposite was found with thicker crust in western DML. Yet as no seismic measurements for eastern DML were used in that compilation, the thickness values are interpolated in this area and thus subject to uncertainty.

In the AN1 model, a pronounced small patch of very thick crust beneath the Valkyrie Dome (also referred to as Dome Fuji) is present, but no such feature exists in our results. Instead, the crust there is thinner than at its surroundings.

Only scarce data exist for Enderby Land further east as well. While crustal thickness estimates exist for west Enderby Land (Yoshii et al., 2004; Miyamachi et al., 2003) and the Lambert Graben area (e.g. Feng et al., 2014; Reading, 2006), the interior structure of Enderby Land remains seismically underexplored. Satellite gravity inversions estimate the Moho depth in this region at ~40 km (Baranov et al., 2018; O'Donnell and Nyblade, 2014; Block et al., 2009) but can only give a rather blurred image due to the long-wavelength signal. As the gravity gradients enhance shorter wavelengths, which correspond to shallower structures, and our modeling process considers the principle of isostasy, we are able to infer more details in the crustal structure of Enderby Land. West of the Lambert Graben, the Moho is less than 40 km deep, reaching 30 km in central Enderby Land and near the coast. We can also see a clear boundary toward eastern DML along the ~30° N meridian. This is broadly consistent with the models from An et al. (2015b) and O'Donnell and Nyblade (2014).

The GSM, which are adjacent to the southern part of Enderby Land, have been subject to extensive investigations (e.g. An et al., 2016; Paxman et al., 2016; Heeszel et al., 2013; Lloyd et al., 2013; Ferraccioli et al., 2011; Hansen et al., 2010). Yet their formation remains unclear. One hypothesis that has been put forward to explain their uplift is Permian to Cretaceous rifting and strike-slip faulting followed by Cenozoic peak uplift due to fluvial and glacial erosion (Paxman et al., 2016; Rose et al., 2013; Ferraccioli et al., 2011) combined with remarkably low erosion rates (Cox et al., 2010). The remarkably thick crust that is still preserved beneath the GSM has been related to subduction and collision during the late stages of the Pan-African orogenic cycle (~550–500 Ma) by An et al. (2015b) or to much older Grenvillian-age accretion and possible collision of terranes against the composite Archean to Mesoproterozoic Mawson Craton by Ferraccioli et al. (2011). Estimates of crustal root depth values range from more than 60 km in seismic studies (An et al., 2016, 2015b) to ~50 km (O'Donnell and Nyblade, 2014; von Frese et al., 2009) or less (Block et al., 2009) in gravity-based models. Ferraccioli et al. (2011) have shown, based on gravity modeling, that the density contrast between the crustal root of the GSM and the underlying lithospheric upper mantle may be only about 55 kg/m^3. More generally, An et al. (2015b) conclude that the density contrast for whole EANT is small from comparison of their seismic crustal thickness estimates and an Airy-isostatic Moho depth model. In our model the Moho

shows a maximum depth of 52 km, and the root beneath the GSM is elongated in a south-north direction, rather than the more circular-shaped geometry imaged by An et al. (2015b). Between the GSM and the Vostok Highlands to the east, which again are underlain by a thick crust of more than 40 km, a clear lineament of thinner crust is apparent, consistent with seismological estimates (Ramirez et al., 2016) and the location of the proposed eastern branch of the East Antarctic Rift System (Ferraccioli et al., 2011).

Further east we can identify a prominent lineament in the region of the proposed Indo-Australo-Antarctic Suture (Aitken et al., 2014), where Indo-Antarctica and Australo-Antarctica may have collided either during the late Mesoproterozoic assembly of interior EANT or as late as the early Cambrian (Boger, 2011; Collins and Pisarevsky, 2005). However, the exact location of this inferred suture zone cannot precisely be determined from our model. The Terre Adélie Craton stands out as a block of ~40-km-thick crust, consistent with receiver function analyses (Lamarque et al., 2015). It is surrounded by the Aurora Subglacial Basin to the west, the Sabrina Subglacial Basin to the northwest, and the Wilkes Subglacial Basin to the west, which all are characterized by a rather shallow Moho at 30 km or shallower. This level of detail in crustal thickness variation has not been imaged in the region of Wilkes Land so far.

3.5.4. Lithospheric Thickness

As mentioned before, different definitions of the LAB exist corresponding to different geological understanding and geophysical methods. In our model the LAB is described by a thermal (1315 °C isotherm), rheological (base of rigid layer), and a compositional boundary. Basic assumptions in our modeling, such as composition and crustal rock parameters, imply some uncertainty due to the lack of reliable local constraints. As expressed previously, it should also be noted that the depths of the Moho and the LAB in our models are non-unique, which is always the case in models based on gravity, particularly because the density change at the LAB is generally small. Nevertheless, there are additional aspects that help to constrain the total lithospheric thickness in our model, which are the self-consistent computation of density due to pressure, temperature, and composition as well as the principle of isostasy. Some information about the robustness of the results can be given by the comparison with the seismologically derived and thus gravity-independent LAB depth model AN1-LAB (An et al., 2015a).

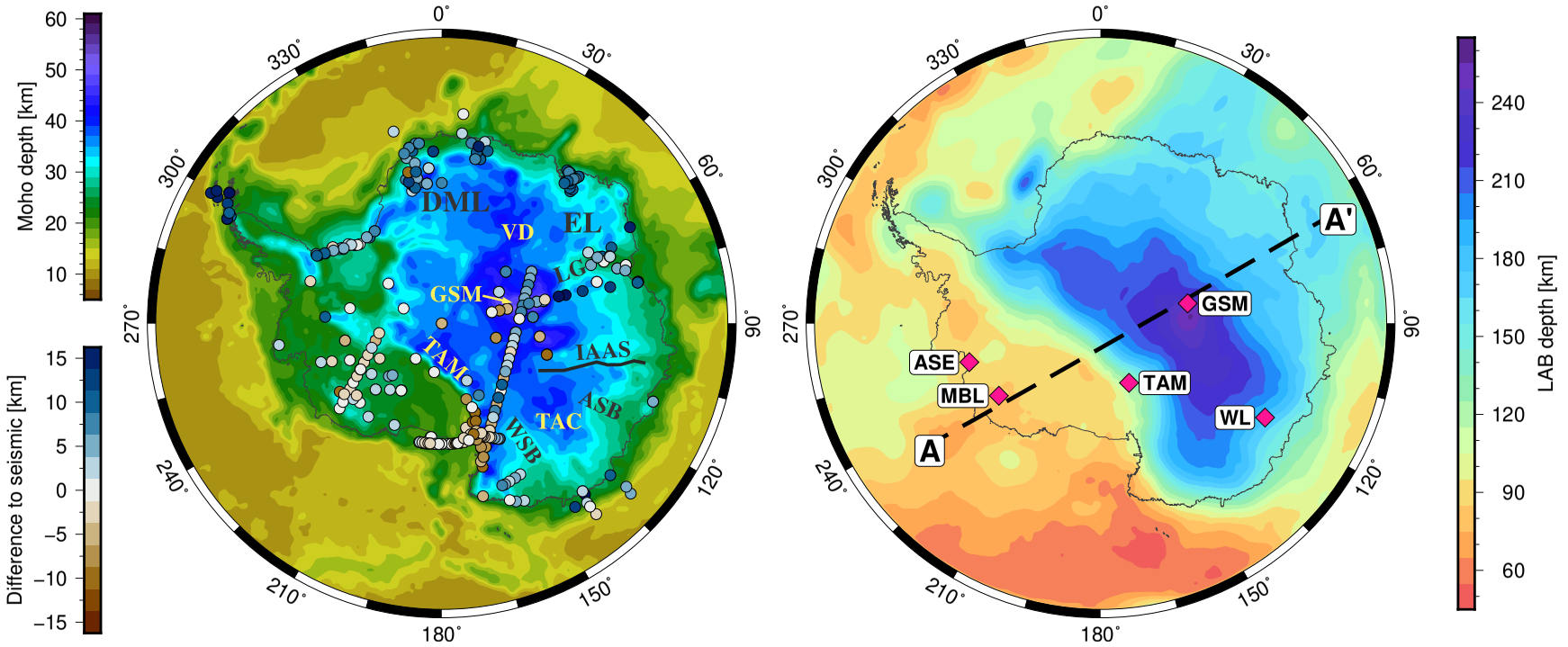

Figure 3.7.: (left) Moho depth of lithospheric model (Model 3). Colored circles show mismatch with respect to seismic estimates from other studies. ASB=Aurora Subglacial Basin, DML=Dronning Maud Land, EL=Enderby Land, GSM=Gamburtsev Subglacial Mountains, IAAS=Indo-Australo-Antarctic Suture, LG=Lambert Graben, TAC=Terre Adélie Craton, TAM=Transantarctic Mountains, VD=Valkyrie Dome, WSB=Wilkes Subglacial Basin. (right) Lithosphere-asthenosphere boundary depth of Model 3. Dashed line A–A′ corresponds to temperature cross sections in Figure 3.8. Pink-colored diamonds indicate locations of vertical temperature profiles in Figure 3.8.

An et al. (2015a) used a mixed LAB definition. They converted the *S* wave velocity model AN1-VS into temperatures and defined the LAB as 1330 °C isotherm. The authors state that the vertical resolution of their seismological LAB should be smaller than 20–50 km. This estimation, however, does not include the uncertainties in the conversion of velocities into temperature due to the choice of composition, grain size, and water content, which An et al. (2015a) assume to be ~150 °C. Since both our LAB and the AN1-LAB model are likewise defined as isotherms that only differ by 15 K, we can compare the depths of the LAB (Figures 3.4 and 3.7). Although we used the AN1-LAB as a starting geometry, the final LAB of our model results from a completely different methodology. They are markedly similar in most parts of Antarctica, and the differences are mainly within the range of uncertainty of different methods to assess the LAB depth. Similar to An et al. (2015a) and other seismological studies (e.g. Schaeffer and Lebedev, 2013; Ritzwoller et al., 2001), the lithospheric thickness of our final Model 3 shows a strong contrast between WANT where values less than 100 km are attained and EANT with more than 150 km. While the LAB topography in our model is rather smooth within both parts of the continent, the transition is very steep, spanning about 100-km depth difference over 250-km horizontal distance. In WANT few regions show a lithosphere thinner than 80 km, such as MBL, Ellsworth Land, and the Ross Sea front of the TAM. However, we see that a very deep LAB of ~180 km beneath the Weddell Sea emerged in our model, which is not shown by seismological models. This could be a consequence of an overestimated sediment thickness in this area due to the ambiguity of the depth to basement estimates from magnetic data, although notably the presence of cratonic lithosphere beneath the southern part of the Weddell Sea Rift has also been inferred from aeromagnetic studies (e.g. Jordan et al., 2017b, and references therein).

In EANT the cratonic nature is clearly reflected by a thick lithospheric root down to ~260-km depth beneath the GSM. Thickness values more than 200 km extend westward to the Pensacola Mountains and the Shackleton Range. To the east we still see 200-km LAB depth beneath George V Land and Wilkes Land. Notably, the lithosphere thins more rapidly toward the coast between the longitudes 20° W and 90° E, reaching 150 km beneath Enderby Land and 100 km beneath western DML, respectively.

A major difference between our model and the AN1-LAB is the lithospheric thickness in the GSM region. In contrast to the AN1-LAB, all our models result in a deeper LAB below the GSM in order to compensate the topographic load. The thickest lithosphere in the AN1 model with more than 230 km is located east of the GSM, whereas

in our models the deepest point lies beneath them at ~260 km. An et al. (2015b) regard the different locations of the thickest crust and the deepest LAB in their models to be evidence for a collision belt from the amalgamation of Gondwana during the Pan-African orogeny (~550–500 Ma). Low erosion rates for at least over 250 Myr (Cox et al., 2010) support the hypothesis that the high topography of the GSM might have been stable for 500 Myr. However, the whole mass column must have stayed close to isostatic equilibrium for this scenario. In our model a very thick (thus cold and dense) lithosphere is required to compensate the thick (less dense) crust beneath the GSM. If the crust is even thicker, as seen by An et al. (2015b), and the LAB less deep, isostatic equilibrium could only be achieved by higher densities within the lithosphere, meaning cold temperatures and possibly enriched mantle composition. Yet our model is even colder than AN1-T. It therefore seems unlikely that a thinner and warmer, thus more buoyant, lithosphere could have maintained isostatic equilibrium in the GSM region for several hundreds of million years.

3.5.5. Thermal Structure and GIA Response

Following our discussion on crustal and lithosphere thickness variations here, we infer the steady-state temperature distribution within the lithosphere and the sub-lithospheric mantle, which allows to estimate viscosity values for assessing GIA. It should, however, be kept in mind that our models presume that the lithosphere is in isostatic equilibrium and the steady-state temperature field does not include thermal anomalies. We discuss the thermal structure of our models at five selected points of interest (Figure 3.8): the Amundsen Sea Embayment (ASE), MBL, TAM, GSM, and Wilkes Land. Further comparison is made with the temperature model AN1-T from An et al. (2015a), which results from conversion of the *S* wave velocity model AN1-VS (An et al., 2015b) into temperatures. The authors point out that a homogeneous mantle composition and pressure dependency have been considered in the conversion method but not potential water content or partial melt. They take their estimated mantle temperatures to be the upper bound, and note that if the converted temperatures for the upper mantle seem unreasonably high, a possible explanation might be the existence of melt or fluid inclusions (An et al., 2015a). Indeed, the temperature of the AN1 model is slightly higher than ours, and some areas of increased temperature are not visible in our models.

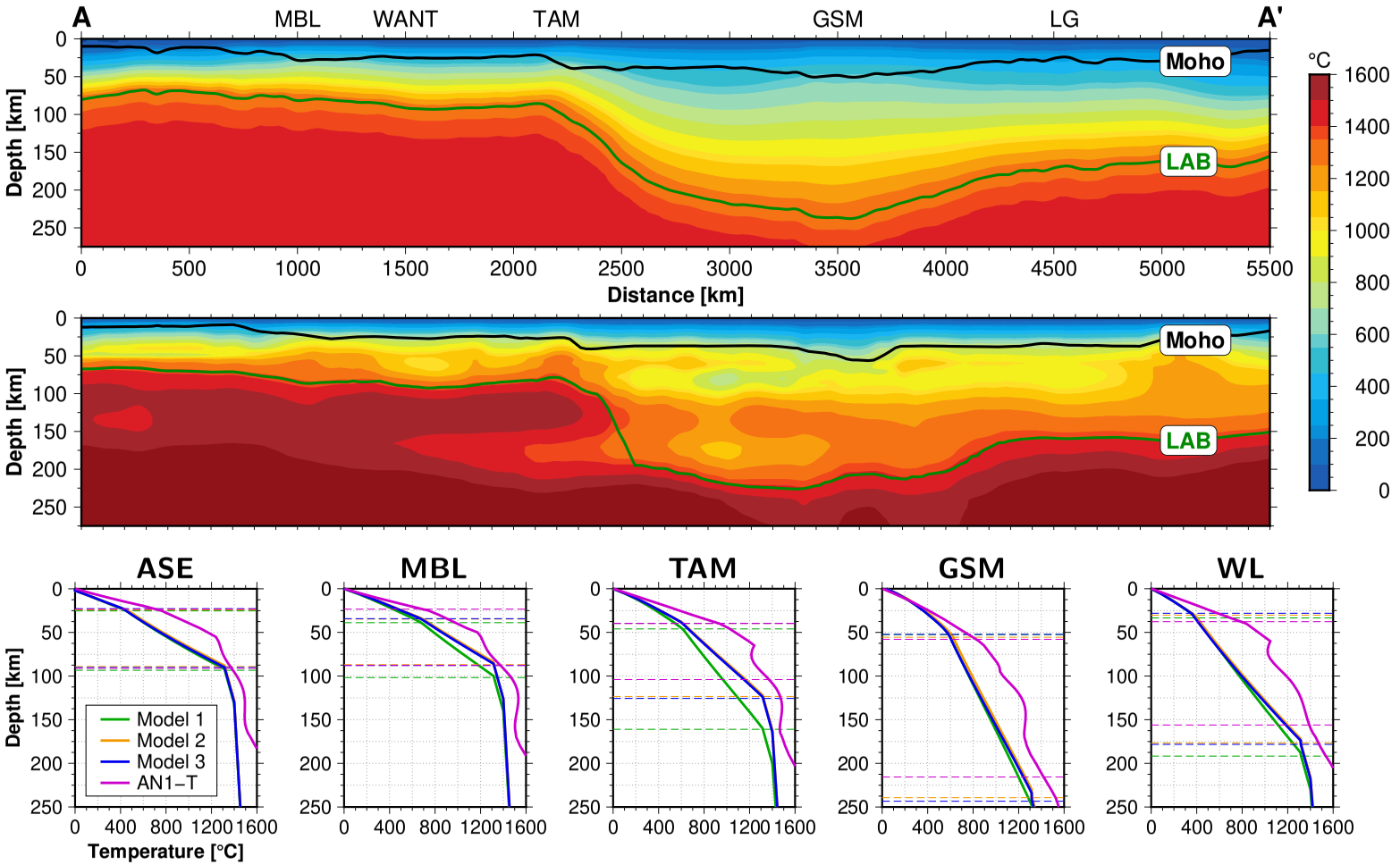

Figure 3.8.: Cross sections show temperature of Model 3 (top) and AN1-T (below) model from An et al. (2015a). (bottom) Vertical temperature profiles for selective locations demonstrate the generally higher temperature estimates from conversion from seismic velocity model (AN1-T). The locations of all profiles are indicated in Figure 3.7 (right). Horizontal dashed lines indicate depth of Moho and lithosphere-asthenosphere boundary, respectively. Note that the Models 1, 2, and 3 feature steady-state temperature fields and thus do not include thermal anomalies.

The cross section in Figure 3.8 demonstrates the striking temperature variations within the upper mantle between WANT to EANT in both Model 3 and AN1-T. At the transition from WANT to EANT, the AN1 model and our model show high temperatures at the steps of Moho boundary and LAB. Although our model only considers steady-state conditions and thus no thermal anomalies, the temperature at the Moho reaches almost 700 °C. Such values would be generally expected in orogenic belts (McKenzie et al., 2005), while the Moho temperature beneath cratonic shields is estimated to range from 300–500 °C (Archaean) to 450–650 °C (Paleoproterozoic; Artemieva, 2009). The generally higher temperatures of the AN1-T model compared to our models, particularly at the crust-mantle boundary, are also visible in the vertical temperature profiles (Figure 3.8), for example, at the TAM profile. Here, the AN1-T temperatures not only are ~400 K higher in the middle part of the mantle lithosphere (~70-km depth), but also our models differ from each other due to variations in lithospheric thickness. The lithosphere is much thinner (~125 km) in Models 2 and 3 than in Model 1 (>150 km). Consequently, the temperature is higher within the lithosphere in Models 2 and 3 and approximately 200 K higher at 125-km depth. Due to the associated density decrease in the mantle, this generally allows a thinner crust to be in isostatic balance and does not require a pronounced crustal root. A substantially hotter mantle could potentially increase this effect to the extent that a much thinner crust can overcompensate the topographic load. The cross section (Figure 3.8) also shows the lateral temperature variation of the uppermost lithospheric mantle between the TAM and the region beneath the GSM. Beneath the TAM, temperatures are high throughout the lithosphere due to the shallow LAB. The hinterland of the TAM toward the GSM features rather low temperatures below the relatively thin crust, whereas temperatures rise again beneath the GSM's crustal root. Here the thick crust provides additional heat from radiogenic decay, which is higher than in the mantle due to the increased abundance of uranium, thorium, and potassium. Such temperature variations affect the upper mantle seismic velocities, leading to velocity highs in regions of low temperature and a velocity low beneath the GSM. Such decreased velocities have been observed by Shen et al. (2018), who, however, hypothesize that they originate from compositional changes. Beneath the GSM, our models show ~600 °C at the Moho, whereas AN1-T suggests ~800 °C, which is much higher than generally expected for cratonic shields. Varying crustal density parameters in our Models 2 and 3 with respect to Model 1 in the GSM region apparently have no significant effect on the temperature. The same phenomenon occurs in the profile for Wilkes Land, where the

impact of the implementation of Archaean lithospheric mantle on the temperature is also minor, whereas it has a significant effect on the density.

In the ASE in WANT, our models show almost identical values, whereas the Moho in the AN1-T model is more than 200 K hotter and exceeds 700 °C. On the other hand, all models have similar temperatures at the lithospheric base. In the sublithospheric mantle the *S* wave inferred temperatures of the AN1 model show a pronounced temperature increase with respect to our models beneath the ASE. This is consistent with observations of the short-term interaction between solid Earth movement and ice mass changes in the ASE, which suggest very low upper mantle viscosities (Barletta et al., 2018). It is also consistent with seismic low-velocity zones in other studies (Shen et al., 2018; Hansen et al., 2014). Our models may underestimate the temperature because they represent a steady-state temperature distribution with a lithosphere in isostatic equilibrium, which might not be the case in the ASE. Similar limitations may apply for MBL. Here, the changes in crustal parameters from Model 1 to Model 2 led to a shallower Moho and LAB, resulting in higher temperatures within the lithosphere. As a consequence, lower densities and seismic velocities can be expected. However, seismological studies inferred significant mantle velocity reduction of 1–3% for *P* waves and 2–5% for *S* waves beneath MBL (White-Gaynor et al., 2019; Shen et al., 2018; Heeszel et al., 2016; Lloyd et al., 2015; Hansen et al., 2014), accompanied by Cenozoic volcanism (e.g. LeMasurier, 1990). Such velocity anomalies would correspond to a temperature increase of ~150 K (Lloyd et al., 2015). If, on the other hand, the upper mantle beneath MBL has an elevated water content compared to surrounding areas, which could likely be the case due to a history of subduction in the region (LeMasurier et al., 2016), then partial melts could cause the decrease in seismic velocities (White-Gaynor et al., 2019).

The temperature field does not only affect rock densities and hence contribute to isostasy but, in general, also controls dynamic effects, such as GIA and mantle convection, in which viscosity is the crucial property. Temperature or viscosity can be derived from seismic velocity anomalies, yet with large uncertainty (Ivins and Sammis, 1995). Here we take the 3-D temperature values from our thermodynamically self-consistent model to derive mantle viscosities and point out the implications for present-day uplift rates in Antarctica, which can be compared with GPS measurements to ultimately constrain past ice thickness.

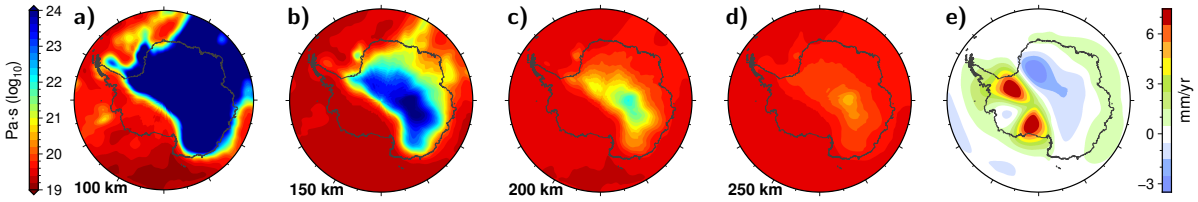

Figure 3.9.: Modeled mantle viscosity (a–d) and resulting uplift rates (e) in a dry olivine rheology and 4-mm grain size scenario. The depth slices represent values at 100 (a), 150 (b), 200 (c), and 250 km (d).

Viscosity values are computed according to equation 4 with temperatures from Model 3. As stated in section 3, we compute viscosity for dry olivine rheology and 4-mm grain size (Figure 3.9). As a result, viscosity at 100-km depth in all of EANT is so high that it is effectively elastic and can thus be considered as part of the lithosphere for GIA models. The viscosity in WANT is somewhat higher than found in earlier studies (Barletta et al., 2018; Bradley et al., 2015; van der Wal et al., 2015). Using wet rheology lowers viscosity to around 10^{18} Pa·s for large parts of WANT, in agreement with viscosity for water-saturated peridotite provided in O'Donnell et al. (2017). Lowering the grain size to 1 mm even reduces viscosity in WANT to below 10^{18} Pa·s. This corresponds to relaxation times in the order of decades. For these small relaxation times, the solid Earth response to changes in loading thousands of years ago will have reached equilibrium.

Uplift rates in Figure 3.9e show two maxima in location of former ice domes in the W12 ice history model. GPS uplift rates (Argus et al., 2014; Thomas et al., 2011) and empirical GIA models (Martin-Español et al., 2017) prefer somewhat smaller values, but note that no measurements are available in the locations of maximum uplift rates. Smaller uplift rates can be achieved with lower grain size (1 mm) or a wet rheology in our model, but these viscosities result in uplift rates of less than 1 mm/year, which is well below observed values. However, this argument rests on the assumption that all ice loading changes are accounted for, while Antarctic-wide ice loading histories such as the W12 model used in this study do not include changes in ice sheet thickness that occurred in the last centuries, and the response to those changes is absent from Figure 3.9e. A low viscosity in combination with recent ice unloading could produce significant uplift rates. The lowest viscosities obtained for the wet and small grain size rheologies are also below those inferred from observations of late Holocene ice loading relaxation, including in Iceland (Barnhoorn et al., 2011b; Sigmundsson, 1991) and parts of Antarctica (Barletta et al., 2018). Based on this, our preferred model

features the dry rheology and 4-mm grain size. The preference for GIA observations for dry rheology is subject to the uncertainties introduced by applying the olivine flow law to the upper mantle rheology deficiencies in the experimental flow law itself and our temperature model. From a petrology point of view, a completely dry rheology is plausible. The upper mantle contains on average small amounts of water (50–200 ppm; Hirschmann, 2006). Low hydration in WANT is supported by magnetotelluric measurements (Wannamaker et al., 2017) and suggested for cratons such as EANT (Peslier et al., 2010). However, possible hydration due to recent subduction in WANT (Emry et al., 2015) and the variation in flow law parameters in xenolith findings across Antarctica (see table in van der Wal et al., 2015) suggest the necessity of regional modeling of flow law parameters.

3.6. Conclusions

A comprehensive and self-consistent continental-scale model of Antarctica's lithosphere is presented in this study. Satellite gravity gradient data, seismological estimates, thermodynamic modeling, and the principle of isostasy are used to infer crustal and lithospheric thickness, density, and temperature distribution. By integrating a variety of geophysical observables and principles, a higher robustness of the result is achieved compared to modeling them separately. A precise quantification of the uncertainties of all individual geophysical properties can, however, not be obtained because the model is too computationally expensive to follow a probabilistic approach. Integrated and probabilistic modeling methods of the lithosphere are currently in development yet still in 1-D and immature (Afonso et al., 2016). Before applying them on poorly explored areas like Antarctica, they need to give proof of their reliability and robustness.

Our new Moho depth map provides higher-resolution estimates for poorly surveyed regions of EANT, where seismic station coverage is sparse or nonexistent. We find that ~30- to 35-km-thick crust is present in Wilkes Land, while the Terre Adélie Craton features distinctly thicker (~40 km thick) crust. The GSM are underlain by a marked crustal root with a ~52-km-deep Moho. Although our model cannot solve the debate about the origin and evolution of the GSM directly, it indicates that a thick and cold and thus dense lithospheric mantle is needed to compensate the thick buoyant crust to maintain isostasy.

The 3-D temperature distribution from our model is taken to infer mantle viscosity and to model present-day uplift rates for Antarctica due to GIA. Viscosity values are computed for dry olivine rheology and moderate grain size (4 mm). High viscosities imply that the GIA lithosphere is at least 100 km thick in EANT, and below 150 km in its central part. In WANT, viscosity values are around 10^{19} Pa·s, slightly above previously published values. Lowering grain size or assuming wet rheology results in uplift rates well below measured values. Our modeling prefers a dry rheology and a moderate grain size. A limitation of this estimation is, however, the absence of ice thickness variations during the last centuries in the used W12 model. Recent unloading together with low viscosity values could have a strong impact on present-day uplift rates. Therefore, future studies should include ice thickness changes in the last decades and centuries as well as 3-D variations and rheologic parameters below 400-km depth to estimate the full dynamic effect due to glacial loading.

Chapter 4

The Antarctic Mantle from a Gravity Perspective

4.1. Gravity Observations in Antarctica: Scales and Strides

Gravity data allow to detect and interpret subsurface structures related to density variations. Such features can, for instance, be troughs, sedimentary basins, sub-glacial volcanoes, intrusions, tectonic suture zones, the depth of the crust-mantle boundary (Moho discontinuity), or mantle density variations. The commonly used products for interpretation are the free-air gravity anomaly, the Bouguer gravity anomaly or the isostatic anomaly. Measured data are corrected for the station height and Earth's normal gravity, which also considers its ellipticity, which results in the free-air anomaly. If in addition the effects induced by topographic features with a constant standard rock density (2670 kg/m^3) are removed, one obtains the Bouguer gravity anomaly, which reveals density inhomogeneities in the subsurface (e.g. Nowell, 1999) such as crustal roots of mountain chains. With additional information about subsurface density structures that are relevant for the isostatic behaviour of the solid Earth, one can compute their effect on the gravity field, which is referred to as the isostatic correction (e.g. Kaban et al., 2004). After applying the isostatic correction to the Bouguer gravity anomaly, the resulting, isostatic residual anomaly reveals deviations of the Earth from the state of isostatic equilibrium.

Gravimetric measurements can be taken on the ground with high precision but requiring considerable logistical effort for remote areas and nevertheless providing of-

ten only low coverage. Therefore, nowadays mostly airborne and satellite surveys are acquired for Antarctica. In recent years, considerable progress has been made in both global Earth gravity field observations by satellite missions and regional airborne campaigns (e.g. Forsberg et al., 2018; Scheinert et al., 2016; Aitken et al., 2014; Riedel et al., 2012; Ferraccioli et al., 2011). The lateral resolution (Figure 4.1) of these two techniques ranges from 130–80 km for static gravity models derived from satellite data (Mayer-Gürr et al., 2012, 2010) to less than 10 km for airborne data (e.g. Forsberg et al., 2011). Long-wavelength satellite data are particularly useful to study the deeper lithospheric and sub-lithospheric upper mantle structures. Aerogravimetry compilations often lack these information due to post-processing and combination procedures of individual flight lines and thus focus on small-scale and shallow features. Theoretically, the maximum wavelength detectable by airborne measurements is half the extent of the surveyed area, but it is often shorter due to processing steps such as levelling (e.g. Barzaghi et al., 2014). Aerogravimetric and satellite data are therefore combined in Earth gravitational models, mathematically expressed as a spherical harmonic series, in order to achieve a high degree of consistency together with high resolution where data are available (e.g. Pail et al., 2018; Forsberg, 2015).

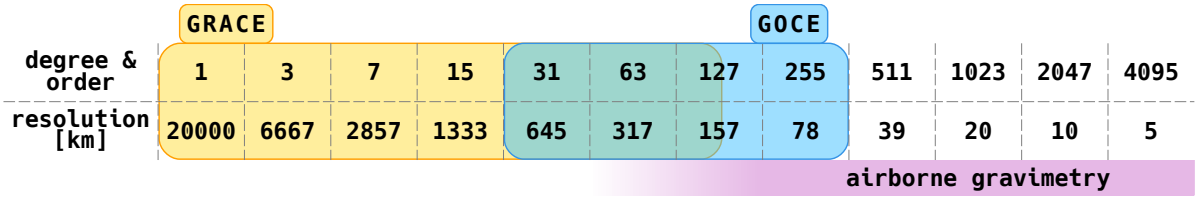

Figure 4.1.: Relation between spherical harmonic degree and order, spatial resolution, and measuring technique.

The twin-satellite mission GRACE (Gravity Recovery and Climate Experiment), orbiting Earth at ~500 km height from 2002 to 2017, did not only measure the long wavelength signal of the gravitational field with high precision (Tapley et al., 2004) but also allowed to track changes over time. In the years 2009–2013 the complementary GOCE (Gravity field and steady-state Ocean Circulation Explorer) satellite mission mapped the gravity gradient field of the Earth at ~250 km altitude (~225 km in the final stage) with its three-dimensional gradiometer (Bouman et al., 2015; Rummel et al., 2011). The gravity gradients are the second derivative of the gravitational potential, also known as the Marussi Tensor, consisting of six unique components. While the spatial resolution could be improved significantly to ~80 km, GOCE's gravity gradient measurement has a poorer sensitivity at long wavelengths, which is why

global Earth gravity models often combine GRACE and GOCE data to exploit the complementary advantages (e.g. Peidou and Pagiatakis, 2019). Due to the orbit inclination, however, both satellite missions do not cover the entire Earth, which means that data gaps at the poles exist. In case of GOCE's data the polar gap covers regions beyond 83.5° S (Brockmann et al., 2014; Forsberg et al., 2011) and is as large as 1400 km in diameter (Scheinert et al., 2016). Recent efforts have been made in the course of the PolarGAP initiative to fill the gap with extensive airborne gravity measurements (Forsberg, 2015). Great advances have also been made in collecting and compiling airborne gravimetric data for the Antarctic continent and its adjacent oceanic areas. The AntGG compilation (Scheinert et al., 2016) covers 73% of Antarctica with a 10 km resolution grid and provides free-air and Bouguer gravity anomaly estimates (Figure 4.2). Remaining gaps like the interior of Dronning Maud Land are successively filled by further surveys, which still reveal unexplored geological features, enhance existing gravity models, or confirm previously measured data (Forsberg et al., 2018; Jordan et al., 2017a; Yildiz et al., 2017). With the picture of Antarctica's gravitational signal getting successively clearer and more complete, large-scale tectonic features and crustal structures can be studied on a more robust basis. Furthermore, gravitational signatures can, together with other data like magnetic measurements, identify or assure the links between the Antarctic and its adjacent continents within the Gondwana, Rodinia, and Columbia supercontinents (Aitken et al., 2016; Scheinert et al., 2016).

4.2. The Shape Index: a Gravitational Field Curvature Product to Study the Lithospheric Structure

Since satellite gravity measurements provide a homogeneous data coverage over nearly the entire globe, one can search for similar characteristics in the gravitational field between regions in Antarctica and those in better-studied continents. Gravity gradients as measured by GOCE (Figure 4.2) are particularly suited for this purpose due to their high sensitivity to density variations in lithospheric depth ranges (Bouman et al., 2016). It is, however, challenging to interpret multiple gravity gradient components simultaneously, all the more as the tensor components can be expressed in different mathematical reference frames (Bouman et al., 2013). Combining

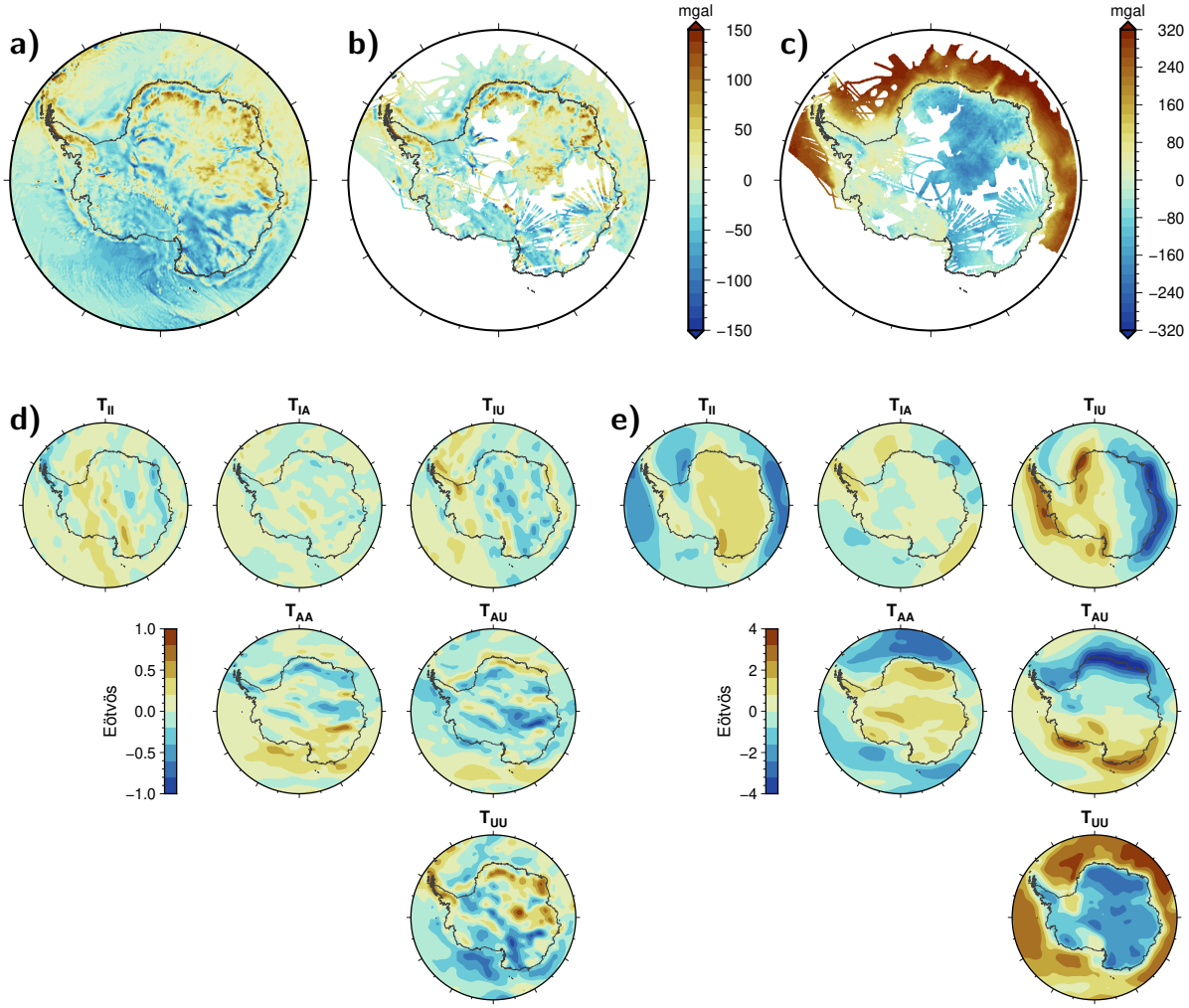

Figure 4.2.: Gravity data of Antarctica: (a) gravity anomaly of combined satellite model XGM2016 (Pail et al., 2018), (b) free-air and (c) Bouguer gravity anomalies from airborne survey data (Scheinert et al., 2016), (d) gravity gradient components from GOCE data (Bouman et al., 2016) at satellite altitude (225 km), and (e) topography-corrected gravity gradients. Gravity gradients are expressed in IAU reference frame (Pappa et al., 2019b) with axes pointing to Indian Ocean (I), Atlantic Ocean (A), and upward (U) direction.

different gravity gradient components can simplify the interpretation and thus be of use for a broad scientific community.

An example of a gravity (gradient) data product that can be interpreted relatively easily is the shape index. Hereby, the gravity gradient tensor, is translated into an index value ranging from –1 for a bowl-like shape of the equipotential surface to +1 for a dome-like shape, which are interpreted for the characteristics of the continental lithosphere. Ebbing et al. (2018) applied this technique on GOCE's global gravity gradient

data after correcting them for topographic effects. The shape index indicates mass deficits in the lithosphere with negative values (bowls) and mass surplus with positive values (domes) and thus enhances lithospheric and intra-crustal density variations. In the global view (Figure 4.3a), bowls can generally be correlated with cratonic areas and orogenic belts, e.g. the Kaapvaal Craton in South Africa and the Himalayas. In these cases, mass deficits can be explained by depleted lithospheric mantle composition in cratonic settings and thick crustal roots beneath mountain ranges. On the other hand, the Andes exhibit a valley-like shape, most likely due to the additional masses of the cold subducted slab.

In light of this global correlation, one can compare the shape index of Antarctica (Figure 4.3b) with other regions of the world. A clear distinction between West Antarctica (WANT) and East Antarctica (EANT) is obvious, particularly pronounced through high shape index values in the West Antarctic Rift System and the Weddell Sea Rift, but also above the Antarctic Peninsula. Only Marie Byrd Land exhibits a bowl-like shape in WANT. Underneath this region, a Cenozoic mantle plume has been proposed (LeMasurier and Rex, 1989), which would likely imply relatively low densities of the upper mantle due to elevated temperatures. Independently observed low seismic velocities have been interpreted as a result of such a thermal anomaly (e.g. Lloyd et al., 2015). The shape index cannot confirm the existence of a mantle plume, it is consistent with the hypothesis.

East Antarctica, on the other hand, shows entirely negative shape index values, comparable to those of other cratonic regions on Earth. In addition to a topographic correction, the gravitational field can be reduced for isostatic effects in order to bring out the isostatic state. Figure 4.3c shows the shape index for Antarctica after applying a topographic reduction and subtracting the effect of an isostatically compensated Moho. The patterns are generally similar to the observed gravity anomaly (Figure 4.2), though some differences can be identified. For instance, the Marie Byrd Land dome and the Antarctic Peninsula are more pronounced in the shape index. The Transantarctic Mountains, on the other hand, show a "flat" shape index, whereas their gravity anomaly is distinctly positive with more than 50 mGal. This can be interpreted as an expression of a missing crustal root beneath the Transantarctic Mountains (e.g. Hansen et al., 2016) and their still unresolved isostatic state and uplift history (e.g. Lisker et al., 2013).

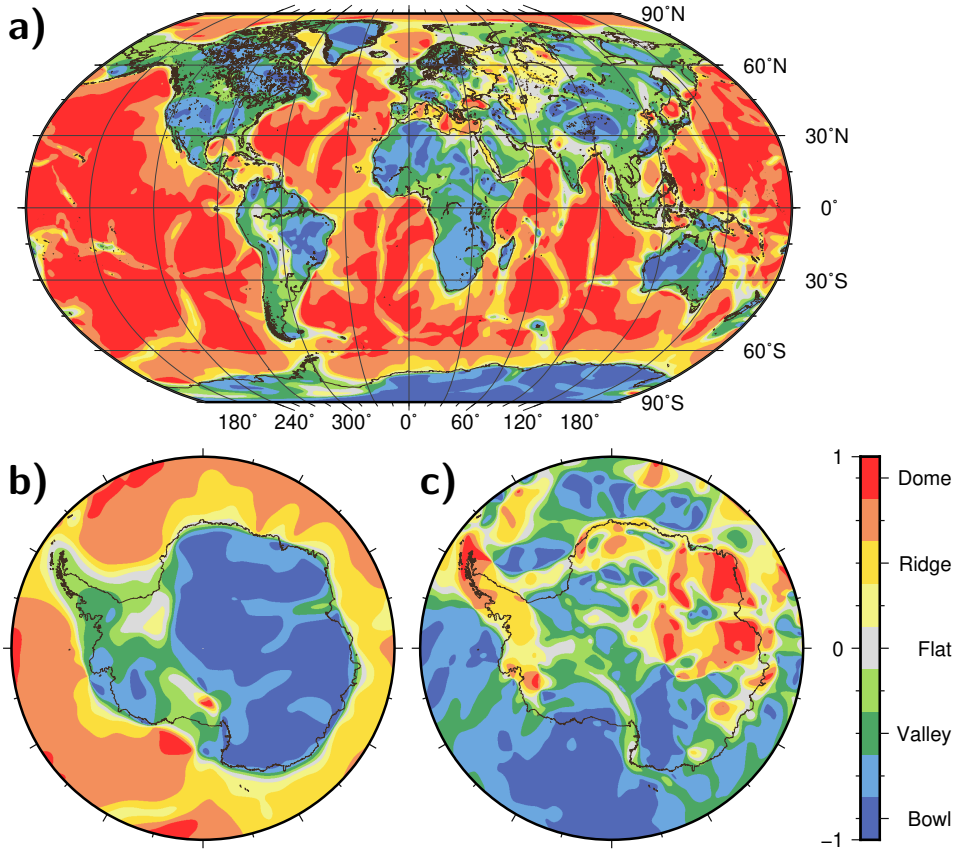

Figure 4.3.: Shape index based on GOCE gravity gradient data after topographic correction for (a) the Earth and (b) Antarctica (based on Ebbing et al., 2018). Panel (c) shows the shape index for Antarctica after additional correction for isostatic effects.

4.3. Crustal Thickness of Antarctica from Gravity Data

The Moho boundary limits crustal and mantle rocks and is, in general, associated with the most prominent density contrast in the lithosphere. Depending on the tectonic setting, the density contrast can vary between less than 200 kg/m^3 in cratonic regions when eclogitization is involved, and more than 500 kg/m^3 in extending basins or Phanerozoic orogens (Rabbel et al., 2013). Therefore, depth, geometry, and density contrast at the Moho interface have a huge impact on the gravity field at a broad range of wavelengths (e.g. Sebera et al., 2018). Since geothermal heat flux, seismic velocities, and several other geophysical and geological parameters are strongly affected by the crustal thickness, knowledge about the Moho depth is of broad importance.

However, the observed gravity signal originates from several sources, and the free air anomaly is largely affected by topography. In order to isolate the signal from the Moho boundary, effects from other sources, such as intra-crustal (sedimentary basins) and mantle density variations or dynamic forces as well as topography, ice, and water, need to be subtracted from the total signal. In case of Antarctica, the estimation of the sub-ice architecture is challenging. Nevertheless, huge progress has been achieved by establishing the Bedmap2 model (Fretwell et al., 2013), which describes the surface elevation, the ice thickness, and the sea-floor and sub-glacial bed elevation of the Antarctic and is about to be updated by Bedmap3 (Fretwell, 2019).

Since sedimentary rocks can have significantly lower densities than crystalline crust, it is crucial to incorporate them in a topographic reduction model. A compilation of offshore sedimentary basins in the Antarctic has recently been published (Straume et al., 2019), showing more than 12 km thick sediments in the Weddell Sea sector and up to 8 km in the Ross Sea region. The availability of data for sediment thickness is much worse for the East Antarctic onshore areas. Few studies exist that estimate the depth of inland subglacial basins from aerogeophysical surveys (e.g. Frederick et al., 2016; Aitken et al., 2014; Ferraccioli et al., 2011; Bamber et al., 2006; Mishra et al., 1999), predominantly in the Wilkes Land region, or seismic methods in Lake Vostok (Isanina et al., 2009; Filina et al., 2008) and its periphery (Studinger et al., 2003). It is, however, extremely challenging to establish a trustworthy model for thicknesses and densities of East Antarctica's sedimentary basins from the available data, which would also have to account for different degrees of compaction, infill composition, and age, if supposed to be used in a gravimetric topographic reduction.

Multiple techniques exist to infer the Moho depth from gravimetric observations. The most widely used one is the Parker–Oldenburg scheme (Oldenburg, 1974; Parker, 1973). This approach mathematically relates the geometry of a 2-dimensional interface with a vertical gravity anomaly and can thus be used to invert the inferred Bouguer anomaly of a particular region into a Moho depth model. It implies, however, a flat Earth approximation and requires presumptions of a certain (constant) density contrast and a reference depth for the Moho. Moreover, the data needs to be given at Earth surface level, which means that low pass filtering and downward continuation must be performed on satellite gravity observations to prevent numerical instabilities and noise amplification.

Block et al. (2009) followed this approach and used GRACE satellite gravity data to estimate the crustal thickness of Antarctica, assuming a reference depth of 35 km and an density contrast of 500 kg/m^3. Notwithstanding the rather high uncertainties of the first Bedmap model (Lythe and Vaughan, 2001), Block et al. (2009) were able to ascertain the huge contrast in crustal thickness between West Antarctica (WANT) with ~30 km and East Antarctica (EANT) with ~40 km and estimated the crustal root beneath the Gamburtsev Subglacial Mountains (GSM) to be as thick as 42 km. Seismological surveys, however, estimated the crustal thickness to be thinner (ca. 20–30 km) in WANT (e.g. Shen et al., 2018; Ramirez et al., 2016; Chaput et al., 2014) and much thicker (>50 km) beneath the GSM (e.g. An et al., 2016; Hansen et al., 2010; Lawrence et al., 2006b). This discrepancy suggests that a single density contrast and reference depth is not applicable for the whole Antarctic continent with its diverse tectonic provinces (Pappa et al., 2019a). Accounting for that, O'Donnell and Nyblade (2014) performed separate inversions of the Moho depth for West and East Antarctica and constrained the solutions with local seismological Moho depth estimates. Their results indicate a >50 km thick crustal root beneath the GSM while a ~23–27 km thick crust is largely suggested for WANT. Integrating seismological findings in the inversion of gravity data enabled the authors to reduce the inherent ambiguity of potential solutions significantly (see also van der Meijde et al., 2015; Schmidt et al., 2011). Despite these methodological improvements, however, it is still not viable to derive a Moho depth model for Antarctica from gravity with constraining seismic data that accounts for the diverse tectonic regimes of the continent (Pappa et al., 2019a).

Gravity-derived Moho depth models of Antarctica show similar morphologies owed to the methodological relatedness. In contrast to this, Moho models based solely on seismological data are notably diverse (e.g. Haeger et al., 2019; Baranov et al., 2018; An et al., 2015b; Baranov and Morelli, 2013) and differ for more than 10 km in large areas of the continent. One reason is the variety of applied seismological methods and their respective sensitivities to noisy factors like ice reverberations. *S* wave can be preferable to *P* wave receiver functions in this context (e.g. Hansen et al., 2016). Another source for the disagreement of seismological models lies in the sparseness of seismic stations in Antarctica and the interpolation method for blank areas. Surface wave analyses can estimate the physical properties of the subsurface between seismic stations from dispersion curves, whereas numerical interpolation algorithms like the Kriging method fill the blank areas based on local Moho depth information in the vicinity (Haeger et al., 2019; Szwillus et al., 2019; Baranov and Morelli, 2013).

Figure 4.4a–f shows six Moho depth models derived with different methods. All models show the striking contrast in crustal thickness between WANT and EANT as well as some prominent features with thicker crust like the GSM, the southern Transantarctic Mountains, and (with the exception of the AN1-Moho model) Marie Byrd Land. The concept of vote maps (Shephard et al., 2017) can be used to illustrate the degree of consistency between models and to identify common features (Figure 4.4g–i). This simple method counts the number of models that match a certain criterion. All presented Moho depth models agree on a >30 km thick crust in whole EANT, represented by white colour in Figure 4.4g. Likewise, large parts of WANT consistently show a Moho depth shallower than 30 km (red colour), whereas the picture is diverse in the Weddell Sea region, the Antarctic Peninsula, and the vicinity of the Marie Byrd Land dome. In EANT, on the other hand, only a few spots are present where at least a majority of the models exhibits a crust thicker than 40 km (yellow–red colour in Figure 4.4i. Dark blue and green colours indicate disagreement between the models.

4.4. Using Satellite Gravity Data to Investigate the Upper Mantle Structure of Antarctica

Joint interpretations of seismic findings and gravity data or isostasy (Pappa et al., 2019a; An et al., 2015b; O'Donnell and Nyblade, 2014) suggest a laterally varying density contrast at the crust-mantle boundary, implying a heterogeneous upper mantle density structure beneath Antarctica. This is also indicated by seismic velocity models (e.g. Lloyd, 2018). The dominating factors for both density and seismic properties of mantle rocks are temperature and composition. However, the relationships between these parameters are fundamentally different and partly non-linear or discontinuous due to mineral phase changes (e.g. Stixrude and Lithgow-Bertelloni, 2005; Cammarano et al., 2003). For instance, the principle of isopycnicity (Jordan, 1988) describes that density changes of mantle rocks due to temperatures can be compensated by opposite density changes due to compositional depletion (for discussion see also Artemieva et al., 2019; Eaton and Perry, 2013; Kaban et al., 2003). Thermodynamic modelling of stable mineral assemblages (e.g. Connolly, 2005) of mantle rocks under given pressure and temperature conditions can be used to establish lithospheric models that are self-consistent in terms of density, temperature, and seismic velocities (e.g. Fullea et al., 2015, 2012). With this tool at hand, one can attempt to investigate the na-

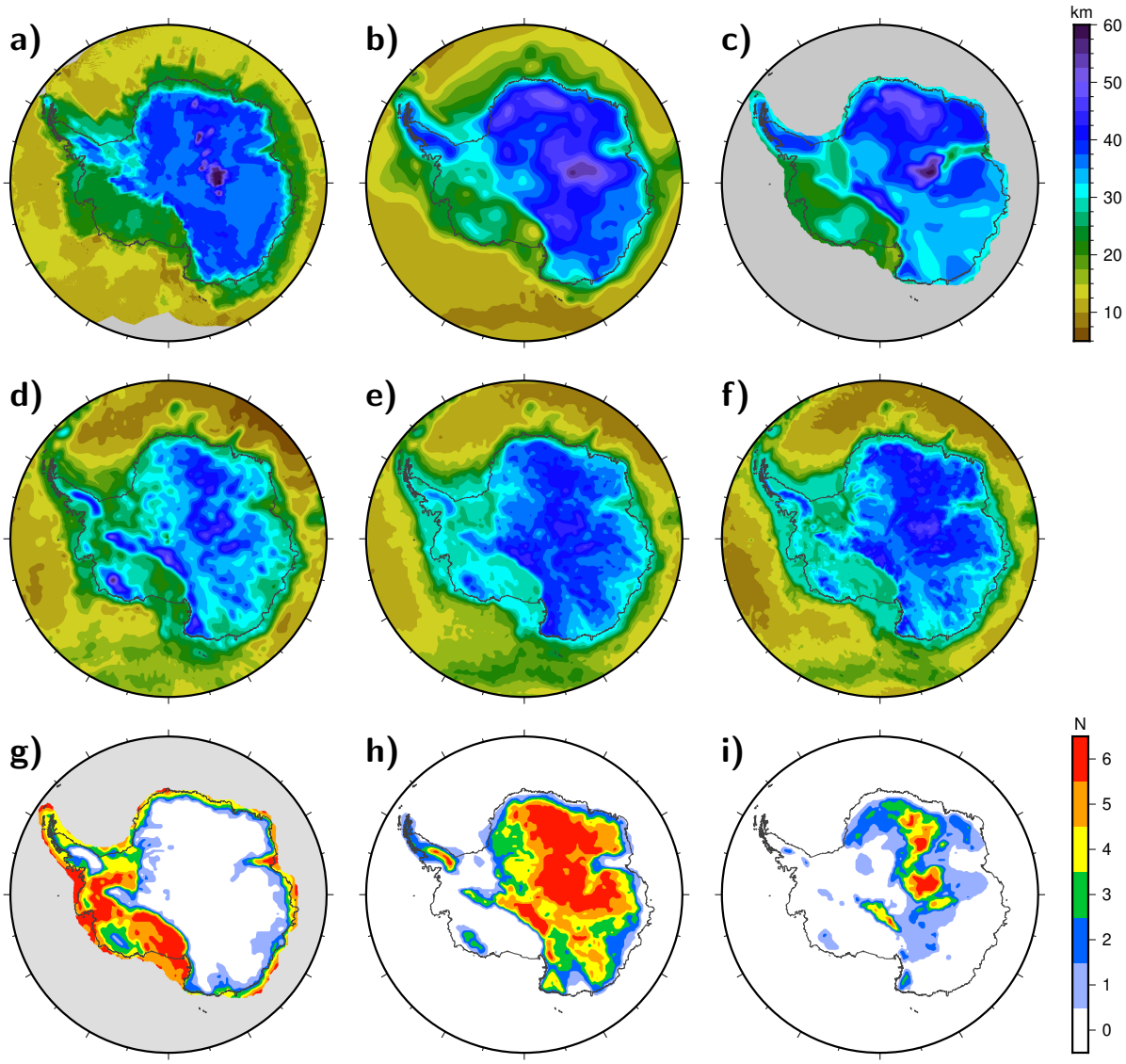

Figure 4.4.: Top: Moho depth models derived with different methods. (a) Surface wave analysis: AN1-Moho (An et al., 2015b), (b) Kriging interpolation between local seismologically derived Moho depth estimates (Haeger et al., 2019), (c) integrating seismic estimates, gravity data, and isostasy (Baranov et al., 2018), (d) inversion of GOCE gravity gradient data: GEMMA (Reguzzoni and Sampietro, 2015), (e) gravity inversion constrained with seismic estimates (Pappa et al., 2019a), (f) Airy-isostatic Moho depth model (Pappa et al., 2019a). Bottom: vote-maps for different depth ranges illustrate the degree of agreement of the above models; (g) less than 30 km Moho depth, (h) more than 35 km, (i) more than 40 km. Reddish areas show high agreement, e.g. shallow Moho in the WARS (g), whereas only a few spots exist in EANT (i) where all models see a >40 km thick crust.

ture of the upper mantle of Antarctica by integrating seismological velocity models and satellite gravity data (Haeger et al., 2019). For this purpose, however, it is nec-

essary to first separate the gravity signal originating from the lithospheric mantle as accurately as possible (e.g. Kaban et al., 2010). Hence, a crustal thickness and density model is needed., which is, as described above, subject to large uncertainties in case of Antarctica. Haeger et al. (2019) used existing seismological information on Moho depth and seismic velocities in Antarctica to derive a crustal model through interpolation for a joint inversion of gravity and seismic tomography data with the aim to infer the density, temperature, and composition of the Antarctic upper mantle. Notwithstanding the poor data situation, the authors were able to show that large parts of East Antarctica's lithospheric mantle are likely strongly depleted in iron and enriched in magnesium (Figure 4.5), indicated by a high magnesium number (Mg# = 100 Mg/(Mg+Fe)), which suggests cratonic settings of Proterozoic to Archaean age. The fact, however, that different up-to-date seismological tomography models lead to inconsistent results in the inversion process demonstrates the need for further field campaigns to collect data, which allow to establish more robust models of Antarctica's lithospheric structure.

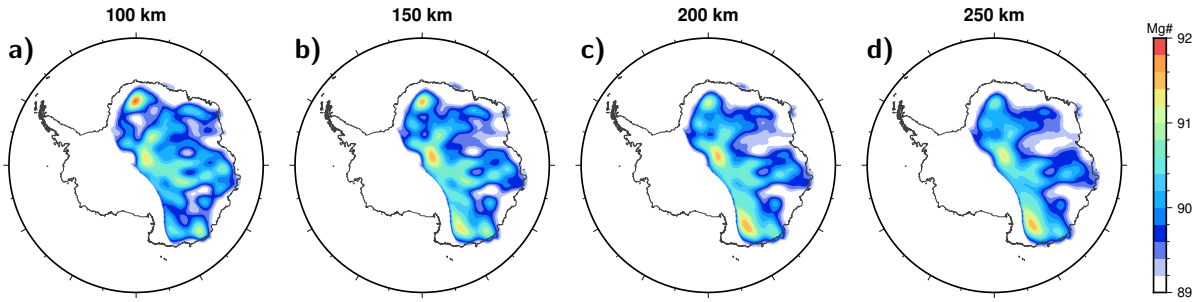

Figure 4.5.: Depletion variations in terms of Mg# estimated for (a) 100, (b) 150, (c) 200, and (d) 250 km, based on AN1-S model (after Haeger et al., 2019).

As long as the seismic station coverage of the Antarctic continent remains sparse, and in consequence seismological models cannot provide the degree of certainty required for gravity modelling, other strategies must be pursued in order to investigate the architecture of the Antarctic lithosphere. One possibility is to model the lithosphere as a whole while considering all those parameters and processes that determine the observables for which data are available. For instance, the temperature strongly affects rock densities due to thermal expansion, the stable mineral assemblage, and the elastic behaviour and thus seismic velocities. Correspondingly, the thermal field of the lithosphere can reasonably be computed by solving the heat transfer equation, whereas the gravity field resulting from the modelled densities and the seismic velocities can be compared with measured data.

Despite the advantages, it is still necessary to make *a priori* assumptions about some parameters like crustal and mantle rock parameters, which are poorly explored or unknown for large parts of Antarctica. For establishing a lithospheric model of Antarctica, Pappa et al. (2019b) relied on petrological studies to define broad regions of different tectonothermal age (Figure 4.6), which we associated with varying degrees of depletion of lithospheric mantle composition. According to the pressure and temperature conditions inside the model, the stable mineral phases (and thus the density) of the respective peridotitic composition were inferred through the thermodynamic modelling software Perple_X (Connolly, 2005). Additionally, representative global values were taken for crustal density and thermal parameters. With this initial set-up, the model was iteratively fitted to the observed topography by maintaining isostatic equilibrium and the satellite gravity gradient data measured by GOCE, always maintaining internal consistency in the relationships between all model properties. Main results of this study are new estimates of the Moho depth and the total lithospheric thickness of Antarctica (Figure 4.6).

Local seismic Moho depth estimates can serve as *a posteriori* benchmark instead of using them as an input or constraint as described above. Since the density contrast at the Moho discontinuity in the lithospheric model is a function of temperature, pressure, and rock properties, it can vary freely, which in result leads to a generally good fit of both the gravity gradient data and the seismic Moho depth estimates. In particular, the crustal root beneath the GSM is deeper (~54 km) in this model than in classical gravity inversions and has a high density of >3150 kg/m^3. A very small density contrast in this region was previously suggested by other studies (An et al., 2015b; Ferraccioli et al., 2011). The modelled total lithospheric thickness is largely similar to seismological estimates (An et al., 2015a) and likewise exhibits a stark contrast between thin lithosphere (~80 km) in WANT and up to 260 km in EANT. Having such a temperature model of the crust and upper mantle at hand, which is in agreement with topographic (isostatic), seismic, and gravity gradient data, offers the opportunity to derive upper mantle viscosities (Pappa et al., 2019b). Especially in Antarctica, it is crucial to consider the 3-dimensional variations of viscosity instead of using 1D models (Nield et al., 2018) in estimating the glacial isostatic behaviour of the solid Earth, e.g. present-day uplift rates, due to ice mass changes.

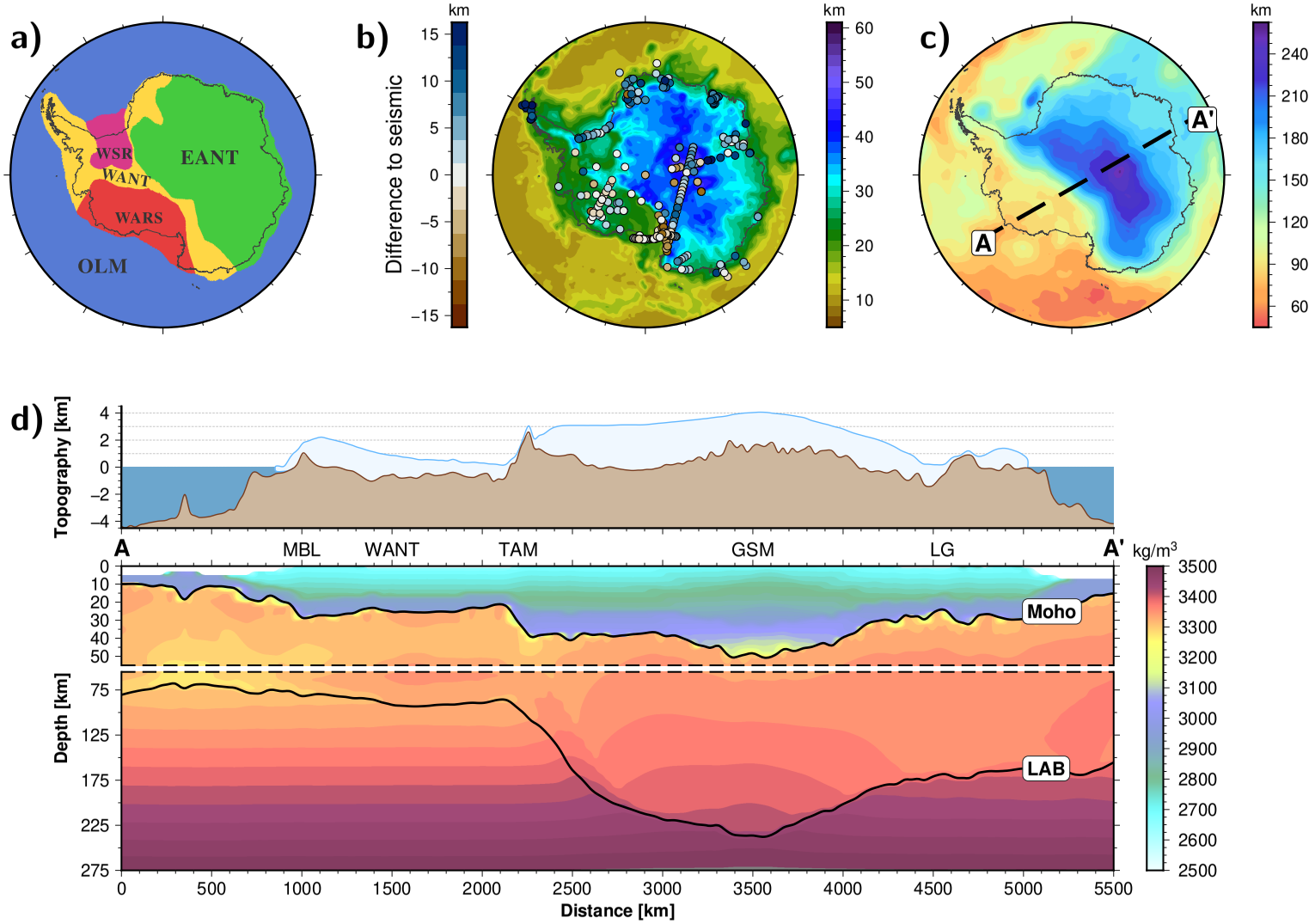

Figure 4.6.: (a) Domains of different lithospheric mantle composition in the model from Pappa et al. (2019b); (b) resulting Moho depth with local seismic estimates as benchmark (coloured circles); (c) resulting total lithospheric thickness; (d) density cross-section from A–A′ (see c).

Chapter 5

Regional Upper Crustal Density Inversion of Antarctica by Using a Lithospheric Model for Background Gravity Field Estimation

5.1. Introduction

Recent compilations of airborne gravity campaigns of Antarctica cover almost three quarters of the continent (Scheinert et al., 2016), which allows to study geological features at a regional to local scale. A homogeneous coverage of the continent, however, is only provided by gravity models based on satellite data, which, on the other hand, have a lower resolution. Separating shallow and deep sources in the gravity signal is not straight forward. This is particularly the case if the knowledge about the crustal setting is as poor as in Antarctica, for instance with respect to the presence of sedimentary basins. For the sake of simplicity, it is often assumed that long wavelength parts of the gravity signal originate from deep sources, whereas shallow density variations are supposed to generate short wavelengths. Following this assumption, low-pass or high-pass filtering is usually carried out to separate the sources in the spectral domain. It is, however, also possible that shallow density variations create long-wavelength signals (e.g. Sebera et al., 2018). Other methods are thus needed to utilize gravity data in order to infer the crustal structure if further constraining information is rare.

A common approach to investigate intra-crustal density variations is to compute an isostatic anomaly of the gravity field (e.g. Blakely, 1995; Simpson et al., 1986). However, since near-surface structures are generally at least partly isostatically compensated, their effect on the isostatic anomaly is counteracted by compensating masses (e.g. Cordell et al., 1991). To account for that, a decompensative correction can be applied in addition, which requires additional constraining data such as estimates of a compensation depth (Kaban et al., 2017), provided for instance by a Moho depth model, which is subject to high uncertainties in the case of Antarctica (Pappa et al., 2019a).

In a recent study, Haeger and Kaban (2019) computed isostatic and decompensative gravity anomalies for Antarctica by using satellite and airborne gravity data in combination with a seismology-derived crustal model. The decompensative anomaly was used to infer locations and thickness estimates of sedimentary basins of the continent. The authors were able to partly confirm the presence of known sedimentary basins from their results but also inferred previously unmapped sub-glacial sediment deposits in East Antarctica. Some known sedimentary basins, however, did not appear in their results. This ambiguity may be attributed to the uncertainties of Moho depth estimates in Antarctica due to large gaps in seismic coverage (e.g. Pappa et al., 2019a). The findings from Haeger and Kaban (2019) suggest density variations in the crust that can also have a significant gravity effect at satellite level. It remains unclear to what extent this may affect previous studies on the deeper Antarctic lithosphere using satellite gravity data (Haeger et al., 2019).

With robust information about the large-scale lithospheric structure, particularly the depth of the Moho discontinuity and crustal and upper mantle densities, one can establish a background density model (e.g. Pappa et al., 2019b) that can be used to calculate a residual gravity field, which in turn can be used to invert for near-surface density variations, e.g. in the upper crust. A basic assumption of this approach is that the long-wavelength part of the gravity signal is entirely represented by the lithospheric background model, whereas shorter wavelengths can be explained by small-scale, shallow sources. In an iterative process, inverted broad-scale density variations can be incorporated in the background density model. The latter is hence expected to represent gravity data at satellite height, while shorter wavelengths, as they are contained in airborne gravity models, are reflected by small-scale and shallow density variations.

A major requirement for the initial lithospheric background model is a high degree of robustness, which can be achieved by involving constraining data from multiple geophysical methods. In the following, the 3D model of the Antarctic lithosphere established in Pappa et al. (2019b) by utilizing satellite gravity gradient data will be used to represent the long-wavelength gravity field and thus separate short-wavelength variations. These gravity residuals will be inverted into near-surface crustal density variations, which can be of help in further studies of geological features, e.g. sub-glacial basins or mafic intrusions, of the Antarctic lithosphere.

5.2. Data and Background Model

The recent Earth gravitational model XGM2019 (Zingerle et al., 2019) (Figure 5.1a) provides combined satellite-based and terrestrial estimates of the gravity field over Antarctica, expressed in a spherical harmonic series up to degree and order 2190, which corresponds to a spatial resolution of ~10 km. In contrast to the XGM2016 model (Pail et al., 2018), it also includes the AntGG compilation of airborne gravity data (Scheinert et al., 2016) and is therefore highly suitable for a near-surface gravity inversion over Antarctica. The AntGG compilation covers 73% of Antarctica's area. Several existing data from different sources, mainly aero-geophysical campaigns, are included, which makes it challenging to harmonize and level them into a consistent model. A high degree of consistency in the regional gravity field data was achieved by applying a remove-compute-restore technique with a satellite-only gravity background model (GOCO03S, Mayer-Gürr et al., 2012), which is independent from terrestrial data and provides homogeneous covering particularly in the long-wavelength part. We use the full expansion of the gravity disturbance from XGM2019 at 10 km height above the WGS84 ellipsoid for the inversion. This altitude ensures that all station points are outside the masses while still close to the surface. The data is first extracted in a grid of 0.1° resolution, then projected into Antarctic Polar Stereographic coordinates and re-gridded into a regular 10 km spacing.

In order to compare the gravity data from XGM2019 with the lithospheric background model and therefore to separate the signal supposedly originating from shallow density variations, a Bouguer gravity correction needs to be applied. We use the Bedmap2 dataset (Fretwell et al., 2013), which provides estimates about surface elevation, ice thickness, and the sea-floor and sub-glacial bed elevation (Figure 5.1b) of the Antarc-

tic. For the computation of the ice-topographic reduction model (Figure 5.1c), we use density values (e.g. Rignot et al., 2008) of 1028 kg/m^3 for water, 917 kg/m^3 for ice, and 2670 kg/m^3 for rock topography.

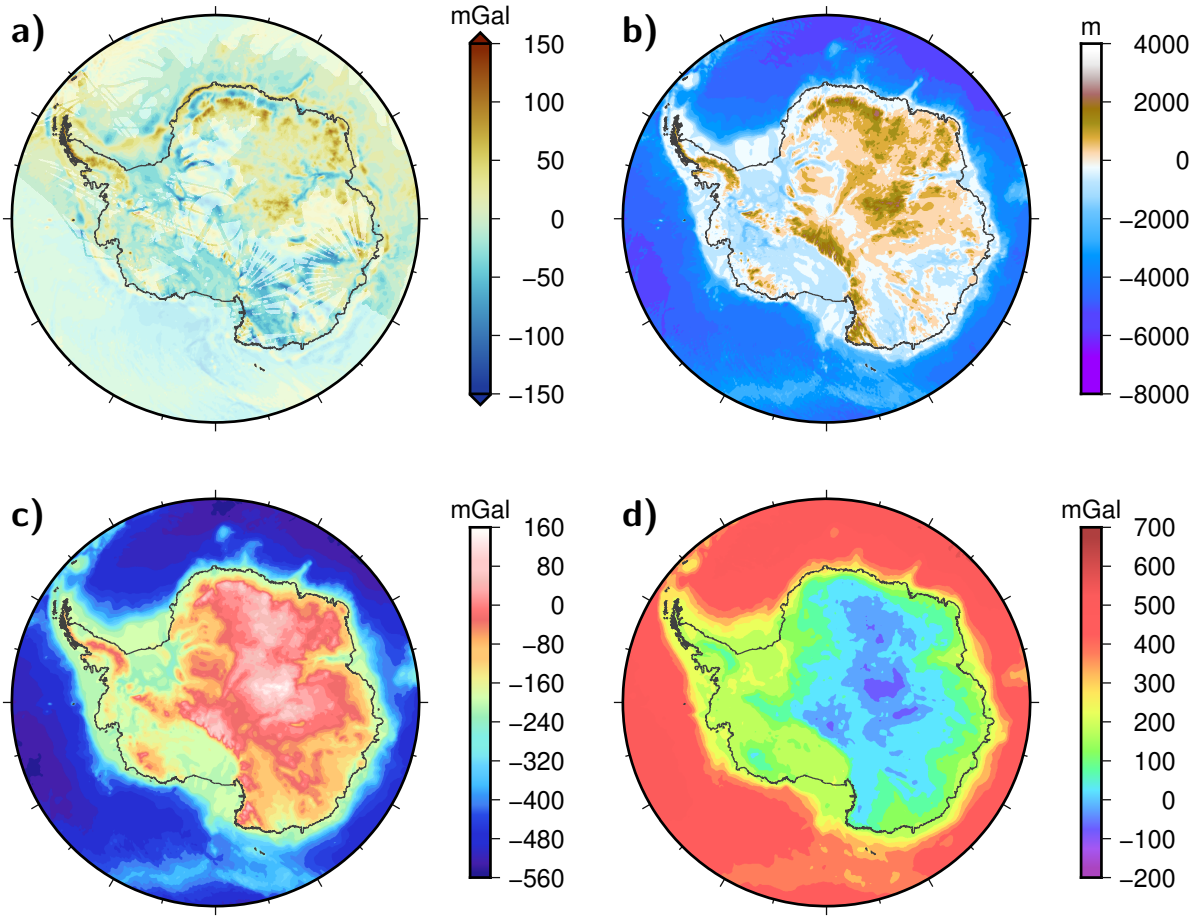

Figure 5.1.: Data used in the inversion. (a) Gravity anomaly from XGM2019. Areas without airborne data are dimmed. (b) bedrock topography and (c) ice-topographic correction model based on Bedmap2, (d) resulting Bouguer anomaly. All gravity signals are at 10 km height above the ellipsoid.

The lithospheric model of Antarctica from Pappa et al. (2019b) is taken as a background density model. From now on, we refer to this model as the LitMod3D model. To establish this model, seismological and petrological models were combined with satellite gravity gradient data in a self-consistent framework (LitMod3D, Fullea et al., 2009). A detailed description of the used data and methodology is given in Pappa et al. (2019b). The resolution of the model is 50 km laterally and 2 km vertically. In order to obtain subsurface density variations, we subtract a piece-wise linear reference model (Pappa et al., 2019b, Figure 3) with density increasing with pressure in

the crust (above 30 km) and the mantle (below 30 km). The forward-computed gravity signal from this density variation model (Figure 5.2a) can be compared with a Bouguer gravity anomaly from the measured data (Figure 5.1d). For the purpose of a comparative interpretation, we also use magnetic anomaly data from the ADMAP-2 compilation (Golynsky et al., 2015).

5.3. Method

The computation of the gravity effect from the ice-topographic correction model and the LitMod3D model is done with the software Tesseroids (Uieda et al., 2011). The density models are discretized into tesseroid volume elements, which are segments of a sphere defined by their upper and lower meridians and parallels plus by their top and bottom radii (as distance from the Earth's centre). Because the ice-topo correction model from Bedmap2 has a high resolution, which also defines the topography, the respective tesseroid model must likewise have a high resolution in order to ensure that masses are preserved and correctly located. We use tesseroids with an edge length of ~11 km to compute the topographic correction model. In contrast to that, the lithospheric model only represents subsurface density variations and has a native lateral resolution of 50 km. Here, tesseroids with an edge length of ~25 km are sufficient for our computation. The gravity effect of the tesseroid models is calculated at the same stations as the XGM2019 data at 10 km height. Finally, the gravity effect of the correction model is subtracted from the XGM2019 data, which gives the Bouguer anomaly. Subsequently, the effect of the LitMod3D model is stripped from this Bouguer anomaly in order to obtain the gravity residual (Figure 5.2b), which will be inverted into density variations within the upper crust.

For the inversion, we use the GM-SYS 3D package from Geosoft's Oasis montaj® software suite. It uses an iterative inversion algorithm modified after Parker and Oldenburg (Oldenburg, 1974; Parker, 1973). In our approach, the geometry of the model is kept fixed, whereas the density is allowed to vary in order to fit the observed gravity residual. A constant shift in the gravity signal can be identified and isolated before estimating the misfit and fitting the model. The data to be inverted is the differential gravity signal between the Bouguer anomaly based on the XGM2019 and the Bedmap2 models and the LitMod3D model at 10 km height above the WGS84 reference ellipsoid. The physical property to be inverted for is the lateral density variation

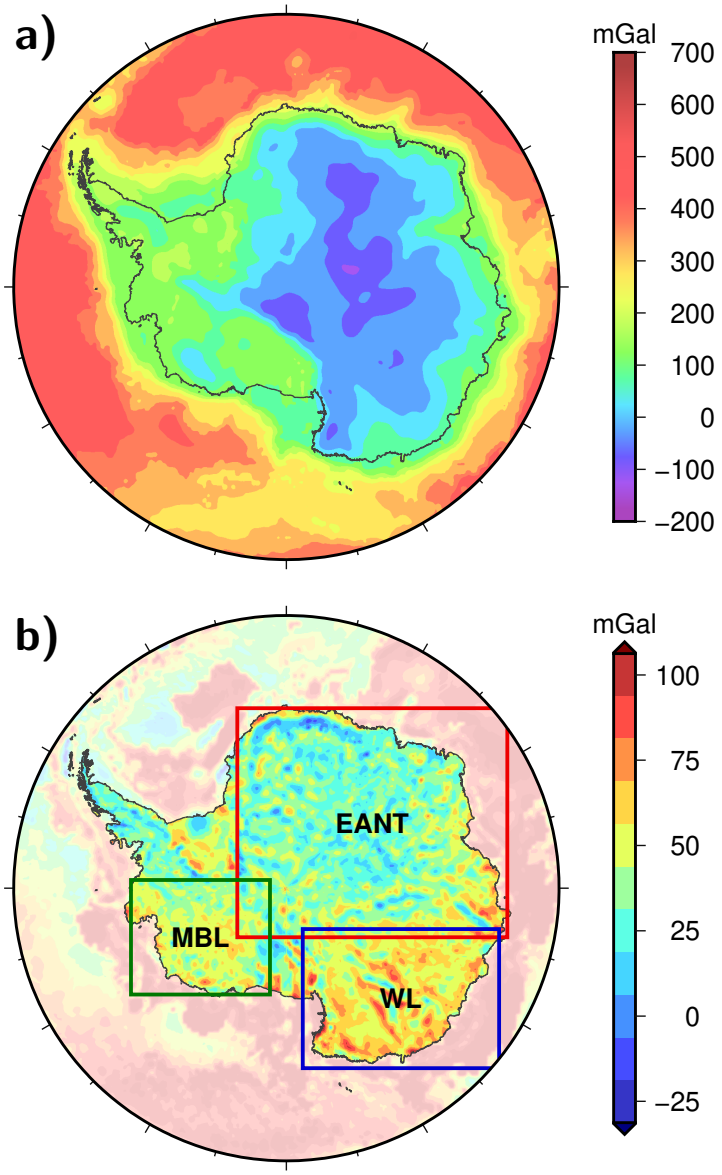

Figure 5.2.: (a) Gravity effect of the lithospheric density background model at 10 km height above the ellipsoid. Panel (b) shows the difference between (a) and the Bouguer anomaly shown in Figure 5.1d. Colours are dimmed in offshore areas . The three rectangles highlight the separate study areas for the density inversion. EANT=East Antarctica; MBL=Marie Byrd Land; WL=Wilkes Land.

inside a layer limited at 12 km depth below the ellipsoid as bottom and the bedrock topography from Bedmap2 as top. The density value is vertically constant in each column of this layer (10 km $\times$ 10 km base area). As abort criterion for the inversion, we use a root-mean-square misfit value of 0.5 mGal. Because the inversion algorithm requires a rectangular study area, we select three separate areas (Figure 5.2b): (1) Marie

Byrd Land (MBL) in West Antarctica, (2) Wilkes Land, and (3) East Antarctica (EANT). All study areas are laterally discretized in a 10-km-spaced grid.

5.4. Results and Discussion

The inversions reached the desired residual misfit of 0.5 mGal after a few iterations (8 iterations for MBL and EANT, 7 iterations for Wilkes Land). The shift in the gravity signal accounts for 30.4 mGal (MBL), 32.5 mGal (Wilkes Land), and 42.3 mGal (EANT), respectively, and may be induced by the reference model or by the Fourier approach of the inversion algorithm. Figures 5.3d–5.5d show the resulting lateral density variation within the upper crust that reproduces the differential gravity in Figure 5.2b.

All three study areas show a markedly positive inverted density of >200 kg/m^3 in offshore areas, which corresponds to the positive residual gravity shown in Figure 5.2b. This is likely a result of imperfect modelling of offshore sediments, e.g. due to the choice of a simplified compaction density model (Pappa et al., 2019b). In onshore areas, all three study areas exhibit density variations mostly in the range of $\pm$100 kg/m^3. No clear correlation with the bedrock topography or ice thickness is apparent, which can be regarded as a sign of a high grade of quality of the ice-topographic correction model. In comparison to that, some similarities appear in the magnetic anomaly data from ADMAP-2 (Golynsky et al., 2015).

In MBL, negative values of the inverted density variation are present in the region of the Marie Byrd Land Dome (Figure 5.3), which is characterized by its high topography. However, the estimated uncertainty in the Bedmap2 dataset is very high with more than 1000 m in this area because of data gaps (Fretwell et al., 2013). By contrast, the region of low topography in the central West Antarctic Rift System is characterized by positive inverted density variations of ~50–120 kg/m^3. The LitMod3D model assumes continental crust in this area with density values of ~2700 kg/m^3. Positive inverted density values may indicate that the crust actually has a higher density, potentially associated with mafic composition, which would be consistent with the high abundance of volcanoes in the central West Antarctic Rift System (van Wyk de Vries et al., 2017), though not all of them are supposed to be characterized by mafic material. For the whole study area segment, we cannot identify any conclusive correlation of the inverted density with the magnetic anomaly data. Furthermore, the central

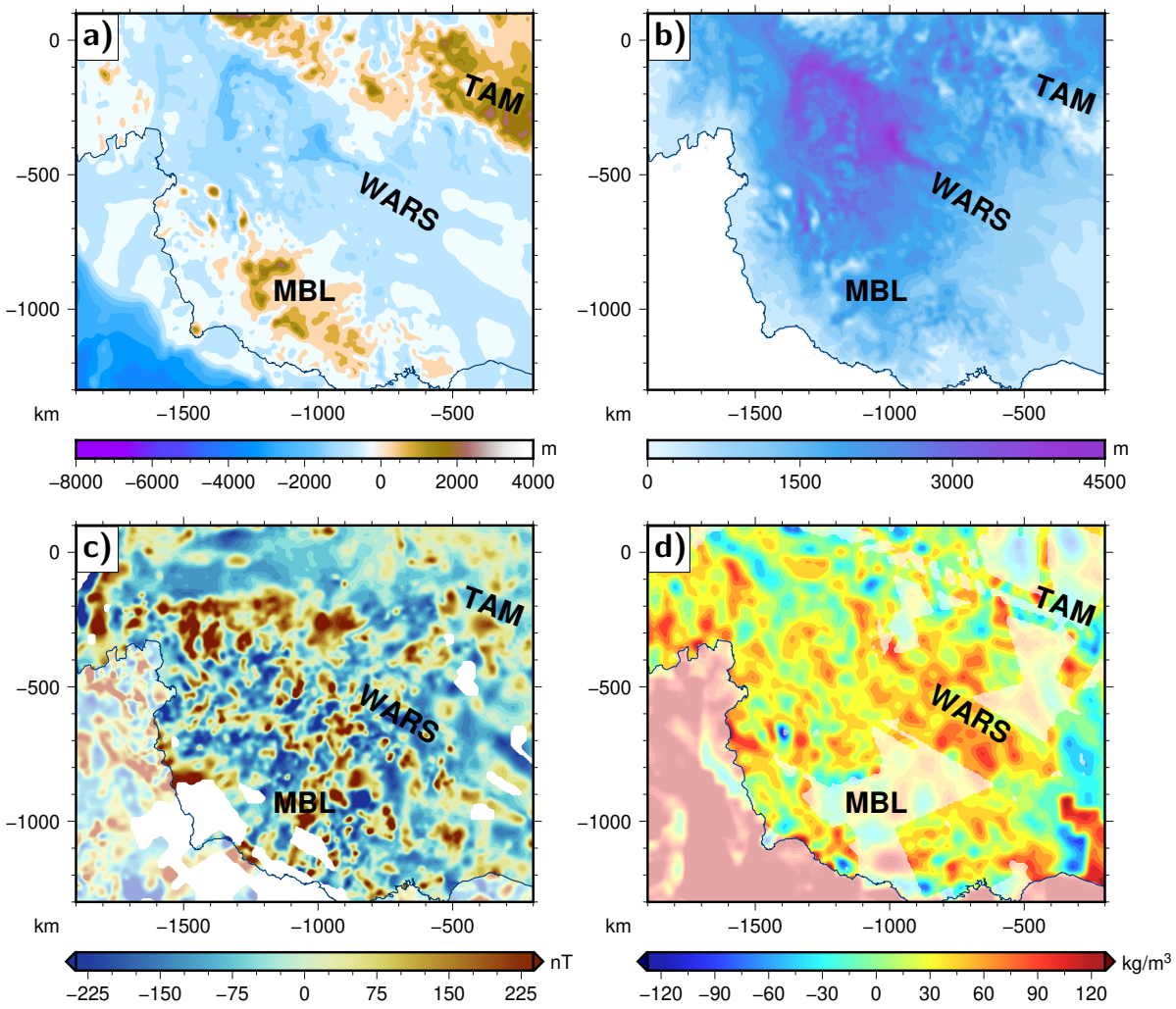

Figure 5.3.: Data and results for Marie Byrd Land segment. (a) Bedrock topography, (b) ice thickness, (c) magnetic anomaly, (d) inverted density variation. Offshore values are dimmed in panels (c) and (d). Areas without airborne data are additionally dimmed in panel (d). MBL=Marie Byrd Land; TAM=Transantarctic Mountains; WARS=West Antarctic Rift System.

Transantarctic Mountains, which are located in the upper right corner of Figure 5.3a, are not visible at all in the inverted density map.

The same applies for the northern Transantarctic Mountains in the Wilkes Land study area (Figure 5.4). Instead, high variations are present in the area of the Terre Adélie Craton (e.g. Ferraccioli et al., 2009a). These patterns are again not clearly correlated with the bedrock topography, even though the relief is strong in that region. While some lineaments of positive density variation seem to follow topographic structures of high elevation, they are not continuous and not entirely congruent. The magnetic

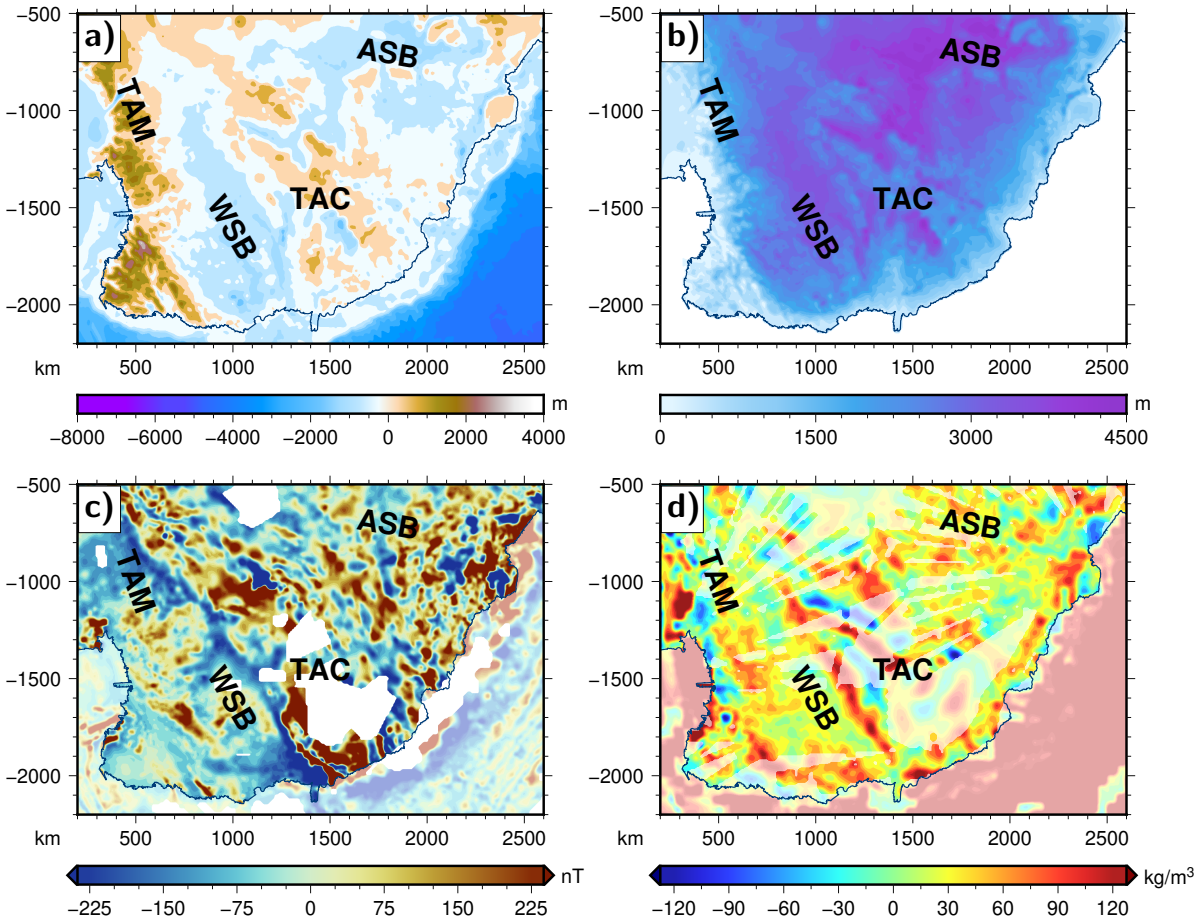

Figure 5.4.: Data and results for Wilkes Land segment. (a) Bedrock topography, (b) ice thickness, (c) magnetic anomaly, (d) inverted density variation. Offshore values are dimmed in panels (c) and (d). Areas without airborne data are additionally dimmed in panel (d). ASB=Aurora Subglacial Basin; TAC=Terre Adélie Craton; TAM=Transantarctic Mountains; WSB=Wilkes Subglacial Basin.

anomaly of the region (Figure 5.4c), on the other hand, reveals structures that match the inverted density more clearly, especially in the southern part of the Terre Adélie Craton and at its boundary to the Wilkes Subglacial Basin. The big sub-glacial basins in Wilkes Land, that is the Wilkes Subglacial Basin and the Aurora Subglacial Basin (Aitken et al., 2014), are not reflected in the inverted density, although they are clearly visible in the bedrock topography and partly in the magnetic anomaly maps.

In the third study area segment, EANT, the inverted density (Figure 5.5d) shows apparently arbitrary patterns throughout the onshore area, and almost no major geological features are visible. However, suture zones and sedimentary basins of Precambrian age have been proposed based on combined interpretation of gravity and

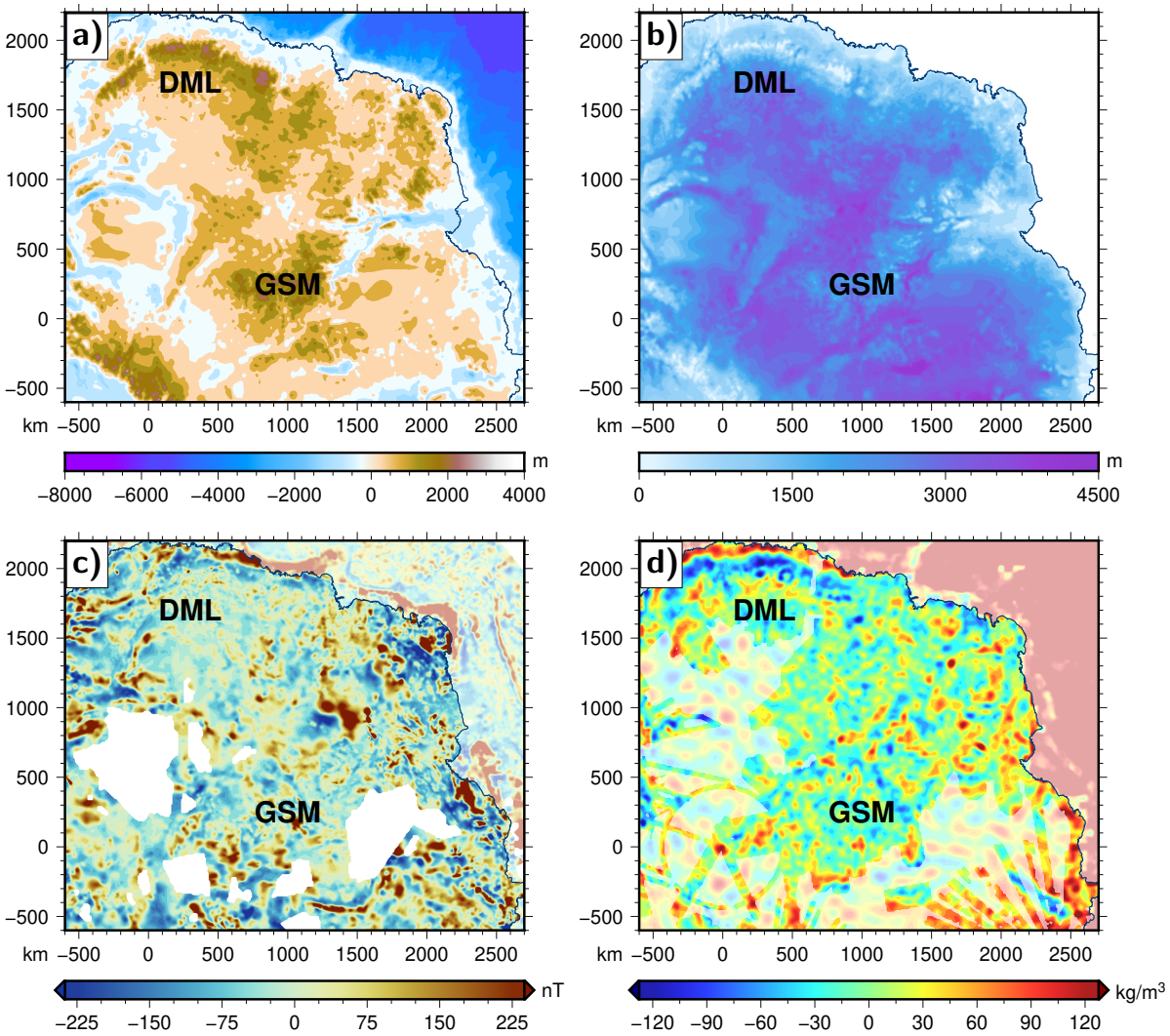

Figure 5.5.: Data and results for East Antarctica segment. (a) Bedrock topography, (b) ice thickness, (c) magnetic anomaly, (d) inverted density variation. Offshore values are dimmed in panels (c) and (d). Areas without airborne data are additionally dimmed in panel (d). DML=Dronning Maud Land; GSM=Gamburtsev Subglacial Mountains.

magnetic data in the periphery of the Gamburtsev Subglacial Mountains (e.g. Ferraccioli et al., 2011), which represent the most prominent topographic elevation in the area (Figure 5.5a). In direct comparison of the inverted density with the magnetic anomaly (Figure 5.5c), however, again no clear correlation is apparent. Even though one might manage to identify some lineaments that are present in both maps, there is no conclusive connection between the two.

As noted above and in Pappa et al. (2019b), the lithospheric density model was derived by modelling satellite gravity gradient data at satellite altitude (225 km), whereas the density inversion presented here is done with gravity data at 10 km height. The inverted density variations have short-wavelengths but may still have a significant effect on the gravity gradients at satellite height. In order to obtain a consistent model of the density distribution within the solid Earth, both the upper crustal and the lithospheric density model need to be iteratively harmonized.

The principle procedure is described in the following. In a first step, the gravity gradient effect of the inverted upper crustal density variations is computed at satellite altitude. If the amplitude of this effect is higher than the uncertainty of the gravity gradient data or a threshold value that accounts for the uncertainty of rock density estimation, the densities in the upper crust of the lithospheric model will be changed to compensate the effect. Subsequently, the lithospheric model needs to be recomputed in the original framework in order to ensure the consistency of all internal properties. The new lithospheric model can then be used to perform the upper crustal density inversion again. This can be done iteratively until the inverted density variations have wavelengths that are not detectable at satellite altitude any more.

We do not conduct the full iteration here but perform the first step, which is the forward-computation of the gravity gradient effect of the inverted densities. As an example, this is done for the EANT study area (Figure 5.5) at 225 km height in order to evaluate the amplitude (Figure 5.6). Offshore areas are ignored in this case. The effect of the inverted densities is notably large, and values are up to ± 0.3 E in the T_{UU} component. This is even beyond the residual misfit of ca. ± 0.2 E of the original lithospheric model (Pappa et al., 2019b, Figure 3.5). Moreover, the contours of the Gamburtsev Subglacial Mountains can be clearly identified in the T_{UU} component in Figure 5.6, showing negative values corresponding to mass deficits. The short-wavelength variations in Figure 5.5d, however, are not detectable at satellite altitude.

In consequence, the density variations derived in the inversion should be implemented into the lithospheric model, as described above. This is, however, a future task and not done at this point. An important aspect in the iterative procedure certainly is the isostatic state of the lithosphere, which was considered in the modelling process in Pappa et al. (2019b). If the densities within the lithosphere change, the isostatic elevation may not match the observed topography any longer. It remains to be tested if the changes in isostatic elevation due to the density modifications are

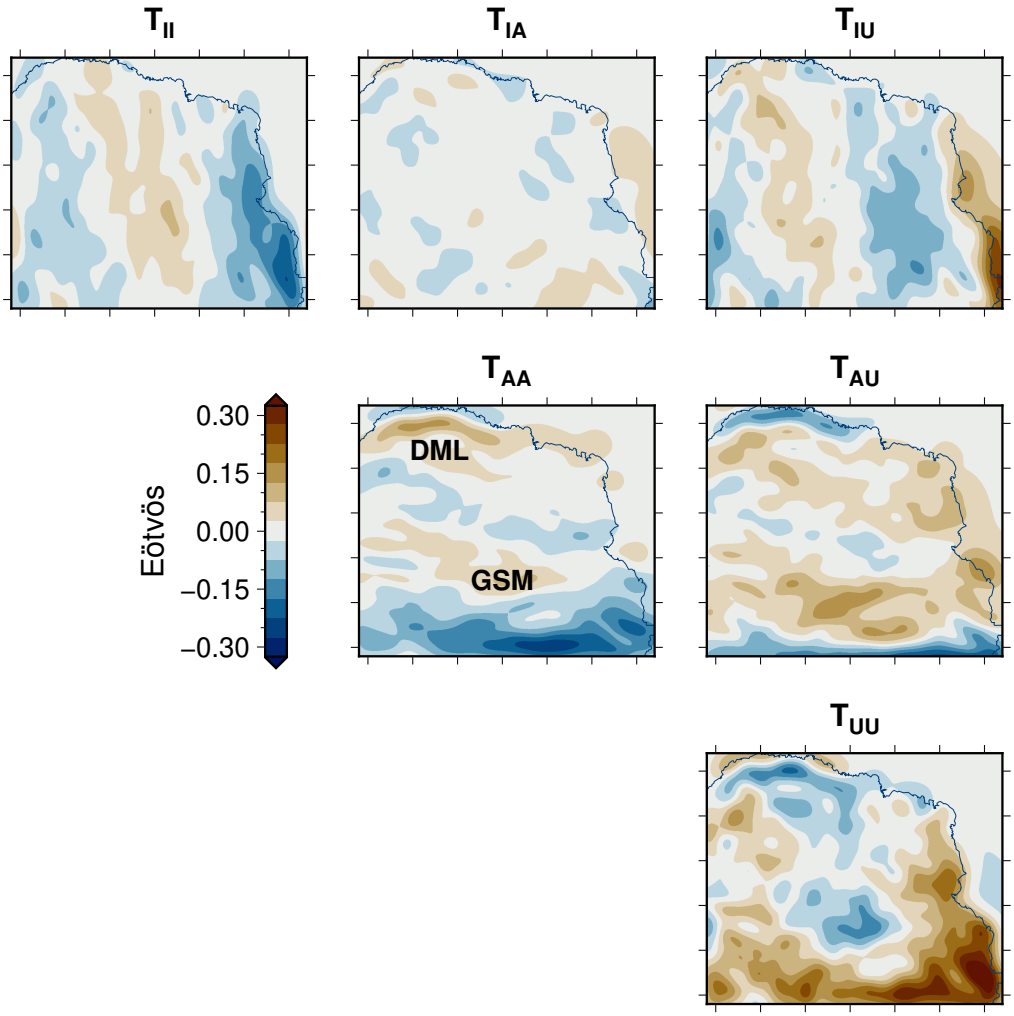

Figure 5.6.: Gravity gradient effect of the inverted density variations in East Antarctica (Figure 5.5d). The amplitude is larger than the residual of the original lithospheric model (±0.2 E, Figure 3.5), which demonstrates the potential of the presented method for iterative improvement of the model. DML=Dronning Maud Land; GSM=Gamburtsev Subglacial Mountains.

sufficiently small compared to the uncertainties of the bedrock topography and ice thickness estimates.

5.5. Conclusions

Continental-scale models of lithospheric densities in coarse resolutions can be used to compute gravity background signals of long wavelengths. By comparing such a gravity signal from the lithosphere with a high-resolution Bouguer gravity anomaly,

short-wavelength residuals can be obtained and inverted into near-surface density variations, which for their part can be interpreted from a geological point of view. Especially for poorly explored areas like Antarctica, this approach has the potential to give new insights in the upper crustal structure. In our study, we obtained a residual, short-wavelength gravity signal by using a separately established lithospheric density model and inverted the crustal densities down to a depth of 12 km.

The inversion was performed in three separate regions of the continent: Marie Byrd Land, Wilkes Land, and western East Antarctica. The resulting onshore density variations are generally in the range of ± 100 kg/m^3 and do not correlate with the input data, e.g. bedrock topography or ice thickness. Some similar patterns can be found in the magnetic anomaly, yet a coherent correlation with the inverted densities is not apparent, either. Positive inverted density values are obtained for the central West Antarctic Rift System, potentially indicating mafic crustal material. Strong density variations are computed for the area of the Terre Adélie Craton in Wilkes Land, but the interpretation is inconclusive due to the lack of correlation with other data. In East Antarctica, which is still geologically unfamiliar territory for large parts, the inverted density patterns cannot be linked to known or proposed geological structures directly. In spite of that, the results may be of use in multivariate analysis techniques (e.g. Stål et al., 2019) to map possible geological boundaries, which can indicate tectonic features like sub-glacial sedimentary basins and suture zones.

Evaluating the gravity gradient effect at satellite altitude, however, reveals long-wavelength residuals, for instance in the area of the Gamburtsev Subglacial Mountains. Given the strong signal of ± 0.3 E, which exceeds the residual misfit of the original model, the latter should be iteratively refined. In this process, attention should be given to the internal consistency of the lithospheric model, especially with respect to its isostatic state.

Chapter 6

Conclusions and Outlook

This thesis has reviewed and discussed the potential of satellite and airborne gravitational data to study the crust and upper mantle of Antarctica. Even though the coverage and the quality have improved significantly in recent years, additional constraints are needed for robust models. Seismological findings can help, but for their part suffer from a sparse station coverage. This fact is of particular importance for estimating the depth of the crust-mantle boundary, i.e. the Moho. As shown in the first paper (chapter 2), simplifying assumptions on the density contrast at this discontinuity lead to unsatisfying depth estimates for Antarctica in classical gravity inversion techniques. Crustal and upper mantle densities should instead be regarded as functions of temperature, pressure, and rock composition in a thermodynamically consistent modelling framework. In the case of the Wilkes Subglacial Basin–Transantarctic Mountains region, however, full lithospheric models in 2-D could not resolve conflicting Moho depth estimates from seismological studies.

In the second paper (chapter 3), a geophysical-petrological model of the Antarctic continent and its surrounding oceanic area has been established. This model represents the crust and upper mantel, and is computed by exploiting satellite gravity gradient data and their potential sensitivity to 3-D density variations. The results are generally consistent with the observed topography in terms of isostatic balance and seismic estimates regarding the Moho depth. Novel crustal thickness values are inferred in thus far poorly explored areas of East Antarctica and provide a basis for further interpretations on major tectonic features such as Gondwanan suture zones. Mantle viscosities are derived from the temperature field of the 3-D model in order to quantify the Earth's response to past changes in ice mass overburden. Small viscosity

values of ~10^{19} Pa·s are inferred for West Antarctica, implying potentially high uplift rates due to recent ice mass loss.

The large-scale lithospheric density model is checked against high-resolution gravity data at low altitude with the aim to invert the residual signal for density variations in the upper crust. The results are first jointly interpreted with topographic data and magnetic anomalies. Positive relative density values in the central West Antarctic Rift System are likely linked to mafic characteristics of the crust, which was originally modelled with properties typical for felsic continental rocks. Secondly, a section of East Antarctica, including Dronning Maud Land and the Gamburtsev Subglacial Mountains, is exemplarily used to demonstrate an iterative procedure for refining the original lithospheric model. The inverted upper crustal density variations cause a gravity gradient signal of significant strength at satellite altitude. Consequently, the lithospheric model may be improved by integrating the inverted density variations into its crustal part in order to reconcile it with both airborne gravity and satellite gravity gradient data at their respective altitudes.

In summary, the lithospheric model of Antarctica established in this thesis is a considerable step forward in resolving the conflicting findings from different geophysical methods by pursuing a comprehensive and self-consistent modelling approach. In this way, it was possible to compensate the data paucity in Antarctica to a large extent. Providing, therefore, a high level of robustness, further applications of the model in other fields of research are possible as shown for GIA modelling. However, limitations certainly exist. That is, for instance, the reliability of the temperature model at greater depth because thermal anomalies are not included in the modelled sublithospheric mantle. The model also ends at the 410-km discontinuity. Information about temperatures and viscosities of the deeper mantle, however, are as well essential for GIA modelling. Satellite gravity gradient data are not very sensitive to these depth ranges. Seismic tomography is better suited to detect spatial temperature variations in this case. Regarding the crustal part of the model, new insights into the tectonic structure of Antarctica may be gained through joint interpretation with other geophysical data, e.g. magnetic anomalies, and geological methods such as age dating and geochemical analyses. However, there is still room for improvement, as specified in the following:

Future tasks

- As mentioned above, the refinement of the lithospheric model with (short-wavelength) upper crustal density variations is the next logical step towards a more advanced and unified representation of the solid Earth structure of Antarctica.
- The crustal part of the model can be evaluated by forward modelling synthetic waveforms and subsequent comparison with existing waveform datasets (Emry, 2019). In this way, potential deficiencies of the model can be identified.
- Preliminary thermodynamic modelling results give reason to expect significant improvements from integrating local information about the upper mantle composition. Mantle xenolith samples, however, are extremely sparse in large regions of Antarctica. Compiling and integrating existing data, at least, would be an important element for a further enhancement of the lithospheric model.
- Since knowledge about the architecture of the Antarctic continent is crucial for reconstructing the geodynamic history of the Earth, the results presented in this thesis may help to better constrain Antarctica's links to its formerly adjacent continents in the Gondwanan framework.
- Estimates on mantle viscosities from this dissertation can be checked against results from regional and local GIA studies in Antarctica (e.g. in the Amundsen Sea Embayment, Barletta et al., 2018). Future works can possibly make use of the continental-scale temperature and density model to better separate the gravity signals from ice mass changes, vertical land motion, and mass redistribution in the deep subsurface.
- Likewise, the new regional 3-D model of the Antarctic lithosphere can be integrated into global Earth models for potential improvements at both global and continental scale. This is a major objective of the project *3D Earth – A Dynamic Living Planet*, funded by the European Space Agency (ESA).

As a final remark, I would like to express my hope that the work presented in this thesis can be of use to other scientists in their research projects related to Antarctica, and thus contribute to unveil the still hidden secrets of this "frozen continent".

References

A, G., Wahr, J., and Zhong, S. (2013). Computations of the viscoelastic response of a 3-D compressible Earth to surface loading: an application to Glacial Isostatic Adjustment in Antarctica and Canada. *Geophysical Journal International*, 192(2):557–572. doi: 10.1093/gji/ggs030.

Afonso, J. C., Fernàndez, M., Ranalli, G., Griffin, G., and Connolly, J. A. D. (2008). Integrated geophysical-petrological modeling of the lithosphere and sublithospheric upper mantle: Methodology and applications. *Geochemistry, Geophysics, Geosystems*, 9(5).

Afonso, J. C., Fullea, J., Griffin, W. L., Yang, Y., Jones, A. G., D. Connolly, J. A., and O'Reilly, S. Y. (2013). 3-D multiobservable probabilistic inversion for the compositional and thermal structure of the lithosphere and upper mantle. I: a priori petrological information and geophysical observables. *Journal of Geophysical Research: Solid Earth*, 118(5):2586–2617. doi: 10.1002/jgrb.50124.

Afonso, J. C., Moorkamp, M., and Fullea, J. (2016). Imaging the Lithosphere and Upper Mantle. In *Integrated Imaging of the Earth*, pages 191–218. American Geophysical Union (AGU). doi: 10.1002/9781118929063.ch10.

Afonso, J. C., Ranalli, G., and Fernàndez, M. (2007). Density structure and buoyancy of the oceanic lithosphere revisited. *Geophysical Research Letters*, 34(10). doi: 10.1029/2007GL029515.

Aitken, A. R. A., Betts, P. G., Young, D. A., Blankenship, D. D., Roberts, J. L., and Siegert, M. J. (2016). The Australo-Antarctic Columbia to Gondwana transition. *Gondwana Research*, 29(1):136–152. doi: 10.1016/j.gr.2014.10.019.

Aitken, A. R. A., Young, D. A., Ferraccioli, F., Betts, P. G., Greenbaum, J. S., Richter, T. G., Roberts, J. L., Blankenship, D. D., and Siegert, M. J. (2014). The subglacial geology of Wilkes Land, East Antarctica. *Geophysical Research Letters*, 41(7):2390–2400. doi: 10.1002/2014GL059405.

Amante, C. and Eakins, B. W. (2009). ETOPO1 1 arc-minute global relief model: procedures, data sources and analysis. *National Geophysical Data Center, NOAA*. doi: 10.7289/V5C8276M.

An, M., Wiens, D. A., and Zhao, Y. (2016). A frozen collision belt beneath ice: an overview of seismic studies around the Gamburtsev Subglacial Mountains, East Antarctica. *Advances in Polar Science*, 27(2):78–89. doi: 10.13679/j.advps.2016.2.00078.

An, M., Wiens, D. A., Zhao, Y., Feng, M., Nyblade, A., Kanao, M., Li, Y., Maggi, A., and Lévêque, J.-J. (2015a). Temperature, lithosphere-asthenosphere boundary, and heat flux beneath the Antarctic Plate inferred from seismic velocities. *Journal of Geophysical Research: Solid Earth*, 120(12):8720–8742. doi: 10.1002/2015JB011917.

An, M., Wiens, D. A., Zhao, Y., Feng, M., Nyblade, A. A., Kanao, M., Li, Y., Maggi, A., and Lévêque, J.-J. (2015b). S-velocity model and inferred Moho topography beneath the Antarctic Plate from Rayleigh waves. *Journal of Geophysical Research: Solid Earth*, 120(1):359–383. doi: 10.1002/2014JB011332.

Argus, D. F., Peltier, W. R., Drummond, R., and Moore, A. W. (2014). The Antarctica component of postglacial rebound model ICE-6g_c (VM5a) based on GPS positioning, exposure age dating of ice thicknesses, and relative sea level histories. *Geophysical Journal International*, 198(1):537–563. doi: 10.1093/gji/ggu140.

Armienti, P. and Perinelli, C. (2010). Cenozoic thermal evolution of lithospheric mantle in northern Victoria Land (Antarctica): Evidences from mantle xenoliths. *Tectonophysics*, 486(1):28–35. doi: 10.1016/j.tecto.2010.02.006.

Artemieva, I. M. (2009). The continental lithosphere: Reconciling thermal, seismic, and petrologic data. *Lithos*, 109(1–2):23–46. doi: 10.1016/j.lithos.2008.09.015.

Artemieva, I. M., Thybo, H., and Cherepanova, Y. (2019). Isopycnicity of cratonic mantle restricted to kimberlite provinces. *Earth and Planetary Science Letters*, 505:13–19. doi: 10.1016/j.epsl.2018.09.034.

Bamber, J. L., Ferraccioli, F., Joughin, I., Shepherd, T., Rippin, D. M., Siegert, M. J., and Vaughan, D. G. (2006). East Antarctic ice stream tributary underlain by major sedimentary basin. *Geology*, 34(1):33–36. doi: 10.1130/G22160.1.

Baranov, A. and Morelli, A. (2013). The Moho depth map of the Antarctica region. *Tectonophysics*, 609:299–313. doi: 10.1016/j.tecto.2012.12.023.

Baranov, A., Tenzer, R., and Bagherbandi, M. (2018). Combined Gravimetric–Seismic Crustal Model for Antarctica. *Surveys in Geophysics*, 39(1):23–56. doi: 10.1007/s10712-017-9423-5.

Barletta, V. R., Bevis, M., Smith, B. E., Wilson, T., Brown, A., Bordoni, A., Willis, M., Khan, S. A., Rovira-Navarro, M., Dalziel, I., Smalley, R., Kendrick, E., Konfal, S., Caccamise, D. J., Aster, R. C., Nyblade, A., and Wiens, D. A. (2018). Observed rapid bedrock uplift in Amundsen Sea Embayment promotes ice-sheet stability. *Science*, 360(6395):1335–1339. doi: 10.1126/science.aao1447.

Barnhoorn, A., van der Wal, W., Vermeersen, B. L. A., and Drury, M. R. (2011a). Lateral, radial, and temporal variations in upper mantle viscosity and rheology under Scandinavia. *Geochemistry, Geophysics, Geosystems*, 12(1). doi: 10.1029/2010GC003290.

Barnhoorn, A., Wal, W. v. d., and Drury, M. R. (2011b). Upper mantle viscosity and lithospheric thickness under Iceland. *Journal of Geodynamics*, 52(3):260–270. doi: 10.1016/j.jog.2011.01.002.

Barzaghi, R., Betti, B., Carrion, D., Gentile, G., Maseroli, R., and Sacerdote, F. (2014). Orthometric correction and normal heights for Italian levelling network: a case study. *Applied Geomatics*, 6(1):17–25. doi: 10.1007/s12518-013-0121-9.

Betts, P. G., Armit, R. J., Stewart, J., Aitken, A. R. A., Ailleres, L., Donchak, P., Hutton, L., Withnall, I., and Giles, D. (2016). Australia and Nuna. *Geological Society, London, Special Publications*, 424(1):47–81. doi: 10.1144/SP424.2.

Beyer, E. E., Griffin, W. L., and O'Reilly, S. Y. (2006). Transformation of Archaean Lithospheric Mantle by Refertilization: Evidence from Exposed Peridotites in the Western Gneiss Region, Norway. *Journal of Petrology*, 47(8):1611–1636. doi: 10.1093/petrology/egl022.

Bingham, R. G., Ferraccioli, F., King, E. C., Larter, R. D., Pritchard, H. D., Smith, A. M., and Vaughan, D. G. (2012). Inland thinning of West Antarctic Ice Sheet steered along subglacial rifts. *Nature*, 487:468.

Blakely, R. J. (1995). *Potential theory in gravity and magnetic applications.* Cambridge University Press.

Block, A. E., Bell, R. E., and Studinger, M. (2009). Antarctic crustal thickness from satellite gravity: Implications for the Transantarctic and Gamburtsev Subglacial Mountains. *Earth and Planetary Science Letters*, 288(1–2):194–203. doi: 10.1016/j.epsl.2009.09.022.

Boger, S. D. (2011). Antarctica – Before and after Gondwana. *Gondwana Research*, 19(2):335–371. doi: 10.1016/j.gr.2010.09.003.

Borg, S. G., Depaolo, D. J., and Smith, B. M. (1990). Isotopic structure and tectonics of the central Transantarctic mountains. *Journal of Geophysical Research: Solid Earth*, 95(B5):6647–6667. doi: 10.1029/JB095iB05p06647.

Bouman, J., Ebbing, J., and Fuchs, M. (2013). Reference frame transformation of satellite gravity gradients and topographic mass reduction. *Journal of Geophysical Research: Solid Earth*, 118(2):759–774. doi: 10.1029/2012JB009747.

Bouman, J., Ebbing, J., Fuchs, M., Sebera, J., Lieb, V., Szwillus, W., Haagmans, R., and Novak, P. (2016). Satellite gravity gradient grids for geophysics. *Scientific Reports*, 6:21050.

Bouman, J., Ebbing, J., Meekes, S., Fattah, R. A., Fuchs, M., Gradmann, S., Haagmans, R., Lieb, V., Schmidt, M., Dettmering, D., and Bosch, W. (2015). GOCE gravity gradient data for lithospheric modeling. *International Journal of Applied Earth Observation and Geoinformation*, 35, Part A:16–30. doi: 10.1016/j.jag.2013.11.001.

Bradley, S. L., Hindmarsh, R. C. A., Whitehouse, P. L., Bentley, M. J., and King, M. A. (2015). Low post-glacial rebound rates in the Weddell Sea due to Late Holocene ice-sheet readvance. *Earth and Planetary Science Letters*, 413:79–89. doi: 10.1016/j.epsl.2014.12.039.

Braitenberg, C., Pettenati, F., and Zadro, M. (1997). Spectral and classical methods in the evaluation of Moho undulations from gravity data: The NE Italian Alps and isostasy. *Journal of Geodynamics*, 23(1):5–22. doi: 10.1016/S0264-3707(96)00024-5.

Brockmann, J. M., Zehentner, N., Höck, E., Pail, R., Loth, I., Mayer-Gürr, T., and Schuh, W.-D. (2014). EGM_tim_rl05: An independent geoid with centimeter accuracy purely based on the GOCE mission. *Geophysical Research Letters*, 41(22):8089–8099. doi: 10.1002/2014GL061904.

Burton-Johnson, A., Black, M., Fretwell, P. T., and Kaluza-Gilbert, J. (2016). An automated methodology for differentiating rock from snow, clouds and sea in Antarctica from Landsat 8 imagery: \hack\breaka new rock outcrop map and area estimation for the \hack\breakentire Antarctic continent. *The Cryosphere*, 10(4):1665–1677. doi: 10.5194/tc-10-1665-2016.

Cammarano, F., Goes, S., Vacher, P., and Giardini, D. (2003). Inferring upper-mantle temperatures from seismic velocities. *Physics of the Earth and Planetary Interiors*, 138(3):197–222. doi: 10.1016/S0031-9201(03)00156-0.

Cawood, P. A. and Buchan, C. (2007). Linking accretionary orogenesis with supercontinent assembly. *Earth-Science Reviews*, 82(3):217–256. doi: 10.1016/j.earscirev.2007.03.003.

Chappell, A. and Kusznir, N. (2008). An algorithm to calculate the gravity anomaly of sedimentary basins with exponential density-depth relationships. *Geophysical Prospecting*, 56(2):249–258. doi: 10.1111/j.1365-2478.2007.00674.x.

Chaput, J., Aster, R. C., Huerta, A., Sun, X., Lloyd, A., Wiens, D., Nyblade, A., Anandakrishnan, S., Winberry, J. P., and Wilson, T. (2014). The crustal thickness of West Antarctica. *Journal of Geophysical Research: Solid Earth*, 119(1):378–395. doi: 10.1002/2013JB010642.

Chiappini, M., Ferraccioli, F., Bozzo, E., and Damaske, D. (2002). Regional compilation and analysis of aeromagnetic anomalies for the Transantarctic Mountains–Ross Sea sector of the Antarctic. *Tectonophysics*, 347(1):121–137. doi: 10.1016/S0040-1951(01)00241-4.

Chisenga, C., Yan, J., and Yan, P. (2019). A crustal thickness model of Antarctica calculated in spherical approximation from satellite gravimetric data. *Geophysical Journal International*, 218(1):388–400. doi: 10.1093/gji/ggz154.

Christensen, N. I. and Mooney, W. D. (1995). Seismic velocity structure and composition of the continental crust: A global view. *Journal of Geophysical Research: Solid Earth*, 100(B6):9761–9788. doi: 10.1029/95JB00259.

Collins, A. S. and Pisarevsky, S. A. (2005). Amalgamating eastern Gondwana: The evolution of the Circum-Indian Orogens. *Earth-Science Reviews*, 71(3–4):229–270. doi: 10.1016/j.earscirev.2005.02.004.

Connolly, J. A. D. (2005). Computation of phase equilibria by linear programming: a tool for geodynamic modeling and its application to subduction zone decarbonation. *Earth and Planetary Science Letters*, 236(1):524–541.

Cordell, L., Zorin, Y. A., and Keller, G. R. (1991). The decompensative gravity anomaly and deep structure of the region of the Rio Grande Rift. *Journal of Geophysical Research: Solid Earth*, 96(B4):6557–6568. doi: 10.1029/91JB00008.

Cox, S. E., Thomson, S. N., Reiners, P. W., Hemming, S. R., and van de Flierdt, T. (2010). Extremely low long-term erosion rates around the Gamburtsev Mountains in interior East Antarctica. *Geophysical Research Letters*, 37(22). doi: 10.1029/2010GL045106.

Craddock, J. P., Schmitz, M. D., Crowley, J. L., Larocque, J., Pankhurst, R. J., Juda, N., Konstantinou, A., and Storey, B. (2017). Precise U-Pb zircon ages and geochemistry of Jurassic granites, Ellsworth-Whitmore terrane, central Antarctica. *GSA Bulletin*, 129(1-2):118–136. doi: 10.1130/B31485.1.

Creyts, T. T., Ferraccioli, F., Bell, R. E., Wolovick, M., Corr, H., Rose, K. C., Frearson, N., Damaske, D., Jordan, T., Braaten, D., and Finn, C. (2014). Freezing of ridges and water networks preserves the Gamburtsev Subglacial Mountains for millions of years. *Geophysical Research Letters*, 41(22):8114–8122. doi: 10.1002/2014GL061491.

Curtis, S. and Thiel, S. (2019). Identifying lithospheric boundaries using magnetotellurics and Nd isotope geochemistry: An example from the Gawler Craton, Australia. *Precambrian Research*, 320:403–423. doi: 10.1016/j.precamres.2018.11.013.

Dalziel, I. W. D. and Elliot, D. H. (1982). West Antarctica: Problem child of Gondwanaland. *Tectonics*, 1(1):3–19. doi: 10.1029/TC001i001p00003.

Dziewonski, A. M. and Anderson, D. L. (1981). Preliminary reference Earth model. *Physics of the Earth and Planetary Interiors*, 25(4):297–356. doi: 10.1016/0031-9201(81)90046-7.

Eaton, D. W., Darbyshire, F., Evans, R. L., Grütter, H., Jones, A. G., and Yuan, X. (2009). The elusive lithosphere–asthenosphere boundary (LAB) beneath cratons. *Lithos*, 109(1):1–22.

Eaton, D. W. and Perry, H. K. C. (2013). Ephemeral isopycnicity of cratonic mantle keels. *Nature Geoscience*, 6:967.

Ebbing, J., Haas, P., Ferraccioli, F., Pappa, F., Szwillus, W., and Bouman, J. (2018). Earth tectonics as seen by GOCE - Enhanced satellite gravity gradient imaging. *Scientific Reports*, 8(1):16356. doi: 10.1038/s41598-018-34733-9.

Elliot, D. H., Fanning, C. M., and Hulett, S. R. W. (2015). Age provinces in the Antarctic craton: Evidence from detrital zircons in Permian strata from the Beardmore Glacier region, Antarctica. *Gondwana Research*, 28(1):152–164. doi: 10.1016/j.gr.2014.03.013.

Emry, E. (2019). Quantitative assessment of Antarctic crustal models using numerical wave simulations. Presentation at XIII International Symposium on Antarctic Earth Sciences (ISAES 2019), Incheon, Republic of Korea.

Emry, E. L., Nyblade, A. A., Julià, J., Anandakrishnan, S., Aster, R. C., Wiens, D. A., Huerta, A. D., and Wilson, T. J. (2015). The mantle transition zone beneath West Antarctica: Seismic evidence for hydration and thermal upwellings. *Geochemistry, Geophysics, Geosystems*, 16(1):40–58. doi: 10.1002/2014GC005588.

Feng, M., An, M., An, C., Shi, G., Zhao, Y., Li, Y., and Wiens, D. (2014). Crustal thicknesses along the traverse from Zhongshan to Dome A in Eastern Antarctica. *Chinese Journal of Polar Research*, 26:177–185. doi: 10.13679/j.jdyj.2014.2.177.

Ferraccioli, F., Armadillo, E., Jordan, T., Bozzo, E., and Corr, H. (2009a). Aeromagnetic exploration over the East Antarctic Ice Sheet: A new view of the Wilkes Subglacial Basin. *Tectonophysics*, 478(1–2):62–77. doi: 10.1016/j.tecto.2009.03.013.

Ferraccioli, F., Armadillo, E., Zunino, A., Bozzo, E., Rocchi, S., and Armienti, P. (2009b). Magmatic and tectonic patterns over the Northern Victoria Land sector of the Transantarctic Mountains from new aeromagnetic imaging. *Tectonophysics*, 478(1):43–61. doi:

10.1016/j.tecto.2008.11.028.

Ferraccioli, F. and Bozzo, E. (2003). Cenozoic strike-slip faulting from the eastern margin of the Wilkes Subglacial Basin to the western margin of the Ross Sea Rift: an aeromagnetic connection. *Geological Society, London, Special Publications*, 210(1):109–133. doi: 10.1144/GSL.SP.2003.210.01.07.

Ferraccioli, F., Bozzo, E., and Capponi, G. (2002). Aeromagnetic and gravity anomaly constraints for an early Paleozoic subduction system of Victoria Land, Antarctica. *Geophysical Research Letters*, 29(10). doi: 10.1029/2001GL014138.

Ferraccioli, F., Coren, F., Bozzo, E., Zanolla, C., Gandolfi, S., Tabacco, I., and Frezzotti, M. (2001). Rifted(?) crust at the East Antarctic Craton margin: gravity and magnetic interpretation along a traverse across the Wilkes Subglacial Basin region. *Earth and Planetary Science Letters*, 192(3):407–421. doi: 10.1016/S0012-821X(01)00459-9.

Ferraccioli, F., Finn, C. A., Jordan, T. A., Bell, R. E., Anderson, L. M., and Damaske, D. (2011). East Antarctic rifting triggers uplift of the Gamburtsev Mountains. *Nature*, 479(7373):388–392. doi: 10.1038/nature10566.

Filina, I. Y., Blankenship, D. D., Thoma, M., Lukin, V. V., Masolov, V. N., and Sen, M. K. (2008). New 3d bathymetry and sediment distribution in Lake Vostok: Implication for pre-glacial origin and numerical modeling of the internal processes within the lake. *Earth and Planetary Science Letters*, 276(1):106–114. doi: 10.1016/j.epsl.2008.09.012.

Finn, C., Moore, D., Damaske, D., and Mackey, T. (1999). Aeromagnetic legacy of early Paleozoic subduction along the Pacific margin of Gondwana. *Geology*, 27(12):1087–1090. doi: 10.1130/0091-7613(1999)027<1087:ALOEPS>2.3.CO;2.

Fitzgerald, P. (2002). Tectonics and landscape evolution of the Antarctic plate since the breakup of Gondwana, with an emphasis on the West Antarctic Rift System and the Transantarctic Mountains. *Royal Society of New Zealand Bulletin*, 35:453–469.

Fitzsimons, I. C. W. (2000). A review of tectonic events in the East Antarctic Shield and their implications for Gondwana and earlier supercontinents. *Journal of African Earth Sciences*, 31(1):3–23. doi: 10.1016/S0899-5362(00)00069-5.

Forsberg, R. (2015). GOCE and Antarctica. In *5th International GOCE User Workshop*, volume 728 of *ESA Special Publication*, page 3.

Forsberg, R., Olesen, A., Yildiz, H., and Tscherning, C. C. (2011). Polar Gravity Fields from GOCE and Airborne Gravity. In *4th International GOCE User Workshop*, volume 696 of *ESA Special Publication*, page 8.

Forsberg, R., Olesen, A. V., Ferraccioli, F., Jordan, T. A., Matsuoka, K., Zakrajsek, A., Ghidella, M., and Greenbaum, J. S. (2018). Exploring the Recovery Lakes region and interior Dronning Maud Land, East Antarctica, with airborne gravity, magnetic and radar measurements. *Geological Society, London, Special Publications*, 461(1):23–34. doi: 10.1144/SP461.17.

Fox Maule, C., Purucker, M. E., Olsen, N., and Mosegaard, K. (2005). Heat Flux Anomalies in Antarctica Revealed by Satellite Magnetic Data. *Science*, 309(5733):464–467. doi: 10.1126/science.1106888.

Frederick, B. C., Young, D. A., Blankenship, D. D., Richter, T. G., Kempf, S. D., Ferraccioli, F., and Siegert, M. J. (2016). Distribution of subglacial sediments across the Wilkes Subglacial Basin, East Antarctica. *Journal of Geophysical Research: Earth Surface*, 121(4):790–813. doi: 10.1002/2015JF003760.

Frederikse, T., Landerer, F. W., and Caron, L. (2019). The imprints of contemporary mass redistribution on local sea level and vertical land motion observations. *Solid Earth*, 10(6):1971–1987. doi: 10.5194/se-10-1971-2019.

Fretwell, P. (2019). Bedmap3: the vision for a new ice thickness and subglacial topography dataset. Presentation at XIII International Symposium on Antarctic Earth Sciences (ISAES 2019), Incheon, Republic of Korea.

Fretwell, P., Pritchard, H. D., Vaughan, D. G., Bamber, J. L., Barrand, N. E., Bell, R., Bianchi, C., Bingham, R. G., Blankenship, D. D., Casassa, G., Catania, G., Callens, D., Conway, H., Cook, A. J., Corr, H. F. J., Damaske, D., Damm, V., Ferraccioli, F., Forsberg, R., Fujita, S., Gim, Y., Gogineni, P., Griggs, J. A., Hindmarsh, R. C. A., Holmlund, P., Holt, J. W., Jacobel, R. W., Jenkins, A., Jokat, W., Jordan, T., King, E. C., Kohler, J., Krabill, W., Riger-Kusk, M., Langley, K. A., Leitchenkov, G., Leuschen, C., Luyendyk, B. P., Matsuoka, K., Mouginot, J., Nitsche, F. O., Nogi, Y., Nost, O. A., Popov, S. V., Rignot, E., Rippin, D. M., Rivera, A., Roberts, J., Ross, N., Siegert, M. J., Smith, A. M., Steinhage, D., Studinger, M., Sun, B., Tinto, B. K., Welch, B. C., Wilson, D., Young, D. A., Xiangbin, C., and Zirizzotti, A. (2013). Bedmap2: improved ice bed, surface and thickness datasets for Antarctica. *The Cryosphere*, 7(1):375–393. doi: 10.5194/tc-7-375-2013.

Fullea, J., Afonso, J. C., Connolly, J. A. D., Fernàndez, M., Garcìa-Castellanos, D., and Zeyen, H. (2009). LitMod3d: An interactive 3-D software to model the thermal, compositional, density, rheological and seismological structure of the lithosphere and sublithospheric upper mantle. *Geochemistry, Geophysics, Geosystems*, 10(8).

Fullea, J., Lebedev, S., Agius, M. R., Jones, A. G., and Afonso, J. C. (2012). Lithospheric structure in the Baikal–central Mongolia region from integrated geophysical-petrological inversion of surface-wave data and topographic elevation. *Geochemistry, Geophysics, Geosystems*,

13(8). doi: 10.1029/2012GC004138.

Fullea, J., Rodríguez-González, J., Charco, M., Martinec, Z., Negredo, A., and Villaseñor, A. (2015). Perturbing effects of sub-lithospheric mass anomalies in GOCE gravity gradient and other gravity data modelling: Application to the Atlantic-Mediterranean transition zone. *International Journal of Applied Earth Observation and Geoinformation*, 35(Part A):54–69. doi: 10.1016/j.jag.2014.02.003.

Garcia-Castellanos, D. (2002). Interplay between lithospheric flexure and river transport in foreland basins. *Basin Research*, 14(2):89–104. doi: 10.1046/j.1365-2117.2002.00174.x.

Golynsky, A., Chiappini, M., Damaske, D., Ferraccioli, F., Ferris, J., Finn, C., Ghidella, M., Isihara, T., Johnson, A., Kim, H., and others (2001). ADMAP – Magnetic Anomaly Map of the Antarctic.

Golynsky, A., Chiappini, M., Damaske, D., Ferraccioli, F., Finn, C. A., Ishihara, T., Kim, H. R., Kovacs, L., Masolov, V. N., Morris, P., and von Frese, R. (2006). ADMAP – A Digital Magnetic Anomaly Map of the Antarctic. In Fütterer, D. K., Damaske, D., Kleinschmidt, G., Miller, H., and Tessensohn, F., editors, *Antarctica: Contributions to Global Earth Sciences*, pages 109–116. Springer, Berlin, Heidelberg. doi: 10.1007/3-540-32934-X_12.

Golynsky, A., Ferraccioli, F., Jordan, T. A., Damaske, D., Blankenship, D., Holt, J., Young, D. A., Ivanov, S., Kiselev, A. V., Masolov, V. N., Jokat, W., Mieth, M., Gohl, K., Eagles, G., Bell, R. E., Golynsky, D., Armadillo, E., Bozzo, E., Caneva, G., Forsberg, R., Aitken, A., Finn, C., Nogi, Y., Ghidella, M., Frese, R. v., Kim, H. R., and Hong, J. (2015). ADMAP-2: A New International Magnetic Anomaly Compilation Project to Aid Antarctic Geosciences. In *XII International symposium on Antarctic Earth Sciences*.

Golynsky, A. V., Ferraccioli, F., Hong, J. K., Golynsky, D. A., von Frese, R. R. B., Young, D. A., Blankenship, D. D., Holt, J. W., Ivanov, S. V., Kiselev, A. V., Masolov, V. N., Eagles, G., Gohl, K., Jokat, W., Damaske, D., Finn, C., Aitken, A., Bell, R. E., Armadillo, E., Jordan, T. A., Greenbaum, J. S., Bozzo, E., Caneva, G., Forsberg, R., Ghidella, M., Galindo-Zaldivar, J., Bohoyo, F., Martos, Y. M., Nogi, Y., Quartini, E., Kim, H. R., and Roberts, J. L. (2018). New Magnetic Anomaly Map of the Antarctic. *Geophysical Research Letters*, 45(13):6437–6449. doi: 10.1029/2018GL078153.

Goodge, J. W. and Fanning, C. M. (2016). Mesoarchean and Paleoproterozoic history of the Nimrod Complex, central Transantarctic Mountains, Antarctica: Stratigraphic revisions and relation to the Mawson Continent in East Gondwana. *Precambrian Research*, 285:242–271. doi: 10.1016/j.precamres.2016.09.001.

Goodge, J. W., Fanning, C. M., Brecke, D. M., Licht, K. J., and Palmer, E. F. (2010). Continuation of the Laurentian Grenville Province across the Ross Sea Margin of East Antarctica. *The Journal of Geology*, 118(6):601–619. doi: 10.1086/656385.

Goodge, J. W., Fanning, C. M., Fisher, C. M., and Vervoort, J. D. (2017). Proterozoic crustal evolution of central East Antarctica: Age and isotopic evidence from glacial igneous clasts, and links with Australia and Laurentia. *Precambrian Research*, 299:151–176. doi: 10.1016/j.precamres.2017.07.026.

Goodge, J. W., Fanning, C. M., Norman, M. D., and Bennett, V. C. (2012). Temporal, Isotopic and Spatial Relations of Early Paleozoic Gondwana-Margin Arc Magmatism, Central Transantarctic Mountains, Antarctica. *Journal of Petrology*, 53(10):2027–2065. doi: 10.1093/petrology/egs043.

Goodge, J. W. and Finn, C. A. (2010). Glimpses of East Antarctica: Aeromagnetic and satellite magnetic view from the central Transantarctic Mountains of East Antarctica. *Journal of Geophysical Research: Solid Earth*, 115(B9). doi: 10.1029/2009JB006890.

Graw, J. H. and Hansen, S. E. (2017). Upper mantle seismic anisotropy beneath the Northern Transantarctic Mountains, Antarctica from PKS, SKS, and SKKS splitting analysis. *Geochemistry, Geophysics, Geosystems*, 18(2):544–557. doi: 10.1002/2016GC006729.

Haeger, C. and Kaban, M. K. (2019). Decompensative Gravity Anomalies Reveal the Structure of the Upper Crust of Antarctica. *Pure and Applied Geophysics*, 176(10):4401–4414. doi: 10.1007/s00024-019-02212-5.

Haeger, C., Kaban, M. K., Tesauro, M., Petrunin, A. G., and Mooney, W. D. (2019). 3-D Density, Thermal, and Compositional Model of the Antarctic Lithosphere and Implications for Its Evolution. *Geochemistry, Geophysics, Geosystems*, 20(2):688–707. doi: 10.1029/2018GC008033.

Hansen, S. E., Graw, J. H., Kenyon, L. M., Nyblade, A. A., Wiens, D. A., Aster, R. C., Huerta, A. D., Anandakrishnan, S., and Wilson, T. (2014). Imaging the Antarctic mantle using adaptively parameterized P-wave tomography: Evidence for heterogeneous structure beneath West Antarctica. *Earth and Planetary Science Letters*, 408:66–78. doi: 10.1016/j.epsl.2014.09.043.

Hansen, S. E., Julià, J., Nyblade, A. A., Pyle, M. L., Wiens, D. A., and Anandakrishnan, S. (2009). Using S wave receiver functions to estimate crustal structure beneath ice sheets: An application to the Transantarctic Mountains and East Antarctic craton. *Geochemistry, Geophysics, Geosystems*, 10(8). doi: 10.1029/2009GC002576.

Hansen, S. E., Kenyon, L. M., Graw, J. H., Park, Y., and Nyblade, A. A. (2016). Crustal structure beneath the Northern Transantarctic Mountains and Wilkes Subglacial Basin: Implications for tectonic origins. *Journal of Geophysical Research: Solid Earth*, 121(2):812–825. doi: 10.1002/2015JB012325.

Hansen, S. E., Nyblade, A. A., Heeszel, D. S., Wiens, D. A., Shore, P., and Kanao, M. (2010). Crustal structure of the Gamburtsev Mountains, East Antarctica, from S-wave receiver functions and Rayleigh wave phase velocities. *Earth and Planetary Science Letters*, 300(3–4):395–401. doi: 10.1016/j.epsl.2010.10.022.

Harley, S. L., Fitzsimons, I. C. W., and Zhao, Y. (2013). Antarctica and supercontinent evolution: historical perspectives, recent advances and unresolved issues. *Geological Society, London, Special Publications*, 383(1):1–34. doi: 10.1144/SP383.9.

Heeszel, D. S., Wiens, D. A., Anandakrishnan, S., Aster, R. C., Dalziel, I. W. D., Huerta, A. D., Nyblade, A. A., Wilson, T. J., and Winberry, J. P. (2016). Upper mantle structure of central and West Antarctica from array analysis of Rayleigh wave phase velocities. *Journal of Geophysical Research: Solid Earth*, 121(3):1758–1775. doi: 10.1002/2015JB012616.

Heeszel, D. S., Wiens, D. A., Nyblade, A. A., Hansen, S. E., Kanao, M., An, M., and Zhao, Y. (2013). Rayleigh wave constraints on the structure and tectonic history of the Gamburtsev Subglacial Mountains, East Antarctica. *Journal of Geophysical Research: Solid Earth*, 118(5):2138–2153. doi: 10.1002/jgrb.50171.

Hemingway, D. J. and Matsuyama, I. (2017). Isostatic equilibrium in spherical coordinates and implications for crustal thickness on the Moon, Mars, Enceladus, and elsewhere. *Geophysical Research Letters*, 44(15):7695–7705. doi: 10.1002/2017GL073334.

Hirschmann, M. M. (2006). WATER, MELTING, AND THE DEEP EARTH H2o CYCLE. *Annual Review of Earth and Planetary Sciences*, 34(1):629–653. doi: 10.1146/annurev.earth.34.031405.125211.

Hirt, C., Kuhn, M., Featherstone, W. E., and Göttl, F. (2012). Topographic/isostatic evaluation of new-generation GOCE gravity field models. *Journal of Geophysical Research: Solid Earth*, 117(B5). doi: 10.1029/2011JB008878.

Hirth, G. and Kohlstedt, D. (2003). Rheology of the Upper Mantle and the Mantle Wedge: A View from the Experimentalists. In *Inside the Subduction Factory*, pages 83–105. American Geophysical Union (AGU). doi: 10.1029/138GM06.

Hofmeister, A. M. (1999). Mantle Values of Thermal Conductivity and the Geotherm from Phonon Lifetimes. *Science*, 283(5408):1699–1706. doi: 10.1126/science.283.5408.1699.

Holzrichter, N. and Ebbing, J. (2016). A regional background model for the Arabian Peninsula from modeling satellite gravity gradients and their invariants. *Tectonophysics*, 692:86–94. doi: 10.1016/j.tecto.2016.06.002.

Irifune, T. and Ringwood, A. E. (1987). Phase transformations in a harzburgite composition to 26 GPa: implications for dynamical behaviour of the subducting slab. *Earth and Planetary Science Letters*, 86(2):365–376. doi: 10.1016/0012-821X(87)90233-0.

Isanina, E. V., Krupnova, N. A., Popov, S. V., Masolov, V. N., and Lukin, V. V. (2009). Deep structure of the Vostok Basin, East Antarctica as deduced from seismological observations. *Geotectonics*, 43(3):221–225. doi: 10.1134/S0016852109030042.

Ivins, E. R. and Sammis, C. G. (1995). On lateral viscosity contrast in the mantle and the rheology of low-frequency geodynamics. *Geophysical Journal International*, 123(2):305–322. doi: 10.1111/j.1365-246X.1995.tb06856.x.

Ji, S. and Zhao, P. (1994). Layered rheological structure of subducting oceanic lithosphere. *Earth and Planetary Science Letters*, 124(1):75–94. doi: 10.1016/0012-821X(94)00085-9.

Jokat, W. and Herter, U. (2016). Jurassic failed rift system below the Filchner-Ronne-Shelf, Antarctica: New evidence from geophysical data. *Tectonophysics*, 688:65–83. doi: 10.1016/j.tecto.2016.09.018.

Jones, A. G., Afonso, J. C., Fullea, J., and Salajegheh, F. (2014). The lithosphere–asthenosphere system beneath Ireland from integrated geophysical–petrological modeling – I: Observations, 1d and 2d hypothesis testing and modeling. *Lithos*, 189:28–48. doi: 10.1016/j.lithos.2013.10.033.

Jordan, T., Ferraccioli, F., Corr, H., Forsberg, R., Matsuoka, K., Olesen, A., Seddon, S., and Casal, T. (2017a). First complete regional view of the Pensacola-Pole Basin from PolarGAP radar data. In *EGU General Assembly Conference Abstracts*, volume 19 of *EGU General Assembly Conference Abstracts*, page 15902.

Jordan, T. A., Ferraccioli, F., Armadillo, E., and Bozzo, E. (2013). Crustal architecture of the Wilkes Subglacial Basin in East Antarctica, as revealed from airborne gravity data. *Tectonophysics*, 585:196–206. doi: 10.1016/j.tecto.2012.06.041.

Jordan, T. A., Ferraccioli, F., and Leat, P. T. (2017b). New geophysical compilations link crustal block motion to Jurassic extension and strike-slip faulting in the Weddell Sea Rift System of West Antarctica. *Gondwana Research*, 42:29–48. doi: 10.1016/j.gr.2016.09.009.

Jordan, T. H. (1988). Structure and Formation of the Continental Tectosphere. *Journal of Petrology*, Special_Volume(1):11–37. doi: 10.1093/petrology/Special_Volume.1.11.

Kaban, K. M., Schwintzer, P., and Reigber, C. (2004). A new isostatic model of the lithosphere and gravity field. *Journal of Geodesy*, 78(6):368–385. doi: 10.1007/s00190-004-0401-6.

Kaban, M. K., El Khrepy, S., and Al-Arifi, N. (2017). Importance of the Decompensative Correction of the Gravity Field for Study of the Upper Crust: Application to the Arabian Plate and Surroundings. *Pure and Applied Geophysics*, 174(1):349–358. doi: 10.1007/s00024-016-1382-0.

Kaban, M. K., Schwintzer, P., Artemieva, I. M., and Mooney, W. D. (2003). Density of the continental roots: compositional and thermal contributions. *Earth and Planetary Science Letters*, 209(1–2):53–69. doi: 10.1016/S0012-821X(03)00072-4.

Kaban, M. K., Tesauro, M., and Cloetingh, S. A. P. L. (2010). An integrated gravity model for Europe's crust and upper mantle. *Earth and Planetary Science Letters*, 296(3):195–209.

Kanao, M., Wiens, D., Tanaka, S., Nyblade, A., Toyokuni, G., Shore, P., Tsuboi, S., Heeszel, D., Usui, Y., and Parker, T. (2014). Broadband seismic deployments in East Antarctica: IPY contribution to monitoring the Earths interiors. *Annals of Geophysics*, 57(3). doi: 10.4401/ag-6379.

Kaufmann, G., Wu, P., and Ivins, E. R. (2005). Lateral viscosity variations beneath Antarctica and their implications on regional rebound motions and seismotectonics. *Journal of Geodynamics*, 39(2):165 – 181. doi: doi.org/10.1016/j.jog.2004.08.009.

Kennett, B. L. N., Salmon, M., Saygin, E., and Group, A. W. (2011). AusMoho: the variation of Moho depth in Australia. *Geophysical Journal International*, 187(2):946–958. doi: 10.1111/j.1365-246X.2011.05194.x.

Kennett, B. L. N., Saygin, E., and Salmon, M. (2012). Australian Seismological Reference Model (AuSREM): crustal component. *Geophysical Journal International*, 192(1):190–206. doi: 10.1093/gji/ggs004.

King, M. A., Bingham, R. J., Moore, P., Whitehouse, P. L., Bentley, M. J., and Milne, G. A. (2012). Lower satellite-gravimetry estimates of Antarctic sea-level contribution. *Nature*, 491(7425):586–589. doi: 10.1038/nature11621.

Lamarque, G., Barruol, G., Fontaine, F. R., Bascou, J., and Ménot, R.-P. (2015). Crustal and mantle structure beneath the Terre Adélie Craton, East Antarctica: insights from receiver function and seismic anisotropy measurements. *Geophysical Journal International*, 200(2):807–821. doi: 10.1093/gji/ggu430.

Lawrence, J. F., Wiens, D. A., Nyblade, A. A., Anandakrishnan, S., Shore, P. J., and Voigt, D. (2006a). Crust and upper mantle structure of the Transantarctic Mountains and surround-

ing regions from receiver functions, surface waves, and gravity: Implications for uplift models. *Geochemistry, Geophysics, Geosystems*, 7(10). doi: 10.1029/2006GC001282.

Lawrence, J. F., Wiens, D. A., Nyblade, A. A., Anandakrishnan, S., Shore, P. J., and Voigt, D. (2006b). Rayleigh wave phase velocity analysis of the Ross Sea, Transantarctic Mountains, and East Antarctica from a temporary seismograph array. *Journal of Geophysical Research: Solid Earth*, 111(B6). doi: 10.1029/2005JB003812.

Leitchenkov, G. L., Antonov, A. V., Luneov, P. I., and Lipenkov, V. Y. (2016). Geology and environments of subglacial Lake Vostok. *Philosophical Transactions of the Royal Society A: Mathematical, Physical and Engineering Sciences*, 374(2059):20140302. doi: 10.1098/rsta.2014.0302.

LeMasurier, W. (1990). Late Cenozoic Volcanism on the Antarctic Plate: An Overview. In *Volcanoes of the Antarctic Plate and Southern Oceans*, pages 1–17. American Geophysical Union (AGU). doi: 10.1029/AR048p0001.

LeMasurier, W. E., Choi, S. H., Hart, S. R., Mukasa, S., and Rogers, N. (2016). Reconciling the shadow of a subduction signature with rift geochemistry and tectonic environment in Eastern Marie Byrd Land, Antarctica. *Lithos*, 260:134–153. doi: 10.1016/j.lithos.2016.05.018.

LeMasurier, W. E. and Rex, D. C. (1989). Evolution of linear volcanic ranges in Marie Byrd Land, West Antarctica. *Journal of Geophysical Research: Solid Earth*, 94(B6):7223–7236. doi: 10.1029/JB094iB06p07223.

Li, X. and Götze, H.-J. (2001). Ellipsoid, geoid, gravity, geodesy, and geophysics. *GEOPHYSICS*, 66(6):1660–1668. doi: 10.1190/1.1487109.

Lisker, F., Prenzel, J., Läufer, A., and Spiegel, C. (2013). The regional thermochronological record as evaluation criterion for uplift models of the Transantarctic Mountains. Presentation at EGU General Assembly 2013, Vienna, Austria.

Lloyd, A. J. (2018). *Seismic Tomography of Antarctica and the Southern Oceans: Regional and Continental Models from the Upper Mantle to the Transition Zone*. PhD thesis, Washington University, St. Louis, Missouri.

Lloyd, A. J., Nyblade, A. A., Wiens, D. A., Hansen, S. E., Kanao, M., Shore, P. J., and Zhao, D. (2013). Upper mantle seismic structure beneath central East Antarctica from body wave tomography: Implications for the origin of the Gamburtsev Subglacial Mountains. *Geochemistry, Geophysics, Geosystems*, 14(4):902–920. doi: 10.1002/ggge.20098.

Lloyd, A. J., Wiens, D. A., Nyblade, A. A., Anandakrishnan, S., Aster, R. C., Huerta, A. D., Wilson, T. J., Dalziel, I. W., Shore, P. J., and Zhao, D. (2015). A seismic transect across West Antarctica: Evidence for mantle thermal anomalies beneath the Bentley Subglacial

Trench and the Marie Byrd Land Dome. *Journal of Geophysical Research: Solid Earth*. doi: 10.1002/2015JB012455.

Lythe, M. B. and Vaughan, D. G. (2001). BEDMAP: A new ice thickness and subglacial topographic model of Antarctica. *Journal of Geophysical Research: Solid Earth*, 106(B6):11335–11351. doi: 10.1029/2000JB900449.

Maaløe, S. and Aoki, K.-i. (1977). The major element composition of the upper mantle estimated from the composition of lherzolites. *Contributions to Mineralogy and Petrology*, 63(2):161–173. doi: 10.1007/BF00398777.

Martin-Español, A., Bamber, J. L., and Zammit-Mangion, A. (2017). Constraining the mass balance of East Antarctica. *Geophysical Research Letters*. doi: 10.1002/2017GL072937.

Martinec, Z. (2014). Mass-density Green's functions for the gravitational gradient tensor at different heights. *Geophysical Journal International*, 196(3):1455–1465. doi: 10.1093/gji/ggt495.

Martos, Y. M., Catalán, M., Jordan, T. A., Golynsky, A., Golynsky, D., Eagles, G., and Vaughan, D. G. (2017). Heat Flux Distribution of Antarctica Unveiled. *Geophysical Research Letters*, 44(22):11,417–11,426. doi: 10.1002/2017GL075609.

Mayer-Gürr, T. (2015). The combined satellite gravity field model GOCO05s. In *EGU General Assembly Conference Abstracts*, volume 17 of *EGU General Assembly Conference Abstracts*, page 12364.

Mayer-Gürr, T., Eicker, A., Kurtenbach, E., and Ilk, K.-H. (2010). ITG-GRACE: Global Static and Temporal Gravity Field Models from GRACE Data. In Flechtner, F. M., Gruber, T., Güntner, A., Mandea, M., Rothacher, M., Schöne, T., and Wickert, J., editors, *System Earth via Geodetic-Geophysical Space Techniques*, pages 159–168. Springer, Berlin, Heidelberg. doi: 10.1007/978-3-642-10228-8_13.

Mayer-Gürr, T., Rieser, D., Höck, E., Brockmann, J., Schuh, W.-D., Krasbutter, I., Kusche, J., Maier, A., Krauss, S., Hausleitner, W., Baur, O., Jäggi, A., Meyer, U., Prange, L., Pail, R., Fecher, T., and Gruber, T. (2012). The new combined satellite only model GOCO03s. In *GGHS2012*, Venice.

McDonough, W. F. and Sun, S.-S. (1995). The composition of the Earth. *Chemical geology*, 120(3):223–253.

McKenzie, D., Jackson, J., and Priestley, K. (2005). Thermal structure of oceanic and continental lithosphere. *Earth and Planetary Science Letters*, 233(3–4):337–349. doi: 10.1016/j.epsl.2005.02.005.

Mishra, D. C., Sekhar, D. V. C., Raju, D. C. V., and Kumar, V. V. (1999). Crustal structure based on gravity–magnetic modelling constrained from seismic studies under Lambert Rift, Antarctica and Godavari and Mahanadi rifts, India and their interrelationship. *Earth and Planetary Science Letters*, 172(3):287–300. doi: 10.1016/S0012-821X(99)00212-5.

Mitrovica, J. X., Gomez, N., Morrow, E., Hay, C., Latychev, K., and Tamisiea, M. E. (2011). On the robustness of predictions of sea level fingerprints. *Geophysical Journal International*, 187(2):729–742. doi: 10.1111/j.1365-246X.2011.05090.x.

Miyamachi, H., Toda, S., Matsushima, T., Takada, M., Watanabe, A., Yamashita, M., and Kanao, M. (2003). Seismic refraction and wide-angle reflection exploration by JARE-43 on Mizuho Plateau, East Antarctica. *Polar geoscience*, 16:1–21.

Ménot, R.-P., Duclaux, G., Peucat, J., Rolland, Y., Guillot, S., Fanning, M., Bascou, J., Gapais, D., and Pecher, A. (2007). Geology of the Terre Adélie Craton (135–146ř E). In Cooper A.K., R. C., editor, *10th International Symposium on Antarctic Earth Sciences*, page 1047, Santa Barbara, United States. doi: 10.3133/of2007-1047.srp048.

Nield, G. A., Barletta, V. R., Bordoni, A., King, M. A., Whitehouse, P. L., Clarke, P. J., Domack, E., Scambos, T. A., and Berthier, E. (2014). Rapid bedrock uplift in the Antarctic Peninsula explained by viscoelastic response to recent ice unloading. *Earth and Planetary Science Letters*, 397:32–41. doi: 10.1016/j.epsl.2014.04.019.

Nield, G. A., Whitehouse, P. L., van der Wal, W., Blank, B., O'Donnell, J. P., and Stuart, G. W. (2018). The impact of lateral variations in lithospheric thickness on glacial isostatic adjustment in West Antarctica. *Geophysical Journal International*, 214(2):811–824. doi: 10.1093/gji/ggy158.

Nowell, D. A. G. (1999). Gravity terrain corrections – an overview. *Journal of Applied Geophysics*, 42(2):117–134. doi: 10.1016/S0926-9851(99)00028-2.

O'Donnell, J. P. and Nyblade, A. A. (2014). Antarcticas hypsometry and crustal thickness: Implications for the origin of anomalous topography in East Antarctica. *Earth and Planetary Science Letters*, 388:143–155. doi: 10.1016/j.epsl.2013.11.051.

O'Donnell, J. P., Selway, K., Nyblade, A. A., Brazier, R. A., Wiens, D. A., Anandakrishnan, S., Aster, R. C., Huerta, A. D., Wilson, T., and Winberry, J. P. (2017). The uppermost mantle seismic velocity and viscosity structure of central West Antarctica. *Earth and Planetary Science Letters*, 472:38–49. doi: 10.1016/j.epsl.2017.05.016.

O'Donnell, J. P., Stuart, G. W., Brisbourne, A. M., Selway, K., Yang, Y., Nield, G. A., Whitehouse, P. L., Nyblade, A. A., Wiens, D. A., Aster, R. C., Anandakrishnan, S., Huerta, A. D., Wilson, T., and Winberry, J. P. (2019). The uppermost mantle seismic velocity

structure of West Antarctica from Rayleigh wave tomography: Insights into tectonic structure and geothermal heat flow. *Earth and Planetary Science Letters*, 522:219–233. doi: 10.1016/j.epsl.2019.06.024.

Oldenburg, D. W. (1974). The Inversion and Interpretation of Gravity Anomalies. *Geophysics*, 39(4):526–536. doi: 10.1190/1.1440444.

Pail, R., Fecher, T., Barnes, D., Factor, J. F., Holmes, S. A., Gruber, T., and Zingerle, P. (2018). Short note: the experimental geopotential model XGM2016. *Journal of Geodesy*, 92(4):443–451. doi: 10.1007/s00190-017-1070-6.

Pappa, F., Ebbing, J., and Ferraccioli, F. (2019a). Moho Depths of Antarctica: Comparison of Seismic, Gravity, and Isostatic Results. *Geochemistry, Geophysics, Geosystems*, 20(3):1629–1645. doi: 10.1029/2018GC008111.

Pappa, F., Ebbing, J., Ferraccioli, F., and van der Wal, W. (2019b). Modeling Satellite Gravity Gradient Data to Derive Density, Temperature, and Viscosity Structure of the Antarctic Lithosphere. *Journal of Geophysical Research: Solid Earth*. doi: 10.1029/2019JB017997.

Parker, R. L. (1973). The Rapid Calculation of Potential Anomalies. *Geophysical Journal International*, 31(4):447–455. doi: 10.1111/j.1365-246X.1973.tb06513.x.

Paulson, A., Zhong, S., and Wahr, J. (2005). Modelling post-glacial rebound with lateral viscosity variations. *Geophysical Journal International*, 163(1):357–371. doi: 10.1111/j.1365-246X.2005.02645.x.

Paxman, G. J. G., Jamieson, S. S. R., Ferraccioli, F., Bentley, M. J., Forsberg, R., Ross, N., Watts, A. B., Corr, H. F. J., and Jordan, T. A. (2017). Uplift and tilting of the Shackleton Range in East Antarctica driven by glacial erosion and normal faulting. *Journal of Geophysical Research: Solid Earth*, 122(3):2390–2408. doi: 10.1002/2016JB013841.

Paxman, G. J. G., Jamieson, S. S. R., Ferraccioli, F., Bentley, M. J., Ross, N., Armadillo, E., Gasson, E. G. W., Leitchenkov, G., and DeConto, R. M. (2018). Bedrock Erosion Surfaces Record Former East Antarctic Ice Sheet Extent. *Geophysical Research Letters*, 45(9):4114–4123. doi: 10.1029/2018GL077268.

Paxman, G. J. G., Jamieson, S. S. R., Ferraccioli, F., Bentley, M. J., Ross, N., Watts, A. B., Leitchenkov, G., Armadillo, E., and Young, D. A. (2019). The Role of Lithospheric Flexure in the Landscape Evolution of the Wilkes Subglacial Basin and Transantarctic Mountains, East Antarctica. *Journal of Geophysical Research: Earth Surface*, 124(3):812–829. doi: 10.1029/2018JF004705.

Paxman, G. J. G., Watts, A. B., Ferraccioli, F., Jordan, T. A., Bell, R. E., Jamieson, S. S. R., and Finn, C. A. (2016). Erosion-driven uplift in the Gamburtsev Subglacial Mountains of East Antarctica. *Earth and Planetary Science Letters*, 452:1–14. doi: 10.1016/j.epsl.2016.07.040.

Peidou, A. and Pagiatakis, S. (2019). Gravity Gradiometry with GRACE Space Missions: New opportunities for the Geosciences. *Journal of Geophysical Research: Solid Earth*. doi: 10.1029/2018JB016382.

Peltier, W. (2004). GLOBAL GLACIAL ISOSTASY AND THE SURFACE OF THE ICE-AGE EARTH: The ICE-5g (VM2) Model and GRACE. *Annual Review of Earth and Planetary Sciences*, 32(1):111–149. doi: 10.1146/annurev.earth.32.082503.144359.

Peslier, A. H., Woodland, A. B., Bell, D. R., and Lazarov, M. (2010). Olivine water contents in the continental lithosphere and the longevity of cratons. *Nature*, 467(7311):78–81. doi: 10.1038/nature09317.

Rabbel, W., Kaban, M., and Tesauro, M. (2013). Contrasts of seismic velocity, density and strength across the Moho. *Tectonophysics*, 609:437–455. doi: 10.1016/j.tecto.2013.06.020.

Ramirez, C., Nyblade, A., Emry, E., Julià, J., Sun, X., Anandakrishnan, S., Wiens, D., Aster, R., Huerta, A., Winberry, P., and Wilson, T. (2017). Crustal structure of the Transantarctic Mountains, Ellsworth Mountains and Marie Byrd Land, Antarctica: constraints on shear wave velocities, Poisson's ratios and Moho depths. *Geophysical Journal International*, 211(3):1328–1340. doi: 10.1093/gji/ggx333.

Ramirez, C., Nyblade, A., Hansen, S., Wiens, D., Anandakrishnan, S., Aster, R., Huerta, A., Shore, P., and Wilson, T. (2016). Crustal and upper-mantle structure beneath ice-covered regions in Antarctica from S-wave receiver functions and implications for heat flow. *Geophysical Journal International*, 204(3):1636–1648. doi: 10.1093/gji/ggv542.

Reading, A. M. (2006). The seismic structure of Precambrian and early Palaeozoic terranes in the Lambert Glacier region, East Antarctica. *Earth and Planetary Science Letters*, 244(1):44–57. doi: 10.1016/j.epsl.2006.01.031.

Reguzzoni, M. and Sampietro, D. (2015). GEMMA: An Earth crustal model based on GOCE satellite data. *International Journal of Applied Earth Observation and Geoinformation*, 35:31–43. doi: 10.1016/j.jag.2014.04.002.

Riedel, S., Jacobs, J., and Jokat, W. (2013). Interpretation of new regional aeromagnetic data over Dronning Maud Land (East Antarctica). *Tectonophysics*, 585:161–171. doi: 10.1016/j.tecto.2012.10.011.

Riedel, S., Jokat, W., and Steinhage, D. (2012). Mapping tectonic provinces with airborne gravity and radar data in Dronning Maud Land, East Antarctica. *Geophysical Journal International*, 189(1):414–427. doi: 10.1111/j.1365-246X.2012.05363.x.

Rignot, E., Bamber, J. L., van den Broeke, M. R., Davis, C., Li, Y., van de Berg, W. J., and van Meijgaard, E. (2008). Recent Antarctic ice mass loss from radarăinterferometry and regional climateămodelling. *Nature Geoscience*, 1:106.

Ritsema, J., Deuss, A., van Heijst, H. J., and Woodhouse, J. H. (2011). S40rts: a degree-40 shear-velocity model for the mantle from new Rayleigh wave dispersion, teleseismic traveltime and normal-mode splitting function measurements. *Geophysical Journal International*, 184(3):1223–1236. doi: 10.1111/j.1365-246X.2010.04884.x.

Ritzwoller, M. H., Shapiro, N. M., Levshin, A. L., and Leahy, G. M. (2001). Crustal and upper mantle structure beneath Antarctica and surrounding oceans. *Journal of Geophysical Research: Solid Earth*, 106(B12):30645–30670. doi: 10.1029/2001JB000179.

Rogozhina, I., Hagedoorn, J. M., Martinec, Z., Fleming, K., Soucek, O., Greve, R., and Thomas, M. (2012). Effects of uncertainties in the geothermal heat flux distribution on the Greenland Ice Sheet: An assessment of existing heat flow models. *Journal of Geophysical Research: Earth Surface*, 117(F2). doi: 10.1029/2011JF002098.

Rose, K. C., Ferraccioli, F., Jamieson, S. S. R., Bell, R. E., Corr, H., Creyts, T. T., Braaten, D., Jordan, T. A., Fretwell, P. T., and Damaske, D. (2013). Early East Antarctic Ice Sheet growth recorded in the landscape of the Gamburtsev Subglacial Mountains. *Earth and Planetary Science Letters*, 375:1–12. doi: 10.1016/j.epsl.2013.03.053.

Rudnick, R. L., McDonough, W. F., and O'Connell, R. J. (1998). Thermal structure, thickness and composition of continental lithosphere. *Chemical Geology*, 145(3–4):395–411. doi: 10.1016/S0009-2541(97)00151-4.

Rummel, R., Yi, W., and Stummer, C. (2011). GOCE gravitational gradiometry. *Journal of Geodesy*, 85(11):777. doi: 10.1007/s00190-011-0500-0.

Salmon, M., Kennett, B. L. N., Stern, T., and Aitken, A. R. A. (2013). The Moho in Australia and New Zealand. *Tectonophysics*, 609:288–298. doi: 10.1016/j.tecto.2012.07.009.

Sato, H. and Sacks, I. S. (1989). Anelasticity and thermal structure of the oceanic upper mantle: Temperature calibration with heat flow data. *Journal of Geophysical Research: Solid Earth*, 94(B5):5705–5715. doi: 10.1029/JB094iB05p05705.

Sato, H., Sacks, I. S., and Murase, T. (1989). The use of laboratory velocity data for estimating temperature and partial melt fraction in the low-velocity zone: Comparison with heat flow

and electrical conductivity studies. *Journal of Geophysical Research: Solid Earth*, 94(B5):5689–5704. doi: 10.1029/JB094iB05p05689.

Schaeffer, A. J. and Lebedev, S. (2013). Global shear speed structure of the upper mantle and transition zone. *Geophysical Journal International*, 194(1):417–449. doi: 10.1093/gji/ggt095.

Scheinert, M., Ferraccioli, F., Schwabe, J., Bell, R., Studinger, M., Damaske, D., Jokat, W., Aleshkova, N., Jordan, T., Leitchenkov, G., Blankenship, D. D., Damiani, T. M., Young, D., Cochran, J. R., and Richter, T. D. (2016). New Antarctic gravity anomaly grid for enhanced geodetic and geophysical studies in Antarctica. *Geophysical Research Letters*, 43(2):600–610. doi: 10.1002/2015GL067439.

Schmidt, S., Plonka, C., Götze, H.-J., and Lahmeyer, B. (2011). Hybrid modelling of gravity, gravity gradients and magnetic fields. *Geophysical Prospecting*, 59(6):1046–1051. doi: 10.1111/j.1365-2478.2011.00999.x.

Sclater, J. G. and Christie, P. A. F. (1980). Continental stretching: An explanation of the Post-Mid-Cretaceous subsidence of the central North Sea Basin. *Journal of Geophysical Research: Solid Earth*, 85(B7):3711–3739. doi: 10.1029/JB085iB07p03711.

Sebera, J., Haagmans, R., Floberghagen, R., and Ebbing, J. (2018). Gravity Spectra from the Density Distribution of Earth's Uppermost 435 km. *Surveys in Geophysics*, 39(2):227–244. doi: 10.1007/s10712-017-9445-z.

Sebera, J., prlák, M., Novák, P., Bezdk, A., and Vako, M. (2014). Iterative Spherical Downward Continuation Applied to Magnetic and Gravitational Data from Satellite. *Surveys in Geophysics*, 35(4):941–958. doi: 10.1007/s10712-014-9285-z.

Seroussi, H., Ivins, E. R., Wiens, D. A., and Bondzio, J. (2017). Influence of a West Antarctic mantle plume on ice sheet basal conditions. *Journal of Geophysical Research: Solid Earth*, 122(9):7127–7155. doi: 10.1002/2017JB014423.

Shapiro, N. M. and Ritzwoller, M. H. (2004). Inferring surface heat flux distributions guided by a global seismic model: particular application to Antarctica. *Earth and Planetary Science Letters*, 223(1–2):213–224. doi: 10.1016/j.epsl.2004.04.011.

Shen, W., Wiens, D. A., Anandakrishnan, S., Aster, R. C., Gerstoft, P., Bromirski, P. D., Hansen, S. E., Dalziel, I. W. D., Heeszel, D. S., Huerta, A. D., Nyblade, A. A., Stephen, R., Wilson, T. J., and Winberry, J. P. (2018). The Crust and Upper Mantle Structure of Central and West Antarctica From Bayesian Inversion of Rayleigh Wave and Receiver Functions. *Journal of Geophysical Research: Solid Earth*, 123(9):7824–7849. doi: 10.1029/2017JB015346.

Shen, W., Wiens, D. A., Stern, T., Anandakrishnan, S., Aster, R. C., Dalziel, I., Hansen, S., Heeszel, D. S., Huerta, A., Nyblade, A., Wilson, T. J., and Winberry, J. P. (2017). Seismic evidence for lithospheric foundering beneath the southern Transantarctic Mountains, Antarctica. *Geology*, 46(1):71. doi: 10.1130/G39555.1.

Shephard, G. E., Matthews, K. J., Hosseini, K., and Domeier, M. (2017). On the consistency of seismically imaged lower mantle slabs. *Scientific Reports*, 7(1):10976. doi: 10.1038/s41598-017-11039-w.

Sigmundsson, F. (1991). Post-glacial rebound and asthenosphere viscosity in Iceland. *Geophysical Research Letters*, 18(6):1131–1134. doi: 10.1029/91GL01342.

Simpson, R. W., Jachens, R. C., Blakely, R. J., and Saltus, R. W. (1986). A new isostatic residual gravity map of the conterminous United States with a discussion on the significance of isostatic residual anomalies. *Journal of Geophysical Research: Solid Earth*, 91(B8):8348–8372. doi: 10.1029/JB091iB08p08348.

Stixrude, L. and Lithgow-Bertelloni, C. (2005). Mineralogy and elasticity of the oceanic upper mantle: Origin of the low-velocity zone. *Journal of Geophysical Research: Solid Earth (1978–2012)*, 110(B3).

Storti, F., Balestrieri, M. L., Balsamo, F., and Rossetti, F. (2008). Structural and thermochronological constraints to the evolution of the West Antarctic Rift System in central Victoria Land. *Tectonics*, 27(4). doi: 10.1029/2006TC002066.

Straume, E. O., Gaina, C., Medvedev, S., Hochmuth, K., Gohl, K., Whittaker, J. M., Abdul Fattah, R., Doornenbal, J. C., and Hopper, J. R. (2019). GlobSed: Updated Total Sediment Thickness in the World's Oceans. *Geochemistry, Geophysics, Geosystems*, 20(4):1756–1772. doi: 10.1029/2018GC008115.

Studinger, M., Bell, R. E., Buck, W. R., Karner, G. D., and Blankenship, D. D. (2004). Sub-ice geology inland of the Transantarctic Mountains in light of new aerogeophysical data. *Earth and Planetary Science Letters*, 220(3–4):391–408. doi: 10.1016/S0012-821X(04)00066-4.

Studinger, M., Karner, G. D., Bell, R. E., Levin, V., Raymond, C. A., and Tikku, A. A. (2003). Geophysical models for the tectonic framework of the Lake Vostok region, East Antarctica. *Earth and Planetary Science Letters*, 216(4):663–677. doi: 10.1016/S0012-821X(03)00548-X.

Stål, T., Reading, A. M., Halpin, J. A., and Whittaker, J. M. (2019). A Multivariate Approach for Mapping Lithospheric Domain Boundaries in East Antarctica. *Geophysical Research Letters*, 46(1718):10404–10416. doi: 10.1029/2019GL083453.

Szwillus, W., Afonso, J. C., Ebbing, J., and Mooney, W. D. (2019). Global Crustal Thickness and Velocity Structure From Geostatistical Analysis of Seismic Data. *Journal of Geophysical Research: Solid Earth*, 124(2):1626–1652. doi: 10.1029/2018JB016593.

Szwillus, W., Ebbing, J., and Holzrichter, N. (2016). Importance of far-field topographic and isostatic corrections for regional density modelling. *Geophysical Journal International*, 207(1):274–287. doi: 10.1093/gji/ggw270.

Tapley, B. D., Bettadpur, S., Ries, J. C., Thompson, P. F., and Watkins, M. M. (2004). GRACE Measurements of Mass Variability in the Earth System. *Science*, 305(5683):503–505. doi: 10.1126/science.1099192.

Thomas, I. D., King, M. A., Bentley, M. J., Whitehouse, P. L., Penna, N. T., Williams, S. D. P., Riva, R. E. M., Lavallee, D. A., Clarke, P. J., King, E. C., Hindmarsh, R. C. A., and Koivula, H. (2011). Widespread low rates of Antarctic glacial isostatic adjustment revealed by GPS observations. *Geophysical Research Letters*, 38(22). doi: 10.1029/2011GL049277.

Torsvik, T., Gaina, C., and Redfield, T. (2007). Antarctica and global paleogeography: from Rodinia, rhrough Gondwanaland and Pangea, to the birth of the Southern Ocean and the opening of gateways. Report 2007-1047-KP-11, U.S. Geological Survey, Washington, DC.

Torsvik, T. H. and Cocks, L. R. M. (2013). Gondwana from top to base in space and time. *Gondwana Research*, 24(3–4):999–1030. doi: 10.1016/j.gr.2013.06.012.

Torsvik, T. H. and Cocks, L. R. M. (2016). *Earth History and Palaeogeography*. Cambridge University Press. doi: 10.1017/9781316225523.

Uieda, L. and Barbosa, V. C. (2017). Fast nonlinear gravity inversion in spherical coordinates with application to the South American Moho. *Geophysical Journal International*, 208(1):162–176. doi: 10.1093/gji/ggw390.

Uieda, L., Bomfom, E. P., Braitenberg, C., and Molina, E. (2011). Optimal Forward Calculation Method of the Marussi Tensor Due to a Geologic Structure at GOCE Height. In *4th International GOCE User Workshop*, volume 696 of *ESA Special Publication*, page 34.

van der Meijde, M., Pail, R., Bingham, R., and Floberghagen, R. (2015). GOCE data, models, and applications: A review. *International Journal of Applied Earth Observation and Geoinformation*, 35:4–15. doi: 10.1016/j.jag.2013.10.001.

van der Wal, W., Barnhoorn, A., Stocchi, P., Gradmann, S., Wu, P., Drury, M., and Vermeersen, B. (2013). Glacial isostatic adjustment model with composite 3-D Earth rheology for Fennoscandia. *Geophysical Journal International*, 194(1):61–77. doi: 10.1093/gji/ggt099.

van der Wal, W., Whitehouse, P. L., and Schrama, E. J. O. (2015). Effect of {GIA} models with 3d composite mantle viscosity on {GRACE} mass balance estimates for Antarctica. *Earth and Planetary Science Letters*, 414:134–143. doi: 10.1016/j.epsl.2015.01.001.

van der Wal, W., Wu, P., Wang, H., and Sideris, M. G. (2010). Sea levels and uplift rate from composite rheology in glacial isostatic adjustment modeling. *Journal of Geodynamics*, 50(1):38–48. doi: 10.1016/j.jog.2010.01.006.

van Wyk de Vries, M., Bingham, R. G., and Hein, A. S. (2017). A new volcanic province: an inventory of subglacial volcanoes in West Antarctica. *Geological Society, London, Special Publications*, 461. doi: 10.1144/SP461.7.

Vermeersen, L. L. A. and Sabadini, R. (1997). A new class of stratified viscoelastic models by analytical techniques. *Geophysical Journal International*, 129(3):531–570. doi: 10.1111/j.1365-246X.1997.tb04492.x.

von Frese, R. R. B., Potts, L. V., Wells, S. B., Leftwich, T. E., Kim, H. R., Kim, J. W., Golynsky, A. V., Hernandez, O., and Gaya-Piqué, L. R. (2009). GRACE gravity evidence for an impact basin in Wilkes Land, Antarctica. *Geochemistry, Geophysics, Geosystems*, 10(2). doi: 10.1029/2008GC002149.

Wannamaker, P., Hill, G., Stodt, J., Maris, V., Ogawa, Y., Selway, K., Boren, G., Bertrand, E., Uhlmann, D., Ayling, B., Green, A. M., and Feucht, D. (2017). Uplift of the central transantarctic mountains. *Nature Communications*, 8(1):1588. doi: 10.1038/s41467-017-01577-2.

Wessel, P., Luis, J., Uieda, L., Scharroo, R., Wobbe, F., Smith, W., and Tian, D. (2019). The Generic Mapping Tools Version 6. *Geochemistry, Geophysics, Geosystems*. doi: 10.1029/2019GC008515.

White-Gaynor, A. L., Nyblade, A. A., Aster, R. C., Wiens, D. A., Bromirski, P. D., Gerstoft, P., Stephen, R. A., Hansen, S. E., Wilson, T., Dalziel, I. W., Huerta, A. D., Winberry, J. P., and Anandakrishnan, S. (2019). Heterogeneous upper mantle structure beneath the Ross Sea Embayment and Marie Byrd Land, West Antarctica, revealed by P-wave tomography. *Earth and Planetary Science Letters*, 513:40–50. doi: 10.1016/j.epsl.2019.02.013.

Whitehouse, P. L., Bentley, M. J., Milne, G. A., King, M. A., and Thomas, I. D. (2012). A new glacial isostatic adjustment model for Antarctica: calibrated and tested using observations of relative sea-level change and present-day uplift rates. *Geophysical Journal International*, 190(3):1464–1482. doi: 10.1111/j.1365-246X.2012.05557.x.

Whittaker, J. M., Goncharov, A., Williams, S. E., Müller, R. D., and Leitchenkov, G. (2013). Global sediment thickness data set updated for the Australian-Antarctic Southern Ocean. *Geochemistry, Geophysics, Geosystems*, 14(8):3297–3305. doi: 10.1002/ggge.20181.

Wobbe, F., Lindeque, A., and Gohl, K. (2014). *Total sediment thickness grid of the Southern Pacific Ocean off West Antarctica, links to NetCDF files*. PANGAEA.

Wu, P. (2004). Using commercial finite element packages for the study of earth deformations, sea levels and the state of stress. *Geophysical Journal International*, 158(2):401–408. doi: 10.1111/j.1365-246X.2004.02338.x.

Wu, P. (2005). Effects of lateral variations in lithospheric thickness and mantle viscosity on glacially induced surface motion in Laurentia. *Earth and Planetary Science Letters*, 235(3):549–563. doi: 10.1016/j.epsl.2005.04.038.

Wörner, G. (1999). Lithospheric dynamics and mantle sources of alkaline magmatism of the Cenozoic West Antarctic Rift System. *Global and Planetary Change*, 23(1):61–77. doi: 10.1016/S0921-8181(99)00051-X.

Yildiz, H., Forsberg, R., Tscherning, C. C., Steinhage, D., Eagles, G., and Bouman, J. (2017). Upward continuation of Dome-C airborne gravity and comparison with GOCE gradients at orbit altitude in east Antarctica. *Studia Geophysica et Geodaetica*, 61(1):53–68. doi: 10.1007/s11200-015-0634-2.

Yoshii, K., Ito, K., Miyamachi, H., and Kanao, M. (2004). Crustal structure derived from seismic refractions and wide-angle reflections in the Mizuho Plateau, East Antarctica. *Polar geoscience*, 17:112–138.

Zingerle, P., Pail, R., Scheinert, M., and Schaller, T. (2019). Evaluation of terrestrial and airborne gravity data over Antarctica – a generic approach. *Journal of Geodetic Science*, 9(1):29. doi: 10.1515/jogs-2019-0004.

Appendix A

Supplementary Material

Supporting Information for Paper II:
Modeling Satellite Gravity Gradient Data to Derive Density, Temperature, and Viscosity Structure of the Antarctic Lithosphere

Original file: jgrb53830-sup-0002-2019JB017997-S02.pdf , see https://doi.org/10.1029/2019JB017997

A.1. Introduction

The detailed formulas for the tensor basis change of the gravity gradient components and an according script function for MATLAB / GNU Octave can be found in A.4. A detailed description of the fitting process is given in section A.2. Figure A.1 shows the gravity gradients in the common North-West-Up frame and demonstrates the issue of that representation in polar regions. The effect of the complete reduction model (water, ice, topography, sediments) is shown in Figure A.2. This document further includes figures that illustrate the uncertainty in the input data of our models, which concerns the estimate of bedrock elevation (Figures A.3 and A.4) and the GIA-related vertical displacement of the crust (Figures A.5 and A.6). In addition, results of Model 1 are shown (Figures A.7 and A.8), as well as supplementary information on the parameterization of Model 2 and Model 3 (Figure A.9). Their misfit with respect to seismic Moho depth estimates is visualized in histogram plots (Figure A.10). Finally, the

cumulative RMS signal of the vertical gravity and the gravity gradients is presented in Figure A.11.

A.2. Description of the Fitting Process

In the following we describe the procedure of fitting the Moho and LAB interfaces in the model to observational data (compare Results and Discussion). Starting from an initial model geometry of Moho and LAB boundaries based on seismic studies, both interfaces are iteratively changed in Model 1 (and subsequently Model 2) in order to achieve isostatic equilibrium, i.e. the modeled topography matches the observed rock-equivalent topography. LitMod3D uses the principle of Airy-type isostasy to model the topography (see Modeling Methods). Given that the initial model shows a large topographic residual, we can use Airy's principle to compute a shift for the Moho and/or the LAB at every location of our model necessary to compensate the residual. As additional parameters, values for topographic rock density ρ_{topo} and the density contrast at the respective interface $\Delta\rho_{\text{interface}}$ are required. The topographic rock density is set to 2670 kg/m^3 in the model, whereas the density contrast at the interface is a function of pressure, temperature, and rock properties such as composition (for mantle material) or thermal expansion and compressibility (for crustal rocks) and thus non-linear in our modeling. The shift required at the interface (Moho or the LAB) $\Delta h_{\text{interface}}$ in order to compensate the topographic residual Δh_{topo} in each iteration step can be calculated according to Airy-isostasy via:

$$\Delta h_{\text{interface}} = -\Delta h_{\text{topo}} \frac{\rho_{\text{topo}}}{\Delta\rho_{\text{interface}}}$$

For instance, a density contrast of $\Delta\rho_{\text{Moho}} = 300$ kg/m^3 would lead to a factor of 8.9 to be multiplied with the residual topography (given in km) in order to obtain the vertical shift at the Moho required to match the observed topography in terms of pure Airy-isostasy. The same can be estimated for the LAB, e.g. with a density contrast of $\Delta\rho_{\text{LAB}} = 30$ kg/m^3. In our fitting procedure, we vary Moho and LAB depth simultaneously with factors obtained as described above. In addition these factors must be weighted (weighting factors must add up to 1), depending on which interface should be changed more. However, by varying the interfaces in the model, the temperature and pressure field change as well, leading to non-linear changes in the density column. Thus, the procedure must be repeated until the mismatch is

satisfyingly small, e.g. with an RMS error of less than 50 m as shown in Figure A.7. In our modeling, factors of 3 for the continental Moho and 12 for the LAB have proven feasible, but needed to be varied during the fitting process with respect to the non-monotonic behavior at the LAB.

In Model 3 the assumption of isostatic equilibrium is discarded, and the model is instead fitted to the gravity gradient data. In consequence, the above formula for Airy-isostasy cannot be used for this purpose. Fitting factors need to be found in other ways, e.g. through analysis of the relationship between Moho and LAB depth and the gravity gradients. We pursued a probabilistic approach and tested a wide range of factors that could be suitable for multiplication with the residual vertical gravity gradient T_{UU} in order to obtain the shift required at the respective interface to compensate the residual. As a result, factors of 2 for the continental Moho and –6 for the continental LAB turned out to be appropriate (gradient residuals given in E), but again needed to be varied to account for the non-linear relationship between interface geometries and densities in the model. The final residual in Model 3 accounts for a RMS misfit of 0.045 E in the vertical gradient T_{UU}.

A.3. Supplementary Figures

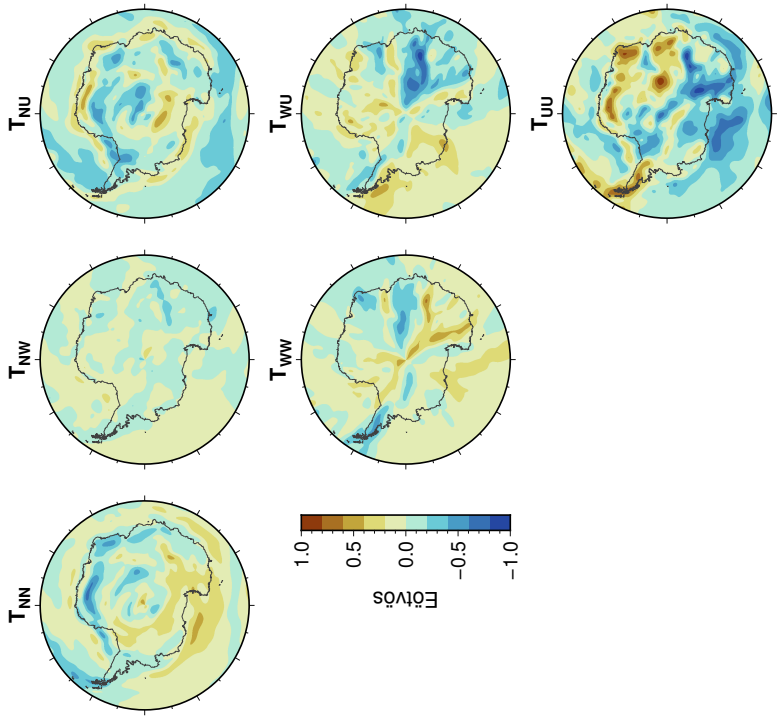

Figure A.1.: GOCE derived gravity gradients in North-West-Up frame at 225 km altitude (Bouman et al., 2016). The transformed tensor components in the IAU frame are shown in Figure 3.2.

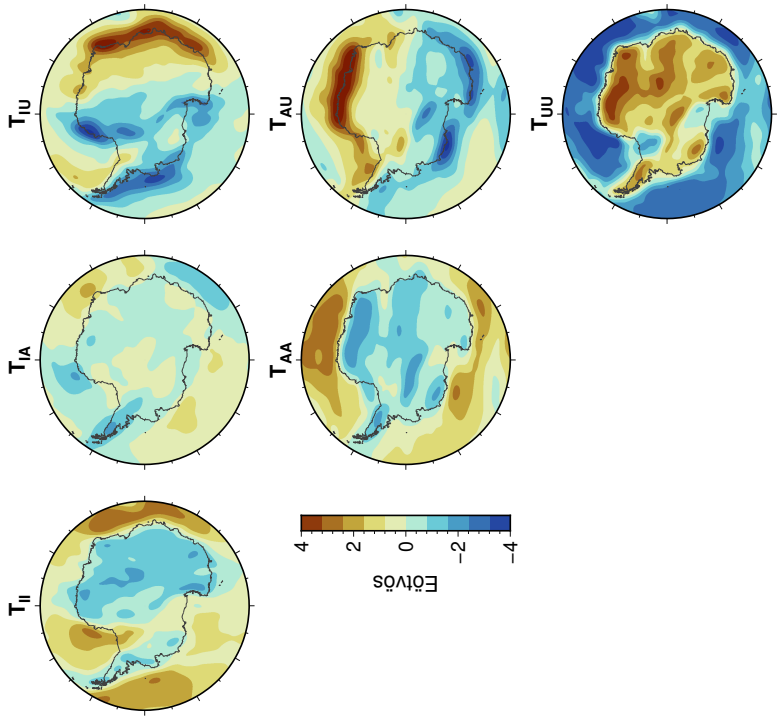

Figure A.2.: Gravity gradient effect of the complete reduction model, based on topography data from the Bedmap2 model (Fretwell et al., 2013), at 225 km altitude. The used densities are described in section 3.2.

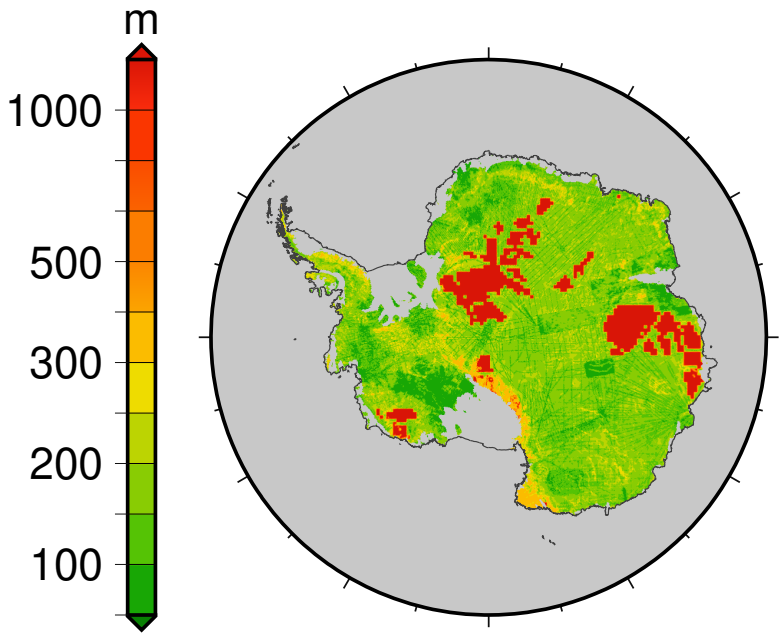

Figure A.3.: Estimated bedrock elevation uncertainty of the Bedmap2 model (Fretwell et al., 2013).

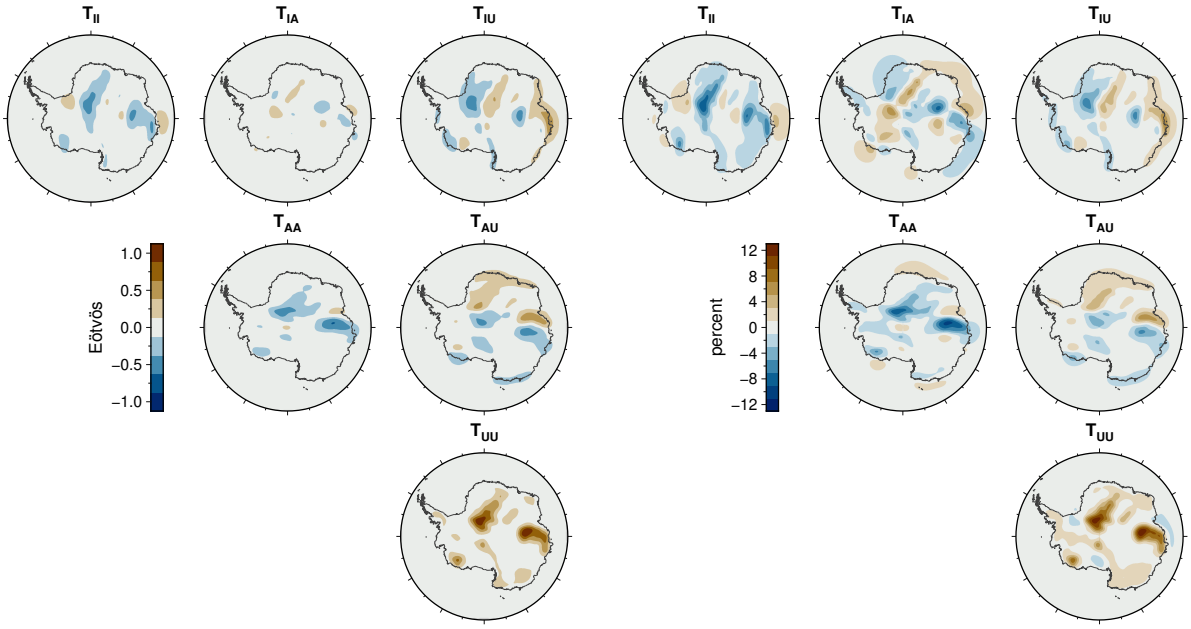

Figure A.4.: Gravity gradient effect of Bedmap2 uncertainty (Figure A.3). Left: absolute values, right: relative to complete topographic reduction model (Figure A.2). A density contrast of 1740 kg/m^3 between ice and rock is used for the computation.

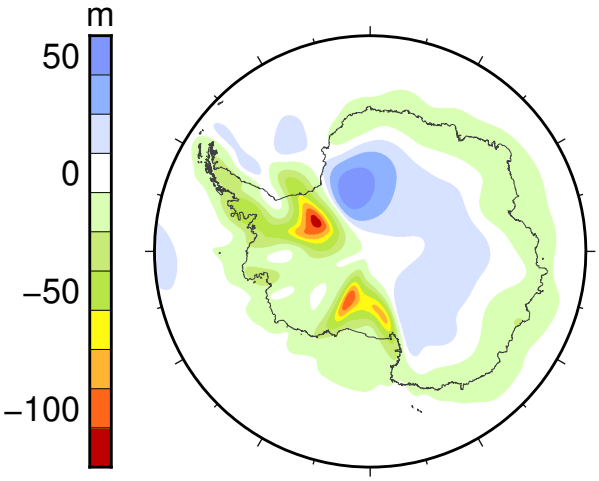

Figure A.5.: GIA-induced vertical displacement of the crust, based on W12 ice history model (Whitehouse et al., 2012) and viscosity inferred from seismological S-wave velocity model S40RTS (Ritsema et al., 2011) with 4 mm grain size and wet rheology.

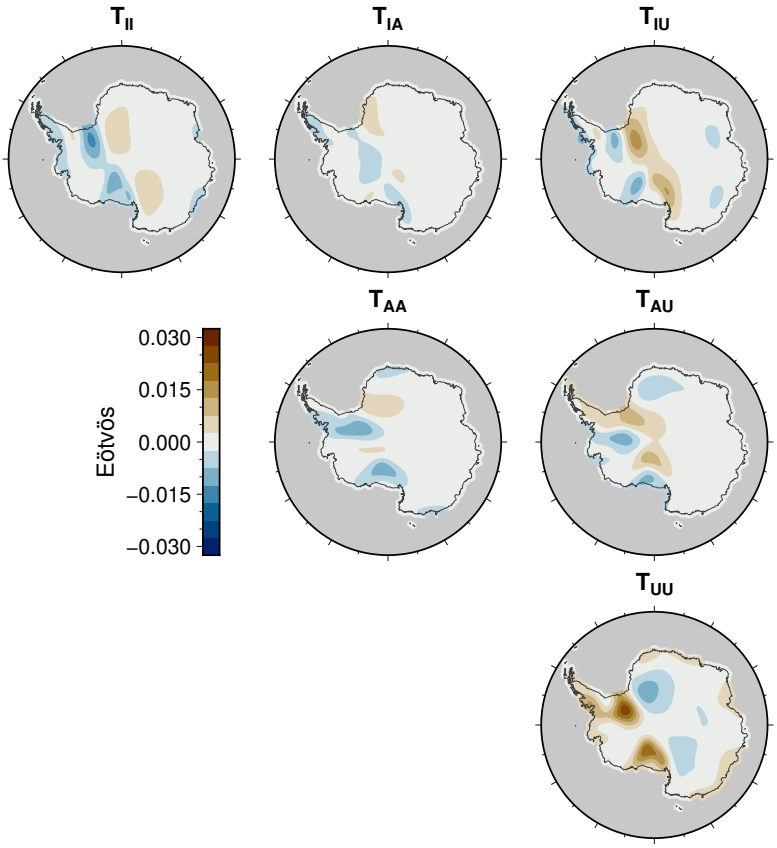

Figure A.6.: Gravity gradient effect of crustal vertical displacement shown in Figure A.5 at 225 km altitude. The mass changes are applied at Moho depth, using AN1-Moho depth model (An et al., 2015b), with a density difference of 400 kg/m^3 between crust and mantle.

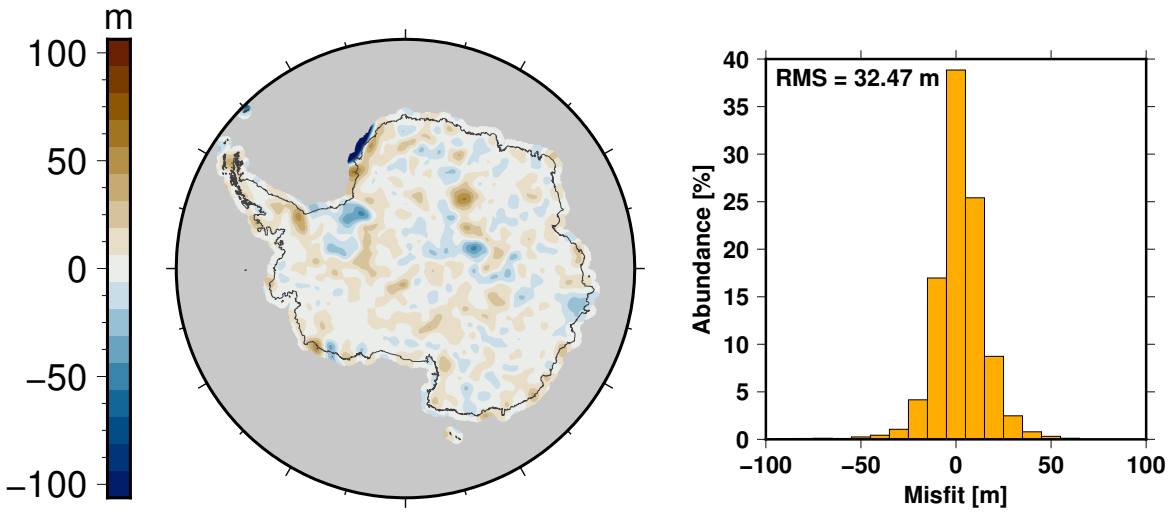

Figure A.7.: Topography misfit map and histogram of Model 1.

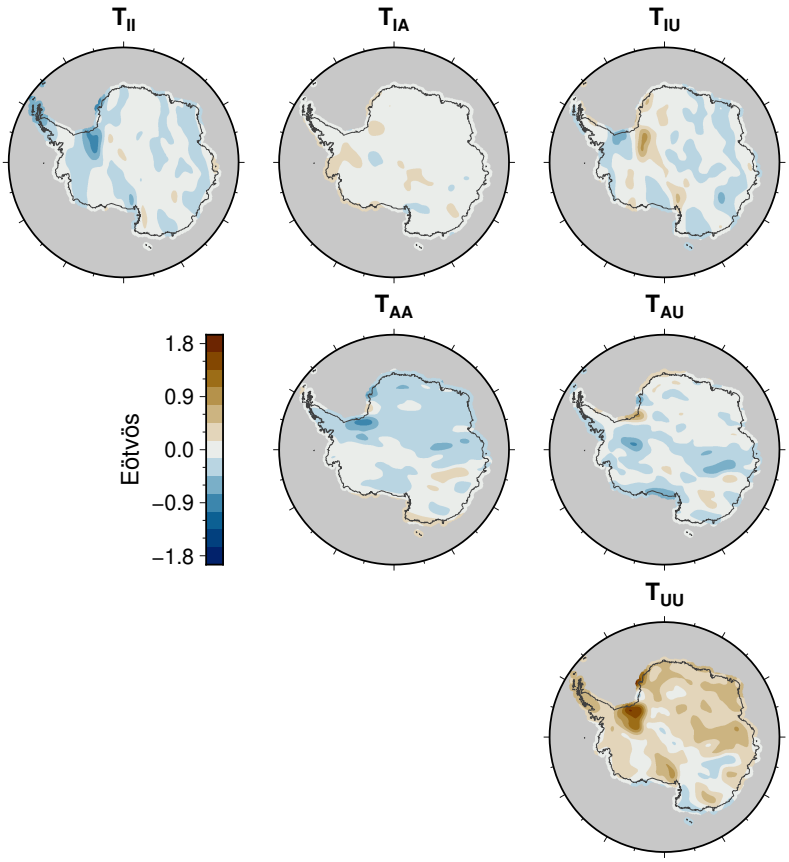

Figure A.8.: Misfit of gravity gradient signal of Model 1.

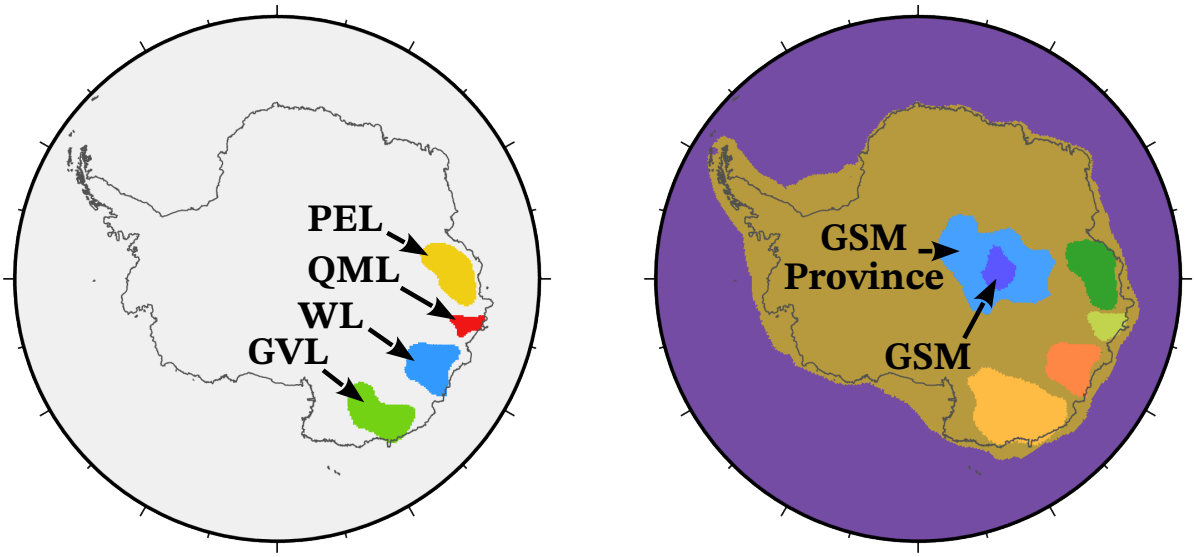

Figure A.9.: Left: areas with Archaean lithospheric mantle bodies in Model 2 and Model 3. They are deduced from the locations of high gravity gradient residuals in Model 1. Right: areas of modified crustal parameters in Model 2 and Model 3. GSM=Gamburtsev Subglacial Mountains, GVL=George V Land, PEL=Princess Elizabeth Land, QML=Queen Mary Land, WL=Wilkes Land.

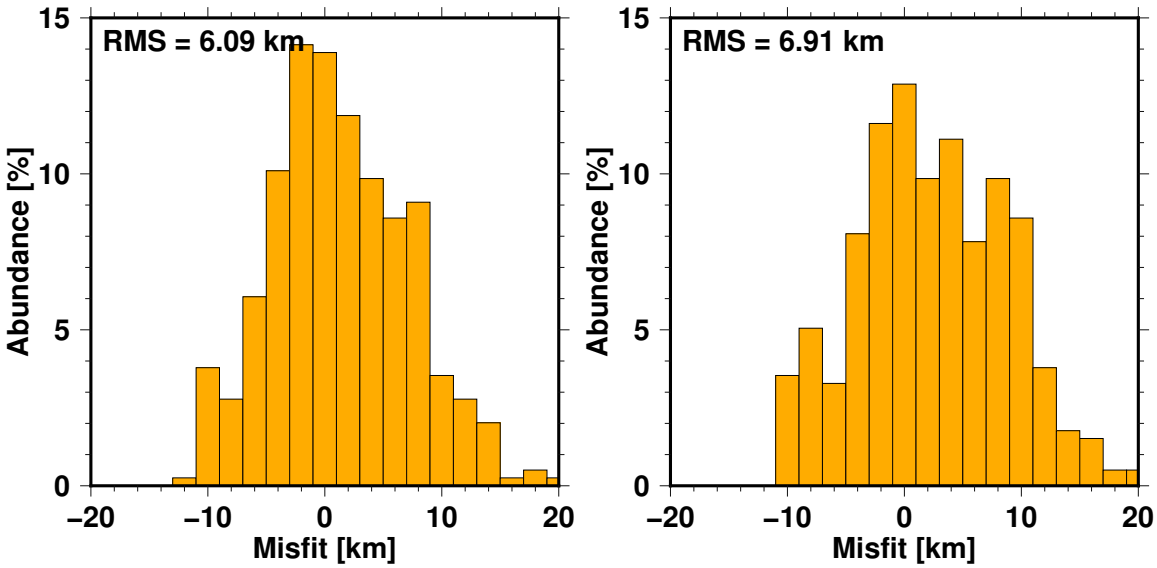

Figure A.10.: Misfit histograms of Moho depth with respect to seismic estimates. Left: Model 2; right: Model 3.

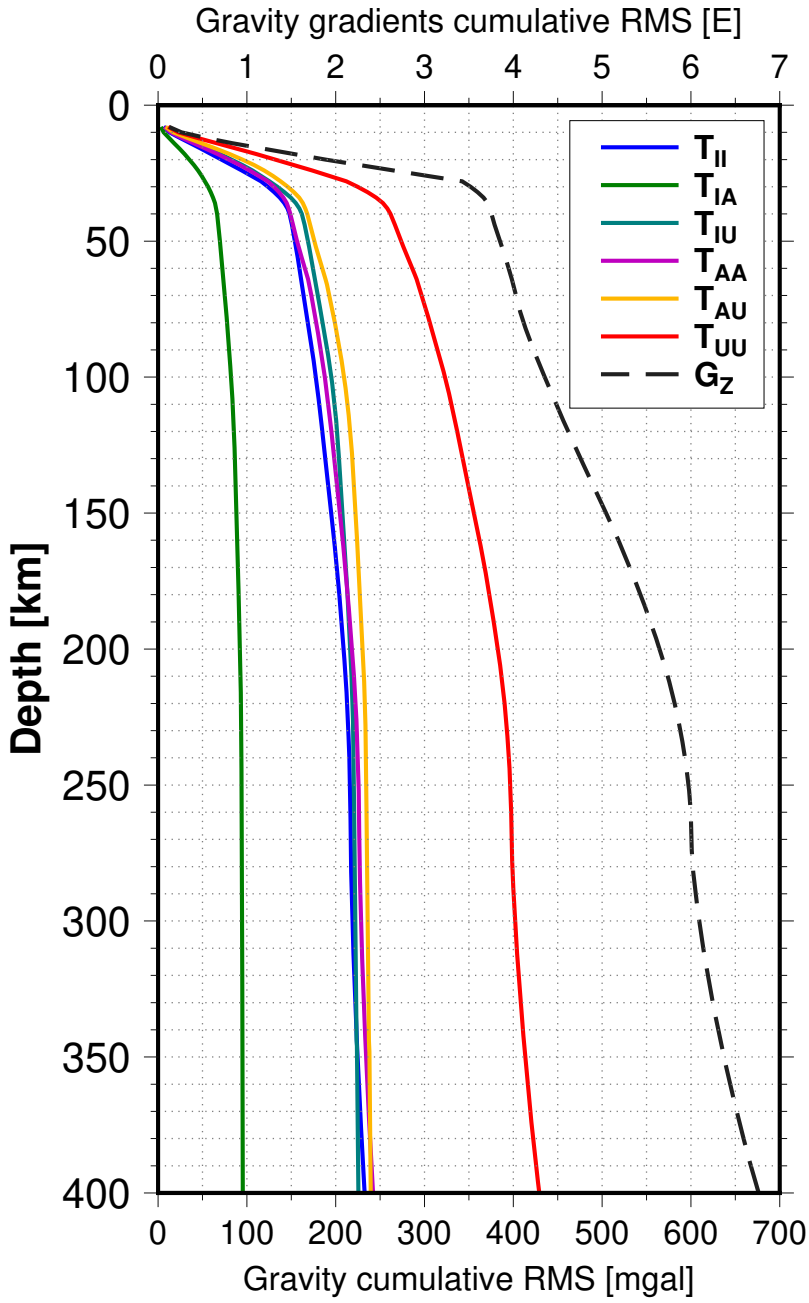

Figure A.11.: Depth-cumulative root mean square (RMS) signal of vertical gravity G_Z and gravity gradients of Model 3. Compare Figure 3.3 (right) in section 3.3. The highest increase is present in the crustal depth range (30 km). Below ~240 km the cumulative gravity gradient RMS signals stagnate, whereas the vertical gravity is still sensitive to density variations. The total RMS sums at 400 km are T_{II}: 2.33 E; T_{IA}: 0.95 E; T_{IU}: 2.26 E; T_{AA}: 2.42 E; T_{AU}: 2.39 E; T_{UU}: 4.29 E; G_Z: 676 mgal.

A.4. Transformation equations for gravity gradients

Since the derivative $D\overrightarrow{T}$ of the gravity $\overrightarrow{T}$ is a tensor (of first degree), one has:

$$\begin{aligned} D\overrightarrow{T} &= T_n\overrightarrow{e_n} + T_w\overrightarrow{e_w} + T_u\overrightarrow{e_u} \\ &= T_n\overrightarrow{e_n} + T_e\overrightarrow{e_e} + T_u\overrightarrow{e_u} \\ &= T_i\overrightarrow{e_i} + T_a\overrightarrow{e_a} + T_u\overrightarrow{e_u} \end{aligned}$$

with: $\overrightarrow{e_x}$ is the corresponding unit vector, and

$$\begin{pmatrix} T_i \\ T_a \\ T_u \end{pmatrix} = \begin{pmatrix} \sin\lambda & -\cos\lambda & 0 \\ \cos\lambda & \sin\lambda & 0 \\ 0 & 0 & 1 \end{pmatrix} \begin{pmatrix} T_n \\ T_w \\ T_u \end{pmatrix}$$

$$\begin{pmatrix} T_i \\ T_a \\ T_u \end{pmatrix} = \begin{pmatrix} \sin\lambda & \cos\lambda & 0 \\ \cos\lambda & -\sin\lambda & 0 \\ 0 & 0 & 1 \end{pmatrix} \begin{pmatrix} T_n \\ T_e \\ T_u \end{pmatrix}$$

The invariants are given by:

$$\begin{aligned} I_1 &= T_{xx}T_{yy} + T_{yy}T_{zz} + T_{xx}T_{zz} - \left(T_{xy}^2 + T_{xz}^2 + T_{yz}^2\right) \\ I_2 &= det\,(T) \end{aligned}$$

Derivation of the gravity $\overrightarrow{T}$ according to local north-oriented frame (*North-West-Up*, GOCE) to get the gravity gradients in the *India-Atlantic-Up* frame:

$$\text{By } \begin{pmatrix} \frac{\partial n}{\partial i} & \frac{\partial w}{\partial i} \\ \frac{\partial n}{\partial a} & \frac{\partial w}{\partial a} \end{pmatrix} = \begin{pmatrix} \sin\lambda & -\cos\lambda \\ \cos\lambda & \sin\lambda \end{pmatrix} \text{ one has:}$$

$$\begin{aligned} T_{ii} &= \frac{\partial T_i}{\partial i} = \frac{\partial T_i}{\partial n}\frac{\partial n}{\partial i} + \frac{\partial T_i}{\partial w}\frac{\partial w}{\partial i} \\ &= \frac{\partial}{\partial n}\big(T_n \sin\lambda - T_w \cos\lambda\big)\sin\lambda - \frac{\partial}{\partial w}\big(T_n \sin\lambda - T_w \cos\lambda\big)\cos\lambda \\ &= T_{nn}\sin^2\lambda - 2T_{nw}\sin\lambda\cos\lambda + T_{ww}\cos^2\lambda \end{aligned}$$

$$\begin{aligned} T_{ia} &= \frac{\partial T_i}{\partial a} = \frac{\partial T_i}{\partial n}\frac{\partial n}{\partial a} + \frac{\partial T_i}{\partial w}\frac{\partial w}{\partial a} \\ &= \frac{\partial}{\partial n}\big(T_n \sin\lambda - T_w \cos\lambda\big)\cos\lambda + \frac{\partial}{\partial w}\big(T_n \sin\lambda - T_w \cos\lambda\big)\sin\lambda \\ &= T_{nn}\sin\lambda\cos\lambda - T_{wn}\cos^2\lambda + T_{nw}\sin^2\lambda - T_{ww}\sin\lambda\cos\lambda \\ &= T_{nn}\sin\lambda\cos\lambda + T_{nw}(\sin^2\lambda - \cos^2\lambda) - T_{ww}\sin\lambda\cos\lambda \end{aligned}$$

$$\begin{aligned} T_{iu} &= \frac{\partial T_i}{\partial u} = \frac{\partial}{\partial u}\big(T_n \sin\lambda - T_w \cos\lambda\big) \\ &= T_{nu}\sin\lambda - T_{wu}\cos\lambda \end{aligned}$$

$$\begin{aligned} T_{aa} &= \frac{\partial T_a}{\partial a} = \frac{\partial T_a}{\partial n}\frac{\partial n}{\partial a} + \frac{\partial T_a}{\partial w}\frac{\partial w}{\partial a} \\ &= \frac{\partial}{\partial n}\big(T_n \cos\lambda + T_w \sin\lambda\big)\cos\lambda + \frac{\partial}{\partial w}\big(T_n \cos\lambda + T_w \sin\lambda\big)\sin\lambda \\ &= T_{nn}\cos^2\lambda + 2T_{nw}\sin\lambda\cos\lambda + T_{ww}\sin^2\lambda \end{aligned}$$

$$\begin{aligned} T_{au} &= \frac{\partial T_a}{\partial u} = \frac{\partial}{\partial u}\big(T_n \cos\lambda + T_w \sin\lambda\big) \\ &= T_{nu}\cos\lambda + T_{wu}\sin\lambda \end{aligned}$$

$$T_{uu} = \frac{\partial T_u}{\partial u}$$

MATLAB / GNU Octave code

```
%nwu2iau Transform GOCE gravity gradient tensor (GGT) from LNOF (North-West-Up) into IAU
(India-Atlantic-Up) frame according to polar stereographic projection.
% Author: F. Pappa, 2015-11-11
% Input:
% 1: GGTnwu contains the columns: Gnn,Gnw,Gnu,Gww,Gwu,Guu
% 2: Longitude of measurement position
% Output: GGTiau: GGT in IAU directions
function GGTiau = nwu2iau(GGTnwu,lon)

      l = lon.*(pi/180);
      Gii = GGTnwu(:,1).*sin(l).^2 - 2*GGTnwu(:,2).*sin(l).*cos(l)
      + GGTnwu(:,4).*cos(l).^2;
      Gia = GGTnwu(:,1).*sin(l).*cos(l) + GGTnwu(:,2).*(sin(l).^2-cos(l).^2)
      - GGTnwu(:,4).*sin(l).*cos(l);
      Giu = GGTnwu(:,3).*sin(l) - GGTnwu(:,5).*cos(l);
      Gaa = GGTnwu(:,1).*cos(l).^2 + 2*GGTnwu(:,2).*sin(l).*cos(l)
      + GGTnwu(:,4).*sin(l).^2;
      Gau = GGTnwu(:,3).*cos(l) + GGTnwu(:,5).*sin(l);
      Guu = GGTnwu(:,6);
      GGTiau = [Gii Gia Giu Gaa Gau Guu];

endfunction
```

```
%neu2iau Transform gravity gradient tensor (GGT) from Tesseroids software (Uieda et al., 2011) from
North-East-Up into IAU (India-Atlantic-Up) frame according to polar stereographic projection.
% Author: F. Pappa, 2015-12-02
% Input:
% 1: GGTneu contains the columns: Gnn,Gne,Gnu,Gee,Geu,Guu
% 2: Longitude of measurement position
% Output: GGTiau: GGT in IAU directions
% References:
% Uieda, L., E. P. Bomfim, C. Braitenberg, and E. Molina (2011), Optimal forward calculation method
of the Marussi tensor due to a geologic structure at GOCE height, Proceedings of the 4th International
GOCE User Workshop
function GGTiau = neu2iau(GGTneu,lon)

      l = lon.*(pi/180);
      Gii = GGTneu(:,1).*sin(l).^2 + 2*GGTneu(:,2).*sin(l).*cos(l)
      + GGTneu(:,4).*cos(l).^2;
      Gia = GGTneu(:,1).*sin(l).*cos(l) + GGTneu(:,2).*(cos(l).^2-sin(l).^2)
      - GGTneu(:,4).*sin(l).*cos(l);
      Giu = GGTneu(:,3).*sin(l) + GGTneu(:,5).*cos(l);
      Gaa = GGTneu(:,1).*cos(l).^2 - 2*GGTneu(:,2).*sin(l).*cos(l)
      + GGTneu(:,4).*sin(l).^2;
      Gau = GGTneu(:,3).*cos(l) - GGTneu(:,5).*sin(l);
      Guu = GGTneu(:,6);
      GGTiau = [Gii Gia Giu Gaa Gau Guu];

endfunction
```

Danksagung

Viele Menschen haben auf unterschiedliche Weise dazu beigetragen, dass es mir möglich war, die vorliegende Arbeit anzufertigen. Mein besonderer Dank gilt meinem Betreuer Prof. Dr. Jörg Ebbing für seine Hinweise, Ratschläge und Unterstützung, insbesondere aber für die Möglichkeit, an zahlreichen Tagungen, Konferenzen und Meetings teilzunehmen und Erfahrungen zu sammeln. Ich danke Wouter van der Wal und Fausto Ferraccioli, den Koautoren der hier einbezogenen Publikationen, für ihre hochwertigen Beiträge. Auch der Austausch und die Diskussionen mit gegenwärtigen und ehemaligen Kollegen haben oft zum Fortschritt meiner Arbeit beigetragen.

Darüber hinaus kann nicht ausreichend betont werden, dass Forschungsarbeiten wie die hier vorliegende nicht möglich wären, wenn nicht die finanziellen Mittel bereitgestellt würden. Deswegen sei an dieser Stelle allen Steuerzahlern der Mitgliedstaaten der Europäischen Weltraumorganisation ESA gedankt. Durch sie konnten die Forschungsprojekte *GOCE+Antarctica* und *3D Earth* finanziert werden, in deren Rahmen auch diese Arbeit entstand. Ebenso möchte ich meine große Wertschätzung für diejenigen Menschen ausdrücken, die sich im politischen Raum für eine gute finanzielle Ausstattung von Hochschulen und Forschungseinrichtungen einsetzen.

Abschließend sei den Entwicklern frei verfügbarer Software gedankt, insbesondere der zahlreichen nützlichen Linux-Shell-Anwendungen und der *Generic Mapping Tools* (GMT, Wessel et al., 2019), mit denen sämtliche Karten in dieser Arbeit erstellt wurden.